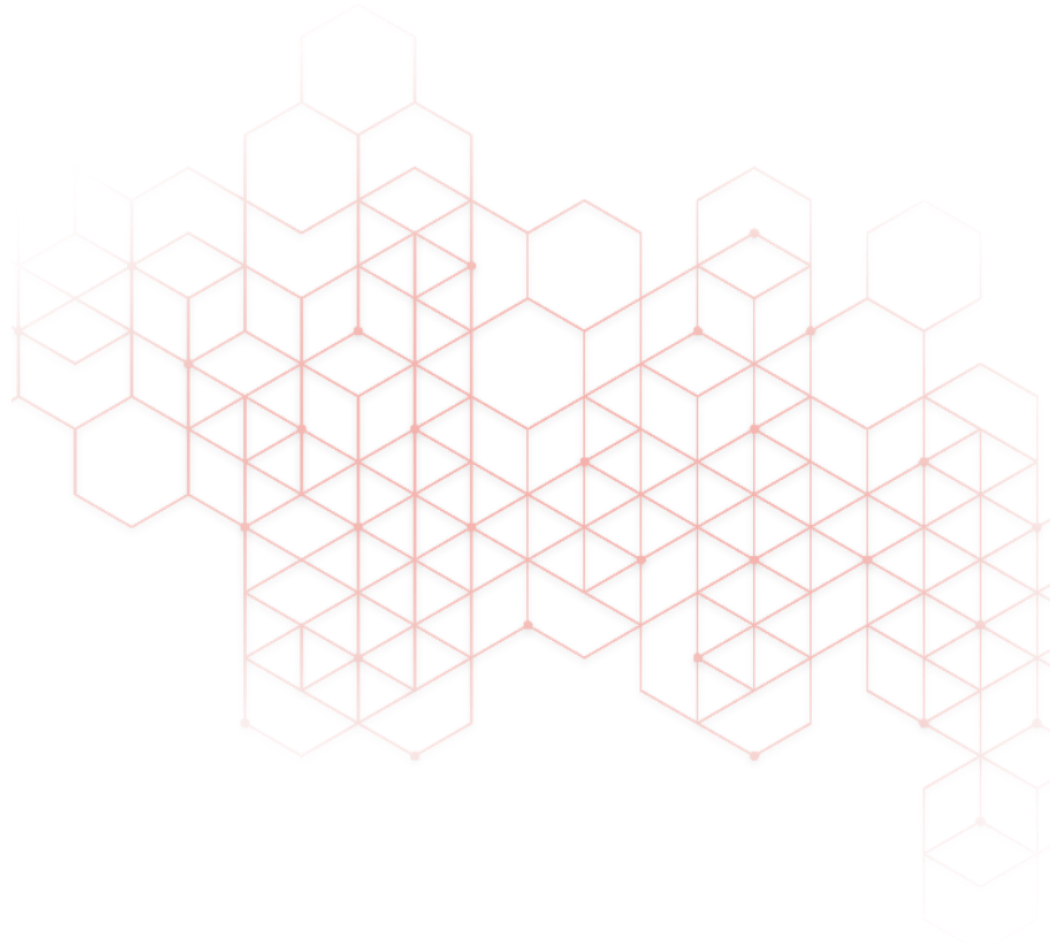# D2.1 – Impact of H₂ heating on product quality, yield, and refractory

Henri Pauna, Juho Haapakangas, Xabier Zapirain Sesma, Yáiza Montaña González, Amaia Iza-Mendia, Olaya Laviana Quintas, Beatriz Pérez Polo, Jon Etxeberria Uranga, Andreas Buchholz, Daniel Krings, Detlef Mackenstedt, Thorsten Tonnesen, Tobias Tillmann, Giovanni Curedda, Robin Mottram

HYINHEAT

Credits

Copyright © 2024 HyInHeat project

Disclaimer

The sole responsibility of this publication lies with the author. The European Union is not responsible for any use that may be made of the information contained therein.

HYINHEAT

Technical references

Grant Agreement N°	101091456	Acronym	HyInHeat
Full Title	Hydrogen technologies for decarbonization of industrial heating processes		
Work Package (WP)	Work Package 2		
Authors	Henri Pauna (OULU), Juho Haapakangas (OULU), Xabier Zapirain Sesma (CEIT), Yáiza Montaña González (CEIT), Amaia Iza-Mendia (CEIT), Olaya Laviana Quintas (CEIT), Beatriz Pérez Polo (CEIT), Jon Etxeberria Uranga (CEIT), Andreas Buchholz (SPE), Daniel Krings (SPE), Detlef Mackenstedt (SPE), Thorsten Tonnesen (RWTH-GHI), Tobias Tillmann (RWTH-GHI), Curedda Giovanni (DAN), Robin Mottram (TCUK)		
Leading organisation	University of Oulu (OULU)		
Date of publication	30/06/2024		
Contributors	CEIT, SPE, RWTH-GHI, OULU, SSAB, AMOB, AMS, TCUK		
Document Type	R – Report		
Document Title	Impact of H$_2$ heating on product quality, yield, and refractory		
Dissemination Level	Public		

Document history

Version	Date	Partner	Author
0.1 (template)	2023/11/20	OULU	Henri Pauna
0.2 (1st draft)	2024/05/29	OULU	Henri Pauna
0.3 (2nd draft)	2024/06/07	OULU	Henri Pauna
1.0	2024/06/17	OULU	Henri Pauna
1.1	2024/06/27	OULU	Henri Pauna

HYINHEAT

Contents

HYINHEAT

Impact of H₂ heating on product quality, yield, and refractory

HYINHEAT

Tables & Figures

HYINHEAT

Figures

HYINHEAT

HYINHEAT

HYINHEAT

HYINHEAT

List of abbreviations

Abbreviations	Explanation
AISCAN	Trademark of ABB for measurement device of hydrogen concentration in molten aluminium
CBS	Can Body Stock
EDS	Energy Dispersive Spectroscopy
FESEM	Field Emission Scanning Electron Microscopy
HPLC (pump)	Solvent delivery system
LTOF	Low Temperature OxyFuel
TGA	Thermogravimetric analysis
MMVF	Man Made Vitious Fibres
RCF	Refractory Ceramic Fibres
AES	Alkaline Earth Silicate

HYINHEAT

A. Investigation of promising refractory material through lab trials and thermodynamic calculations

A.1 Material identification and test setup

Prior to conducting laboratory tests, it is essential to identify an appropriate refractory material that is suitable for the intended tests. To this end, the company Speira was consulted. Based on the technical drawing of the furnace and a subsequent inspection of the test furnace at the furnace location, it was determined that two distinct refractory materials, in direct contact with the furnace atmosphere, are suitable for laboratory tests in different atmospheres. The first material is used to line the bottom and side walls of the furnace. This material is therefore in direct contact with the furnace atmosphere. It is therefore necessary to investigate how the new furnace atmosphere affects the material and whether it is possible to switch to hydrogen firing. This material is a dense medium cement castable based on Al$_2$O$_3$. The maximum application temperature is 1500 °C and the main raw material component is tabular alumina. As it is a medium cement castable, the refractory is hydraulically bound. The second material is used to line the ceiling of the furnace and it is therefore also important to investigate the influence of the new atmosphere on this material. This is also a dense medium cement castable. However, this refractory consists of Al$_2$O$_3$ and SiO$_2$. These two materials were selected for the tests for the reasons mentioned above. The next step is to determine a suitable atmosphere in which the tests can be carried out. When the furnace was converted to hydrogen firing for a short time, it was found that the length of the burner flame increases due to the larger gas volume and that it therefore comes into direct contact with the refractory material. It was also found that the combustion of hydrogen is a sub-stoichiometric combustion. This means that a small amount of hydrogen remains in the atmosphere. This hydrogen could lead to a reduction of components of the refractory material and thus damage the material and make it impossible to convert the firing. For this reason, it was decided to store the various materials in a hydrogen-containing atmosphere in order to investigate the effects of a hydrogen-containing atmosphere on these materials. An atmosphere with a low hydrogen content was selected. During the before mentioned short-term conversion of the furnace, it was determined that the maximum operating temperature is 950 °C. For this reason, the first temperature for the ageing tests was set at 950 °C. However, it was decided to carry out a further series of tests at a higher temperature of 1300 °C in order to deliberately exceed this temperature and provoke signs of corrosion. This temperature is intended to simulate the worst case. The dwell times chosen were 24 hours on the one hand and 96 hours on the other. The tests carried out for the different materials can therefore be summarized in the following test matrix.

HYINHEAT
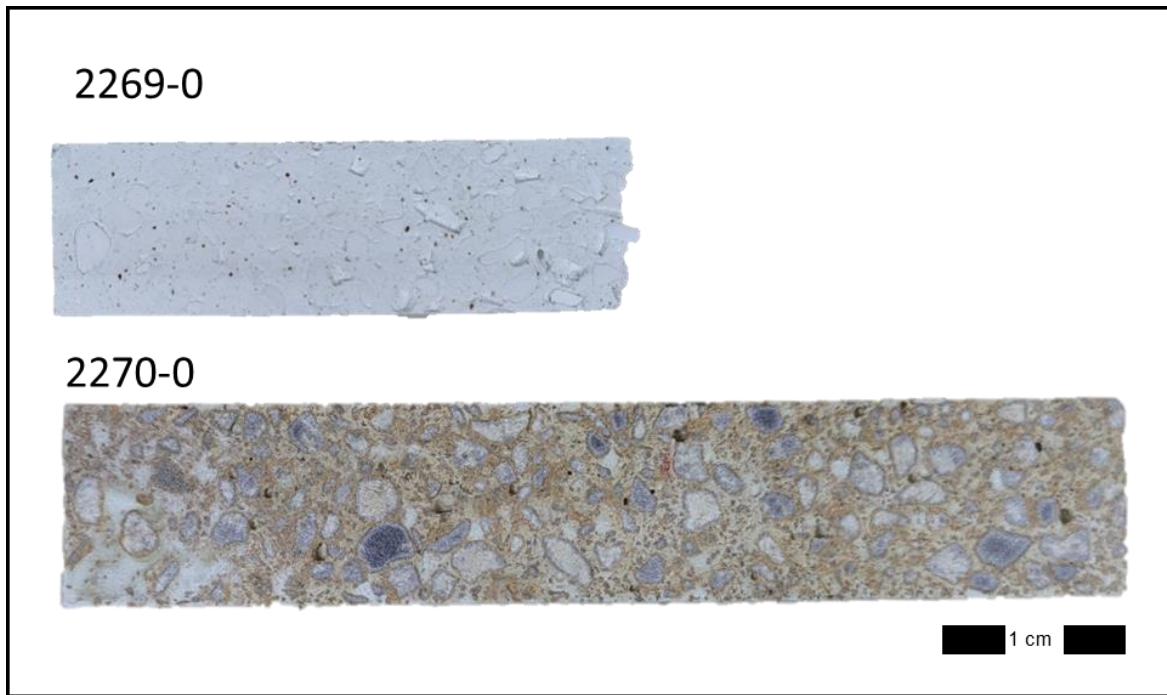
Figure 1: Overview of the two materials examined before the trials

Figure 1 shows the two materials selected for the experiments in the hydrogen-containing atmosphere.

Table 1: Test matrix for the first material

Trial	Sample name	Experimental conditions		
		Temperature [°C]	Dwell time [h]	Atmosphere
1	2269-1, 2269-2, 2269-3	950	24	H₂/Ar
2	2269-4, 2269-5, 2269-6	950	96	H₂/Ar
3	2269-7, 2269-8, 2269-9	1300	96	H₂/Ar

Table 2: Test matrix for the second material

Trial	Sample name	Experimental conditions		
		Temperature [°C]	Dwell time [h]	Atmosphere
1	2270-1, 2270-2, 2270-3	950	24	H₂/Ar
2	2270-4, 2270-5, 2270-6	950	96	H₂/Ar
3	2270-7, 2270-8, 2270-9	1300	96	H₂/Ar

A tube furnace from Therm-Aix is used for the tests to be carried out. The entire furnace design can be seen in Figure 2. It is possible to set and maintain a defined atmosphere in this furnace. The furnace consists of a furnace housing and the furnace tube, which is heated electrically via resistance elements. For the present work, a furnace tube (inner diameter 55 mm) consisting of α-Al$_2$O$_3$ with a purity of more than 99.5 % and a maximum operating temperature in air of 1950 °C is used. With these parameters, it is chemically inert, resistant to high temperatures, has a high mechanical strength and is therefore well suited for the planned reduction experiments. Both pipe ends are sealed with metal flanges to ensure a constant atmosphere through the internal seals. Both flanges each have 5 connections, 4 of which are provided for cooling the

HYINHEAT

flange seals by a water pipe and one connection for the gas inlet or gas outlet. Next to the furnace are cylinders of the desired gas (here: argon green and hydrogen red), which are connected to the gas inlet via rotameters. These rotameters can be used to set the desired volume flow of 25 l/h. With this setup, it is possible to feed either hydrogen or argon into the tube furnace. The resulting exhaust gas is passed through two wash bottles filled with water to prevent the exhaust gas from flowing back into the furnace due to the resulting overpressure. Another positive side effect is that solid particles contained in the gas flow are collected and do not clog the flue gas pipes.
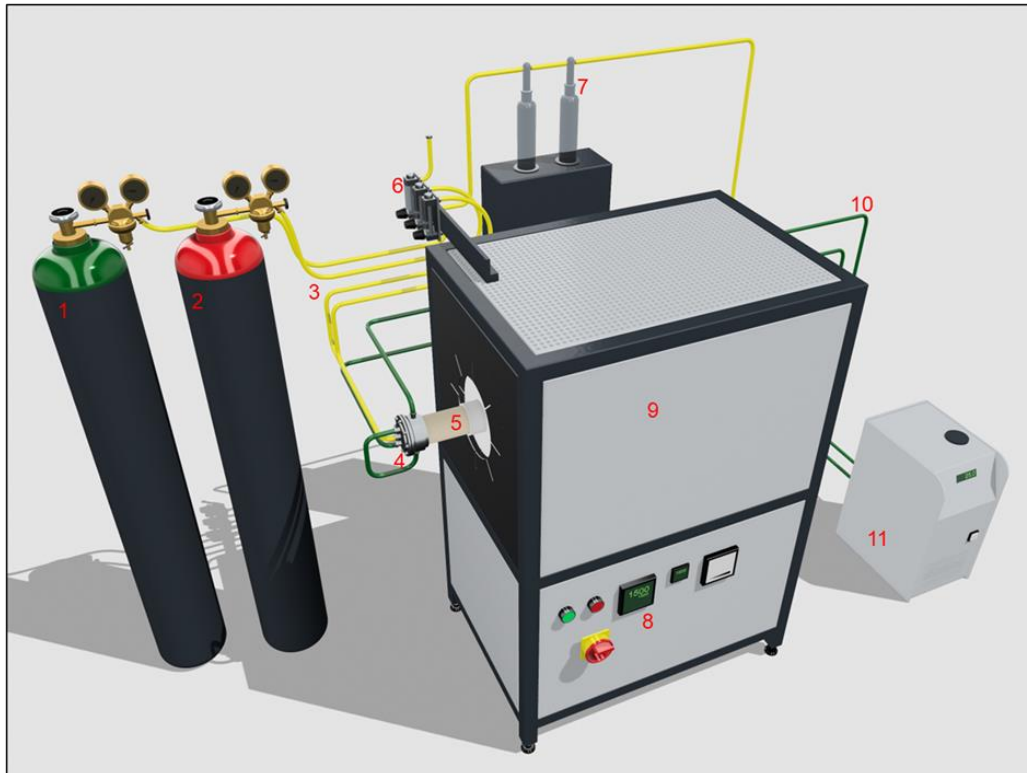
Figure 2 Experimental setup. 1 = Argon; 2 = Hydrogen; 3 = Gas pipe; 4 = Flange; 5 = Stovepipe; 6 = Flow meter; 7 = Wash bottle; 8 = Furnace control; 9 = Furnace housing; 10 = Cooling water pipe; 11 = Water cooling

Before the aging tests are carried out in the hydrogen-containing atmosphere, the exact weight of each sample is determined by weighing with a precision balance and then the open porosity and bulk density are determined. Three samples of the same material are then placed on sample holders made of a class 34 lightweight refractory brick (Al₂O₃ content 99 %) and placed in the middle of the tube (Figure 3). The sample holders are used to prevent contact between the samples and the tube in order to prevent possible damage to the tube. Furthermore, this ensures that there is an even flow around the samples. Each test is carried out with three samples in order to be able to document any interactions that may occur between the samples. After placing the samples in the tube, a cylindrical plug made of the same material as the sample holders is placed between the flange at the gas inlet and the samples as well as between the flange on the exhaust gas side and the samples. The diameter of the plug is 55 mm, the same as the inside diameter of the pipe. An inner drilling with a diameter of 12.5 mm ensures that a gas flow is guaranteed. The plug is primarily used as a radiation shield to protect the flange seals from overheating and thus ensure the tightness of the tube. A side effect of the plugs is that the material in the gas flow can be deposited there. After closing the flanges, the control module can be used to program the furnace to the appropriate program. Before the furnace is started, the tube is purged with argon to create an inert atmosphere. Once the desired holding temperature has been reached, the inert gas (90 % Argon and 10 % H₂) is turned on. As soon as the furnace has cooled down again, the inert gas is turned off and the tube is purged with argon until it is opened. After cooling, the samples can be removed from the tube and prepared for further analysis. The inside of the furnace tube is then examined for any deposits that may have formed and cleaned if necessary.
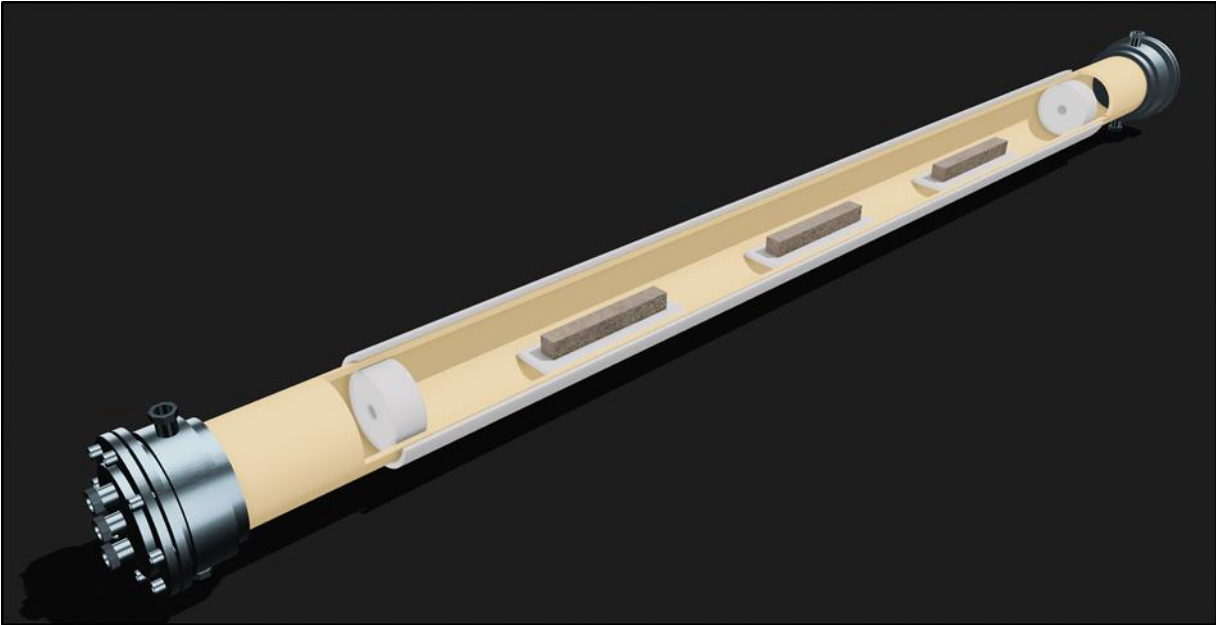
Figure 3 Sample placement in the tube

A.2 Results of the experiments

This section presents the results of the tests carried out. First, an optical assessment of the test specimens is carried out. The results of the X-ray fluorescence analysis, X-ray diffraction, electron microscopy and porosity measurements are then presented. Furthermore, the change in mass is determined for each sample. This value is a very good first point of reference for making statements about a possible reduction of components.

A.2.1 Visual inspection
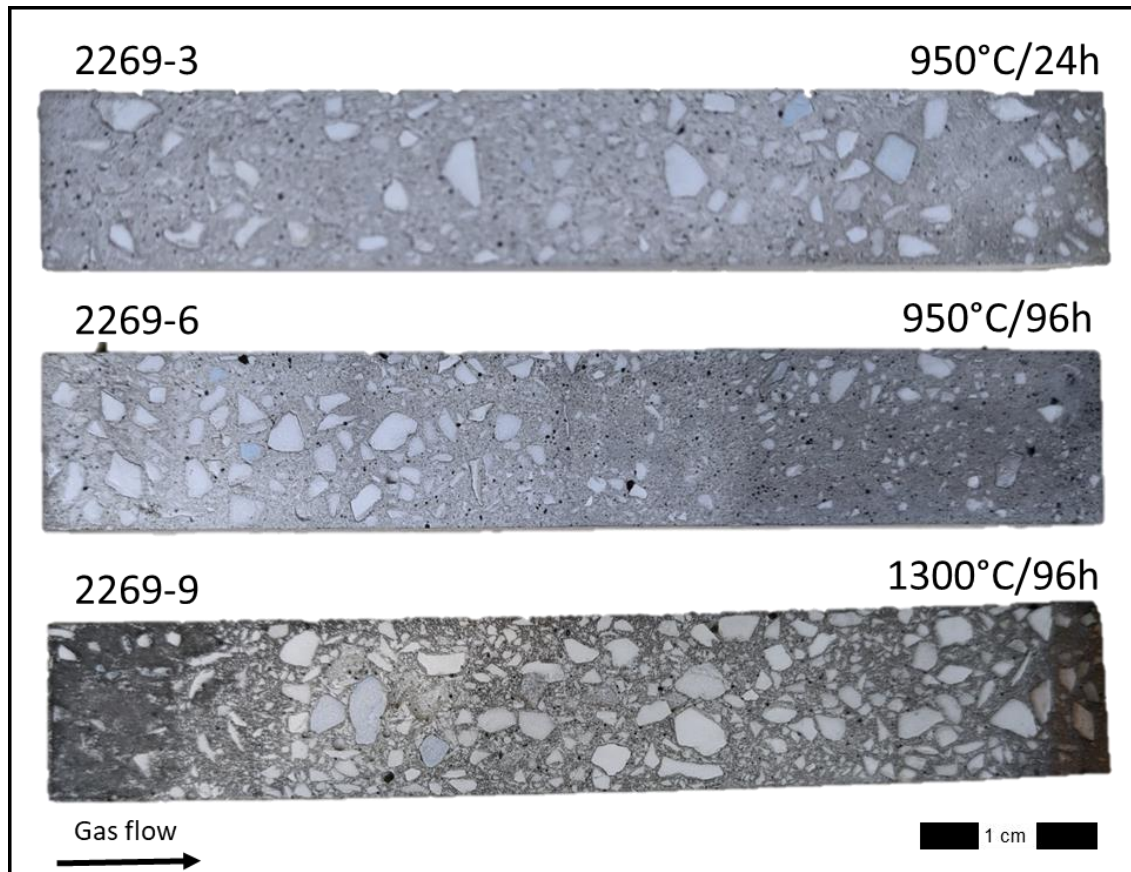
Figure 4 Optical comparison of the material 2269 after the various tests

Figure 4 shows an exemplary sample of material 2269 after the aging tests in the hydrogen-containing atmosphere. These images can initially be compared visually with the original appearance of the samples, which can be seen in Figure 1. It is noticeable that the samples have discolored to varying degrees. The sample that was aged at 950 °C for 96 hours is visually darker than the sample that was only aged for 24 hours. In addition, the areas with this corrosion phenomenon are larger. In the case of the sample that was aged at 1300 °C, it is noticeable that a clear change has occurred both at the beginning and at the end of the sample. Furthermore, it can be observed that the end of the sample not only shows a dark discoloration, but has also taken on a reddish color. The dark discoloration of the sample is due to the formation of oxygen vacancies, which are formed by the reduction of certain components. These oxygen vacancies make the sample appear dark. The reddish discoloration of sample 2269-9 is probably due to the accumulation of reduced iron close to the outlet of the sample. Figure 5 shows the samples of material 2270 after the aging tests. Discoloration can also be seen in these samples, which is due to the phenomenon already described. A green-bluish discoloration can also be observed in these samples, the cause of which has not yet been clarified beyond doubt.
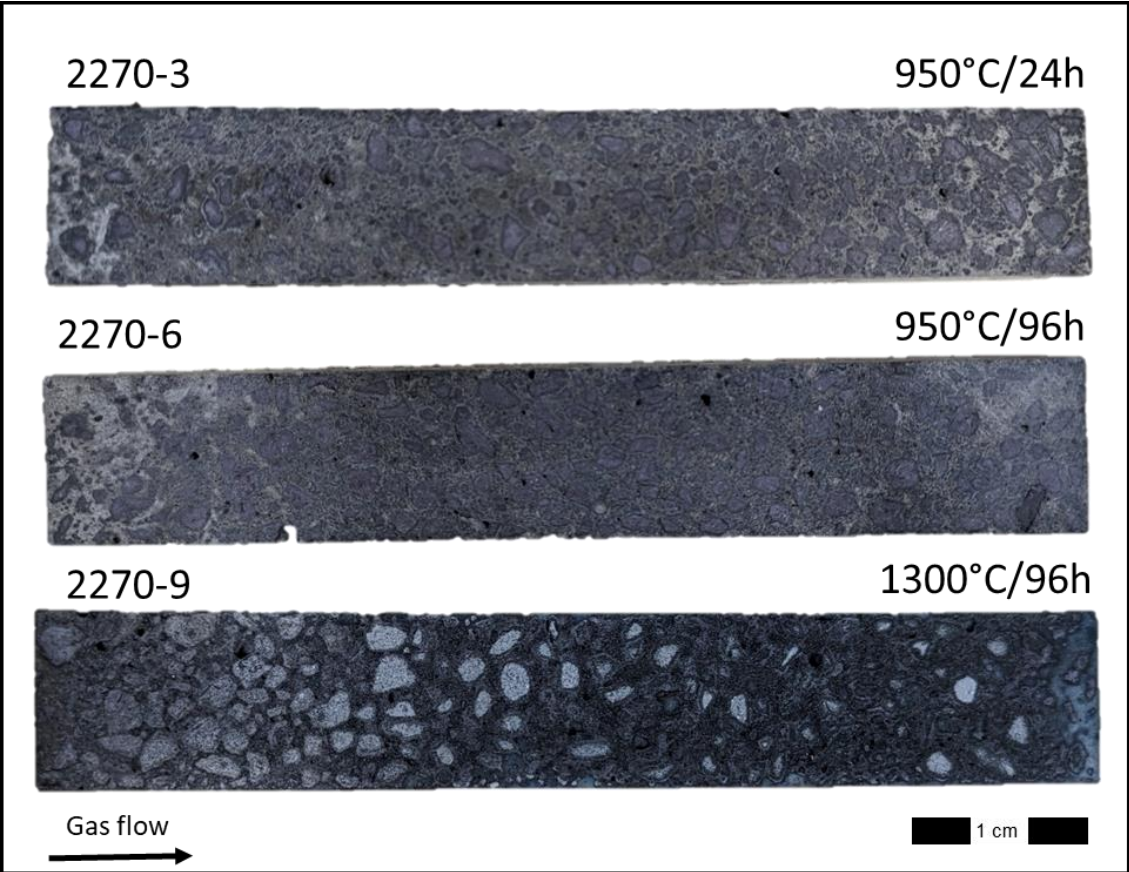
Figure 5 Optical comparison of the material 2270 after the various tests

A.2.2 Mass balance

Another indicator for the evaluation of the tests is the mass balance. As the samples are stored in a reducing atmosphere, it can be assumed that the mass of the individual samples' changes. For this observation, the samples are weighed at the beginning and after the tests in order to document any mass change that may occur with the aid of Formula 2-1. The change in mass is then shown in a diagram.

$$percentage\ weight\ loss = \left(\frac{m_{before}}{m_{after}} - 1\right) \cdot 100\% \qquad \{2\text{-}1\}$$
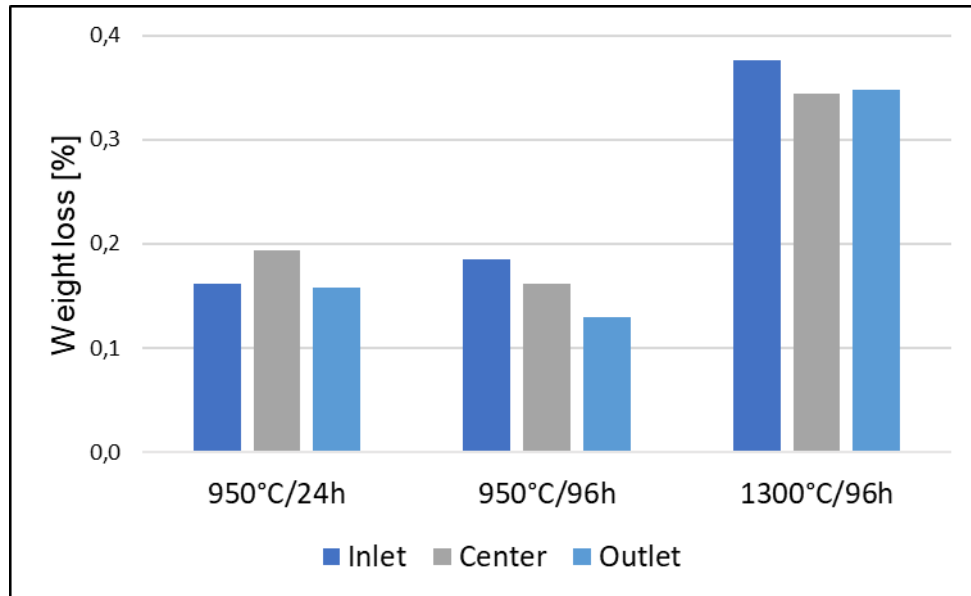
Figure 6 Representation of the percentage weight loss of the various trials for material 2269
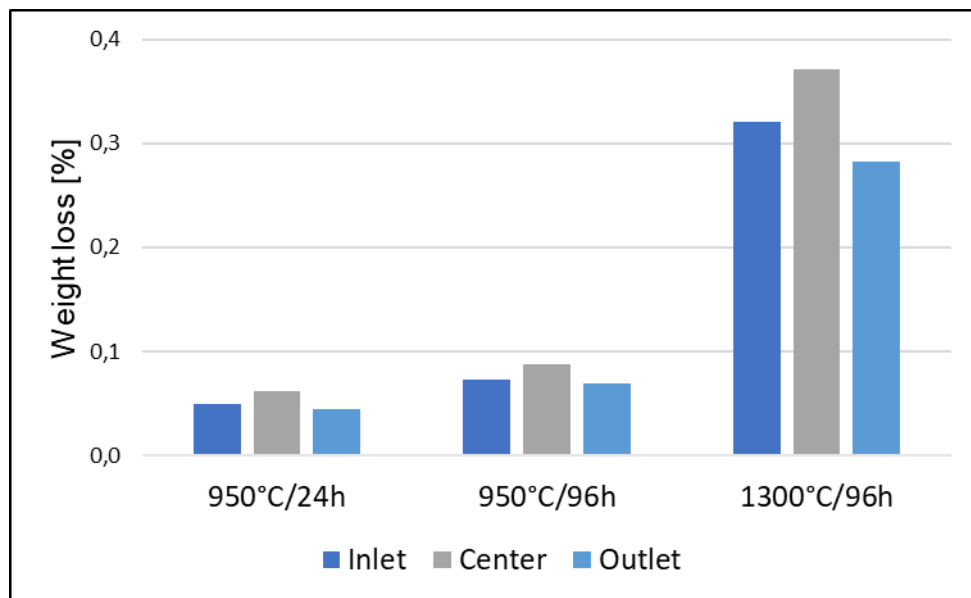
Figure 7 Representation of the percentage weight loss of the various trials for material 2270

Figure 6 and Figure 7 show the calculated percentage weight losses of the samples from the respective tests. It can be seen that three samples were always placed in the tube for each test. This results in the different designations for the three samples (inlet, center, outlet), which can be seen in the diagram. Despite the different holding times at 950 °C, there were no significant differences in the percentage weight loss for the samples made of material 2269. The mass losses here are between 0.1 and 0.2 percent. This observation can

HYINHEAT

also be made in the tests with material 2270. However, the mass losses here are between 0.0 and 0.1 percent. For both materials, however, an increase in mass loss can be observed at the higher temperature. Here, mass losses of up to 0.37 percent are recorded for both materials. This weight loss initially appears to be quite small. However, it should be noted that the tests only had a maximum holding time of 96. As the refractory material normally remains in the furnace for years, it is necessary to investigate how the weight loss develops over longer holding times in order to see whether this loss continues to increase or remains constant after a certain time.

A.2.3 Composition of the samples

X-ray fluorescence analysis is used as an analytical method to determine the chemical composition of a sample. To determine both the chemical composition and the phase constituents, a sample is ground to a particle size ≤ 63 μm using a vibrating disk mill. First, the loss on ignition of the sample is determined, whereby at least 2 g of the sample is annealed in a ceramic crucible at 1050 °C for 2 hours. The sample is then cooled to room temperature and weighed to determine the loss on ignition. In the next step, the annealed sample is mixed with a suitable digestion agent (consisting of 66.67 % lithium tetraborate, 32.83 % lithium metaborate and 0.5 % lithium bromide) and melted in the "LeNeo" melting furnace to form a glass compact. The glass compact is produced using different temperature and time programs. The chemical composition of the glass compact is determined with the aid of a wavelength-dispersive X-ray fluorescence spectrometer using a Rh tube. An X-ray fluorescence spectrometer from PANalytical (model: PW2404) is used for this. The results are evaluated using the iQ device software, whereby the results obtained are given as an oxide.

The so-called loss on ignition is also determined as part of the sample preparation. The loss on ignition provides information about the proportion of volatile components in the sample to be analysed. In addition, the analytical conversion allows conclusions to be drawn about chemical reactions such as oxidation processes. The analysis is carried out at 1050 °C in an air atmosphere. In this atmosphere, substances that have not yet been oxidized can oxidize or volatile components can evaporate. This leads to a detectable mass loss (positive loss on ignition) or mass gain (negative loss on ignition).

HYINHEAT

Impact of H_2 heating on product quality, yield, and refractory

Table 3: Representation of the chemical analyses of the test series of material 2269

wt.-%	2269-0	2269-2 950°C/24h	2269-5 950°C/96h	2269-8 1300°C/96h
SiO_2	0,62	0,54	0,52	0,57
Al_2O_3	89,36	89,99	89,74	89,65
Fe_2O_3	0,17	0,16	0,16	0,17
CaO	3,33	3,13	3,21	3,31
K_2O	0,00	0,09	0,09	0,00
Na_2O	0,17	0,15	0,17	0,03
MnO	0,01	0,01	0,01	0,01
BaO	6,13	5,73	5,89	6,10
SrO	0,16	0,15	0,15	0,16
SO_3	0,05	0,05	0,06	0,00
Total	100	100	100	100
loss of ignition (1050 °C)	0,04	0,03	0,02	0,00

Table 4: Representation of the chemical analyses of the test series of material 2270

wt.-%	2270-0	2270-2 950°C/24h	2270-5 950°C/96h	2270-8 950°C/96h
SiO_2	22,52	23,12	22,89	22,91
Al_2O_3	63,79	63,37	63,82	63,83
Fe_2O_3	1,14	1,18	1,15	1,15
TiO_2	2,12	2,15	2,19	2,18
CaO	3,49	3,37	3,31	3,31
K_2O	0,16	0,18	0,16	0,16
Na_2O	0,09	0,14	0,10	0,11
MnO	0,00	0,00	0,00	0,01
Cr_2O_3	0,01	0,01	0,01	0,01
P_2O_5	0,07	0,08	0,07	0,07
ZrO_2	0,05	0,05	0,05	0,05
BaO	6,39	6,18	6,05	6,05
ZnO	0,00	0,17	0,03	0,00
SrO	0,17	0,00	0,17	0,16
SO_3	0,00	0,00	0,00	0,00
Total	100	100	100	100
loss of ignition (1050 °C)	0,07	-0,02	-0,01	-0,32

HYINHEAT

Impact of H₂ heating on product quality, yield, and refractory

Table 3 and Table 4 show the results of the chemical analyses of the various test series. In addition to a sample that was analysed after sintering, one of the three samples is analysed using XRF for each of the tests performed. The samples of material 2269 consist of 89 wt.-% Al_2O_3. This material can therefore be identified as high alumina refractory concrete. Furthermore, it was found to contain over three percent calcium oxide. For this reason, it is a so-called medium cement castable. Another major component is barium oxide. This barium is added as barium sulphate ($BaSO_4$). Following the sintering process, the sulphur evaporates while the barium reacts with other components in the raw material, for example to form barium hexaaluminate ($BaAl_{12}O_{19}$) or Calsian ($BaAl_2Si_2O_8$). The compounds consisting of barium then provide the necessary anti-wetting effect that is required when using a material in a melting furnace in order to prevent wetting and possible infiltration of the material. In order to ensure safe operation of the furnace after conversion to firing with hydrogen, it is necessary to investigate the influence of the hydrogen combustion atmosphere in more detail. In addition to barium, small quantities of other oxides such as silicon dioxide are also present. After the experiments in the hydrogen-containing atmosphere, it can be determined that the chemical balance has not changed significantly. The changes observed can also be explained by the measurement inaccuracy of the device or an inhomogeneous distribution of raw materials. Material 2270 can be identified as an Al_2O_3-SiO_2-based material, which consists of CaO, Fe_2O_3 and TiO_2 in addition to Al_2O_3 (64 wt.-%) and SiO_2 (22.5 wt.-%). This material also contains barium oxide (BaO), which performs the task already described. No significant changes in the chemical balance were recorded in this case either. In the present series of tests, however, it is noticeable that there is a negative loss on ignition. A negative loss on ignition means that there was an increase in weight during the analysis. This leads to the conclusion that components of the sample were reduced in the hydrogen-containing atmosphere and then oxidized again during the analysis.

HYINHEAT

X-ray diffractometry is carried out using a D8 Advance Theta/Theta goniometer from Bruker in a Bragg-Brentano arrangement. A copper tube, which emits Cu radiation at a wavelength of λ = 1.54060 Å, is used together with a nickel filter. The tube power is 40kV/40mA. Before the measurement, a piece of the respective sample is taken and ground to a size of 63 μm before the ground powder is placed in the diffractometer with a sample holder. The measurement of each individual sample is carried out from 5° to 90° over a measurement period of two hours. The step size is 0.01°. The deflected intensities as a function of 2θ are measured by the LynxEye detector used. The subsequent phase assignment of the resulting diffractogram can be carried out with the help of Powder Diffraction Files (PDF-2-2021), a reference database, in the programs EVA and TOPAS.

Table 5: Results of the phase analysis of material 2269 before and after the various trials

	Corundum (Al_2O_3)	Barium hexaaluminate $(BaAl_{12}O_{19})$	Celsian $(BaAl_2Si_2O_8)$	Grossite $(CaAl_4O_7)$	Hibonite $(CaAl_{12}O_{19})$	Cristobalite (SiO_2)
2069-0	+++	++	-	+	+	-
2069-2	+++	++	-	+	+	-
2069-5	+++	++	-	+	+	-
2069-8	+++	++	-	+	+	-

Table 6: Results of the phase analysis of material 2270 before and after the various trials

	Mullite (Al_2O_3)	Corundum (Al_2O_3)	Celsian $(BaAl_2Si_2O_8)$	Anorthite $(CaAl_2Si_2O_8)$	Hibonite $(CaAl_{12}O_{19})$	Cristobalite (SiO_2)
2070-0	+++	++	++	++	+	+
2070-2	+++	++	++	++	+	+
2070-5	+++	++	++	++	+	+
2070-8	+++	++	++	++	+	+

Corundum was identified as the main phase for material 2269. The aforementioned barium, which is responsible for the non-wetting properties, is mainly present in combination with aluminum as barium hexaaluminate. Grossite and hibonite have been identified as minor phases. Traces of celsian and cristobalite are also present. In material 2270 examined, mullite was found to be the major phase. However, corundum is also present as a minor phase. The calcium in the sample is present as anorthite and hibonite. The barium is present in combination with aluminum and silicon as celsian. Cristobalite is also present. As with the chemical analysis, no major changes in the composition could be detected in the phase analysis after the tests.

A.2.4 Porosity

The bulk density and open porosity are determined in accordance with DIN EN 993-1. For this purpose, the test specimens are dried to constant mass, the mass (m_d) is determined by weighing and then placed in a vacuum chamber whose pressure is lowered. This pressure is kept constant for 30 minutes in order to remove the air from the open pores of the test specimens. After this half hour, the vacuum chamber is filled with water at (20 ± 5) °C until the samples are completely covered with water. The pressure is then kept constant for a further half hour. The vacuum chamber is then vented and the specimens are left in the water for a further 30 minutes. For the bulk density and the open porosity, the masses of the test specimens under water (m_h) and the masses of the test specimens saturated with water (m_s) are determined. For this measurement, the test specimens are wiped with a damp cloth and then weighed.

The bulk density is the ratio between the mass of a dry porous body and its total volume and can be determined according to DIN EN 993-1 using the following equation:

HYINHEAT

Impact of H₂ heating on product quality, yield, and refractory

$$\rho_b = \frac{m_d}{m_s - m_h} * \rho_{liq}$$

{2-2}

The density of water at 20 °C is 0.9982 g/cm^3. The open porosity is the ratio between the volume of open pores of a porous body and its total volume and can be determined with the standard DIN EN 993-1 using the following equation:

$$\pi_a = \frac{m_s - m_d}{m_s - m_h} * 100$$

{2-3}
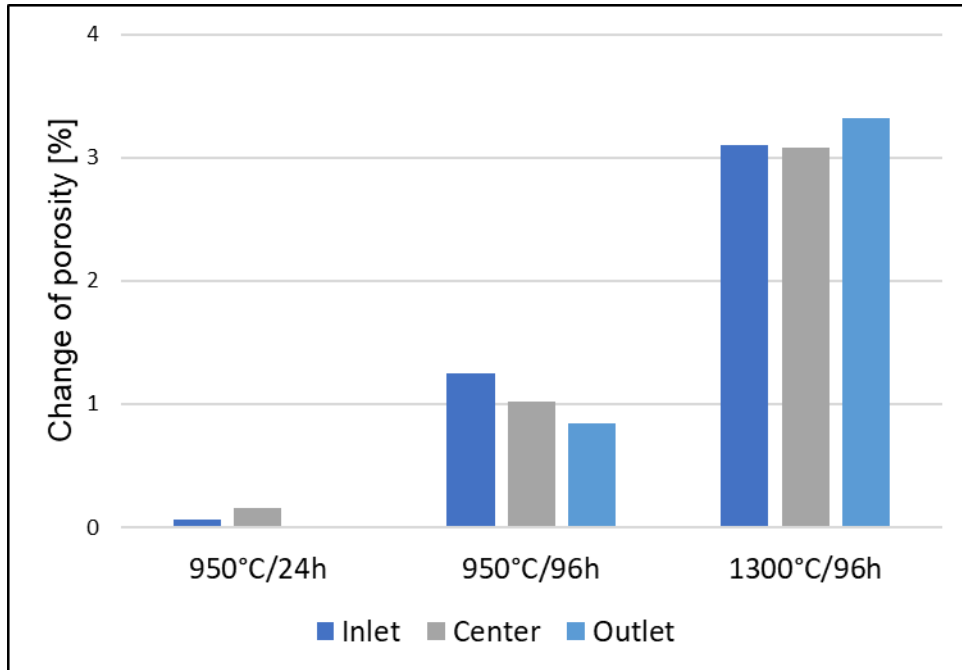
Figure 8 Representation of the percentage change pf porosity of the various trials for material 2269

HYINHEAT
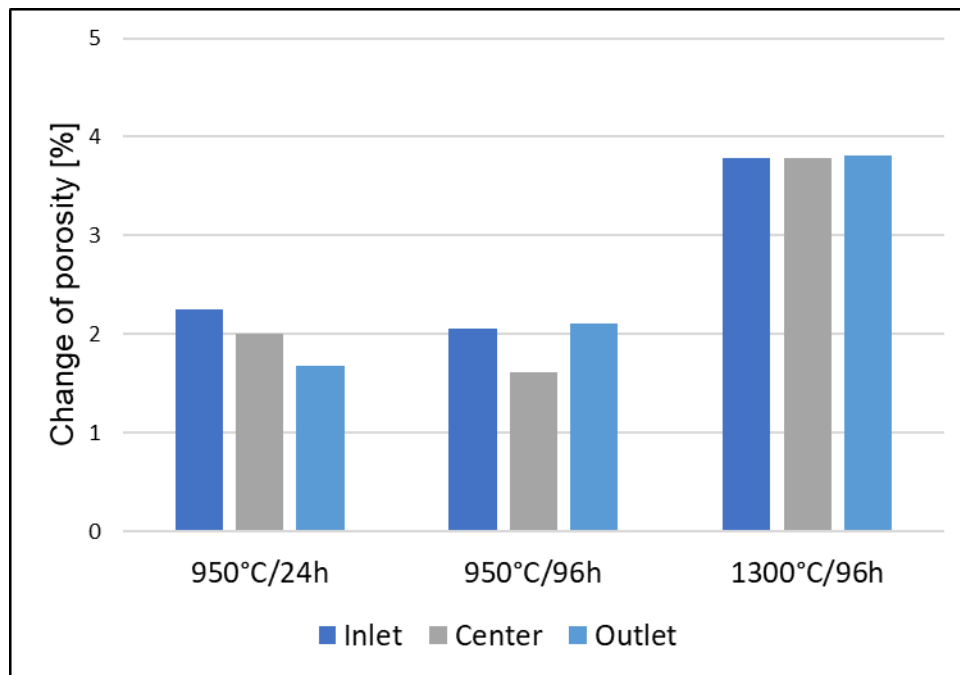
Figure 9 Representation of the percentage change pf porosity of the various trials for material 2270

The open porosity is determined for each individual sample before and after the tests. The exact procedure has already been described. To illustrate the change, the results are given as percentage changes and not as absolute values. As with the mass change, the results are sorted according to the position in the oven and shown in a bar chart. No significant change was observed during the test (950 °C/24 h) with material 2269. The porosity only increased slightly. However, at a holding time of 96 h, a change in porosity of over one percent was observed in the first sample. The other two samples were just below this. However, a greater change was observed in the 1300 °C tests. In this case, the porosity increased by more than 3 percent in each case. This change can also be observed for the same conditions for material 2270. Here, the porosity increased by more than 3 percent. However, differences can be observed between the materials. Material 2270 already showed an increase of approx. 2 % in the tests at 950 °C. This applies both for a holding time of 24 hours and for a holding time of 96 hours.

A.2.5 Microstructure

To carry out the microstructural analysis in the Zeiss scanning electron microscope (GeminiSEM 500 model), a sample from each test series is first selected for analysis. Care must be taken to ensure that each sample was in the same position in the tube furnace in order to ensure comparability between the different tests. Each sample is then cut to size using a diamond-coated saw and placed in a prepared plastic mold. This mold is then filled with a mixture of epoxy resin and hardener to ensure the surface hardness of the samples and to obtain a smooth, even surface for microscopic observation. By placing the samples in a vacuum chamber, the epoxy resin penetrates into the samples through the open porosity and thus ensures further stabilization of the samples. After curing, the specimens are removed from the mold to be ground and polished in the next step using a QATM grinding and polishing machine (model Saphir 550). This step is necessary because the sample is often uneven after embedding. This can lead to the electron beam of the scanning electron microscope not hitting the sample evenly and thus impairing the quality of the images. Grinding and polishing are each carried out in three steps, with the grain size of the grinding and polishing paper decreasing from 250 µm to 0.25 µm. After these preparation steps and before being placed in the microscope, the samples are vaporized with carbon to make them conductive for the electron beam. For each sample, SEM images of the edge and the center of the sample are taken so that they can be compared with each other.

A.3 Thermodynamic calculations

In addition to all these experimental results, it is also possible to carry out theoretical thermodynamic calculations using FactSage. The so-called closed model is mainly used for the calculation of these

HYINHEAT

experiments. In a closed system, the entire gas volume reacts with the predetermined species. In this case, however, it is easier to follow the reactions as a function of temperature.

Over the past few months, a database has been created for deliverable 1.1 that contains information on the materials used in all furnaces. Thermodynamic calculations can be carried out on the basis of this information. This makes it possible to estimate how the various materials might behave in the different atmospheres before the experiments. In summary, it can be said that mainly common materials are used in the ovens. This is practical as the thermodynamic calculations performed help to obtain information about several furnaces. One of the most commonly used materials is fireclay. Fireclay consists mainly of Al_2O_3 and SiO_2. This also corresponds to the composition of the material described in the previous sections. For this reason, it is useful to perform thermodynamic calculations with a fireclay composition.
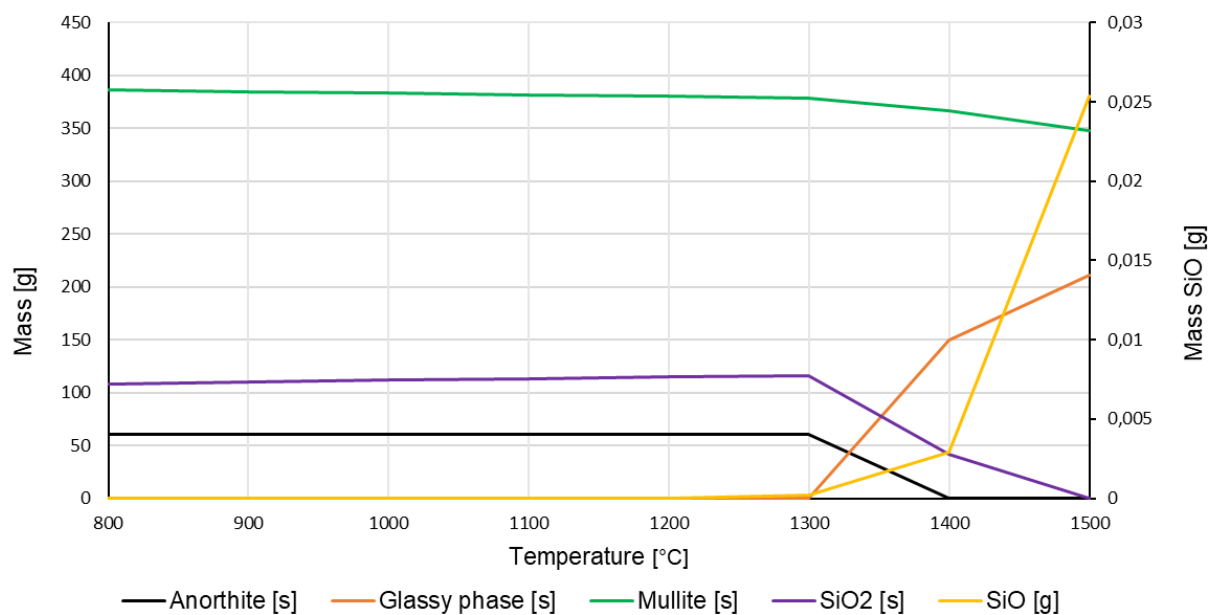
Figure 10 Representation of a thermodynamic calculation of a fireclay in the test conditions used

The exemplary calculation illustrates the already known corrosion phenomena and thus agrees with the results of studies already carried out in a hydrogen-containing atmosphere. The figure shows that the fireclay system remains stable up to a certain temperature. According to FactSage, changes can only be observed above a temperature of 1300 °C. For example, a constant mass loss can be observed for mullite from 1300 °C. This is mainly due to the fact that the SiO_2, which forms the mullite together with Al_2O_3, is reduced to gaseous SiO. This gaseous SiO then evaporates from the sample and thus leads to a mass loss. At the same time, according to the literature, a separation of Al_2O_3 is described, which would explain an increase in the Al_2O_3 content. This described reduction of SiO_2 is the reason why the free SiO_2 content also decreases. These reactions can also be recognized by the fact that the mass of gaseous SiO increases from this temperature. Furthermore, a decrease in anorthite and an increase in a glass phase can be observed. This is due to the fact that the anorthite forms a deep-melting phase together with alkalis, resulting in the formation of a recognizable glass phase.

HYINHEAT

A.4 Conclusion

The results of the tests on promising refractory materials were presented in the previous chapters. In collaboration with the company Speira, an inspection of an aluminum melting furnace was carried out in order to identify the materials on which it makes sense to carry out various laboratory tests. These are necessary to ensure that the furnace can be safely converted to hydrogen firing. As part of this first step, the methods that can be used to assess the materials were presented. In addition to visual inspection and the determination of mass changes, chemical analyses using X-ray fluorescence analysis, phase analyses using X-ray diffraction, changes in open porosity and microstructure analyses using a scanning electron microscope are particularly important. These investigations have already been carried out on the materials to be examined. However, it should be noted that further results, such as the results of the microstructure analysis, are still pending. In addition, results from investigations of other materials from other furnaces are expected from other partners. Results from tests in a different atmosphere are also expected. The other atmospheres are closer to the hydrogen combustion atmosphere. The following atmospheres are initially planned:

- 0 % H$_2$ with the other gas components: H$_2$O, O$_2$, CO$_2$, CO, N$_2$, H$_2$
- 50 % H$_2$ with the other gas components: H$_2$O, O$_2$, CO$_2$, CO, N$_2$, H$_2$
- 100 % H$_2$ with the other gas components: H$_2$O, O$_2$, N$_2$, H$_2$

Finally, it is worth focusing on one aspect of refractory materials. Previously published studies have investigated the effect of hydrogen combustion atmospheres on the main components of refractory materials. The influence on corundum, mullite and silica was analysed in more detail. These results are also consistent with the results of the present work and also with the theoretical results calculated with FactSage. However, it is important to investigate the influence of the atmosphere on components with a lower content. components of the binding matrix have not yet been investigated in detail. Furthermore, the effect on functional additives such as the aforementioned barium compounds should be investigated in more detail in order to ensure a safe conversion of the furnace.

HYINHEAT

B. Effect of H₂/oxyfuel use on scale formation

B.1 Introduction

B.1.1 Goals and background

International pacts such as the Paris Agreement and the EU's Green Deal are enforcing steel producers to find major reductions in CO_2 emissions by the year 2050. Electrical heating, use of hydrogen as the fuel gas, or replacement of air as the oxidizer gas with oxygen (oxyfuel) are methods with potential to reduce the carbon footprint of the reheating process. Understanding and controlling the oxidation of steel during reheating is of economic interest, since the oxidation losses equal to 1-2% of the original metal. High adhesion of the oxide scale to the steel surface can also lead to descaling problems and later to surface defects, such as red scale formation during the hot rolling process.

The goals of this task were to produce information on scaling losses and changes to the structure of oxide scales formed in novel reheating conditions. Steel grades provided by SSAB were tested at the University of Oulu using thermogravimetric analysis (Figure 11). The formed oxide scales were studied with FESEM-EDS microscopy.

B.1.2 Experimental
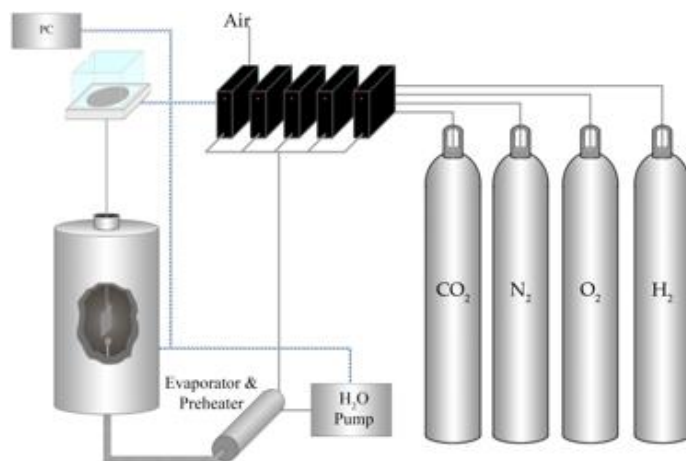
Figure 11. Layout of the thermogravimetric analyser used in oxidation testing.

The oxidation tests were conducted with a custom-built tubular thermogravimetric analyser (TGA). The TGA can hold a maximum temperature of 1500 °C and utilize gases N_2, CO, CO_2, H_2 and H_2O. The heating profile and gases are computer controlled. The mass of test samples is measured continuously throughout the experiments. The samples were cooled in the upper part of the furnace tube in inert nitrogen gas.

Larger steel pieces provided by SSAB were cut in smaller test samples with dimensions of 12 x 12 x 30 mm (±1 mm) at the University of Oulu. A hole of 2,5 mm was made to each sample for sample hanging. After cutting, the samples were polished and cleansed with ethanol and acetone. After oxidation tests, samples were cast in epoxy, cut and polished for FESEM analysis.

B.1.3 The research plan

Two different heating profiles were used. Heating profile "Curve 1" described a typical pattern with an elevation of temperature from 330 to 1250 °C combined with a holding time of 70 minutes at the maximum

HYINHEAT

temperature. With rapid heating (Curve 2) the temperature was raised from 360 to 1180 °C with no holding time. The used heating profiles are depicted in Figure 12.
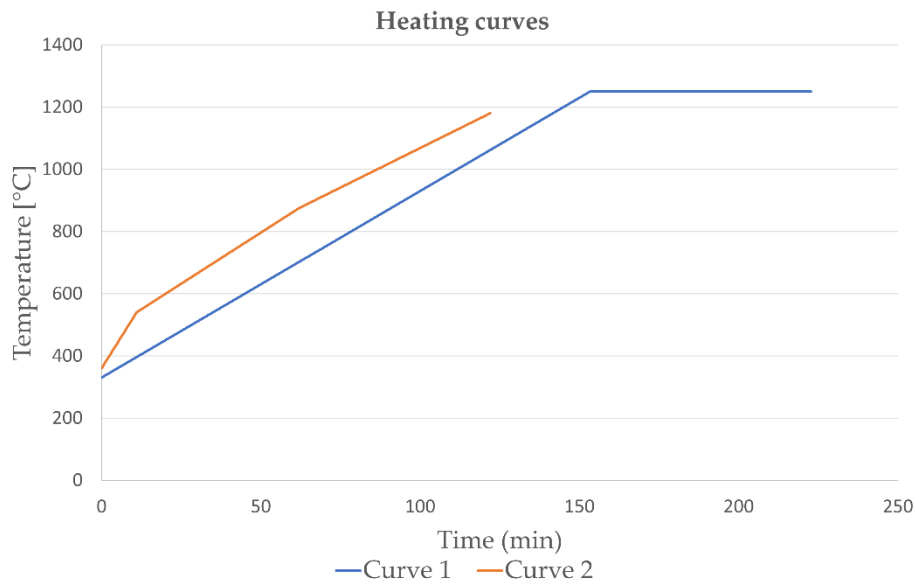
Figure 12. The two different types of heating profiles used in oxidation testing.

Seven different gas atmospheres were used, which included electrical heating, natural gas burn, H₂ and oxyfuel use in various combinations. The gas atmospheres are presented in Table 7.

Table 7. The gas atmospheres used in oxidation tests.

	Atm. 1	Atm. 2	Atm. 3	Atm. 4	Atm. 5	Atm. 6	Atm. 7
Fuel	Natural gas	Natural gas	H_2	H_2	H_2	NG+H_2 50:50	Electrical heating
Oxidizer	Air	Air	Air	Ox	Ox	Ox	Air
O_2	2,5	1	2,5	2,5	1	2,5	21
H_2O	16,4	17,8	30,8	97,5	99	83	-
CO_2	8,5	9,2	-	-	-	14,5	-
N_2	72,6	72	66,7	-	-	-	79

Four different steel grades were included in the study. The composition of these steel grades is presented in Table 8 with regards to the most relevant alloying elements affecting the oxidation process.

Table 8. The main residual/alloying elements affecting the oxidation process in the steel grades studied.

Steel grade	M1	M2	M3	M4
Si %	0,2	0,22	0,25	1,1
Ni %	0	1,3	2	0,7
Cr %	0,8	0,4	0,5	1,35

A research matrix was built around the two heating profiles, four steel grades and seven different gas atmospheres. This amounted to a total of 56 oxidation tests.

B.2 Scaling losses and kinetics

An example of oxidation kinetics is presented in Figure 13 for steel grade M1 using heating curve 1. The mass change curves for all four steel grades were somewhat similar with regards to atmospheres 1-6 and the order of oxidation was generally the same. A somewhat surprising result was the almost non-existent difference between atmospheres 4 (H₂-Oxyfuel) and 6 (CH₄:H₂-Oxyfuel) despite significant differences between the

HYINHEAT

gas compositions. The mass change curves in atmosphere 7 ("Electrical") were irregular and somewhat random. This result could be explained by poor adhesion of the oxide in a water vapor free gas atmosphere and loss of contact with the steel substrate.
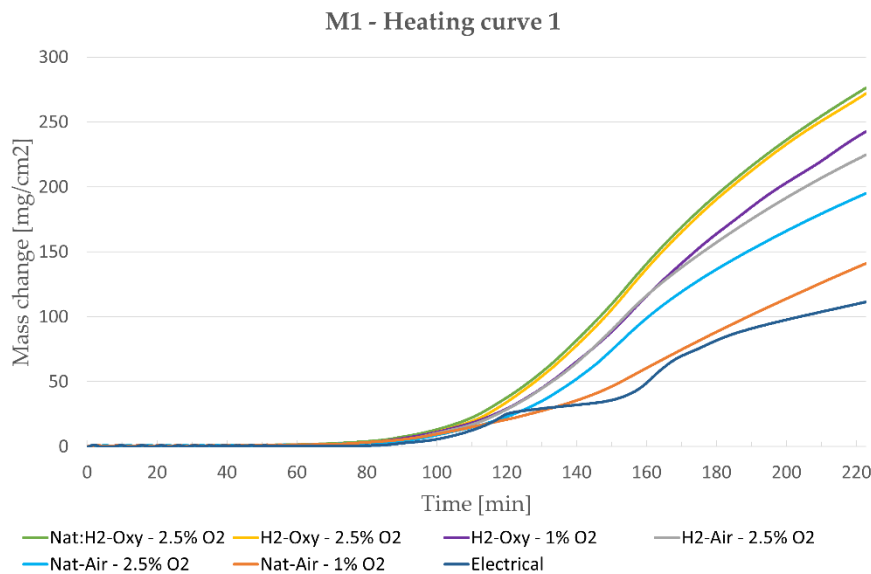
Figure 13. Oxidation kinetics for steel grade M1 when using heating curve 1.

The changes in oxidation when compared to the typical industrial scenario of "Natural gas–Air 2,5% O₂" are highlighted in Table 9. Change from natural gas to hydrogen produced a very modest (11,5-18,2%) increase in oxidation. The oxyfuel gas atmospheres with 2,5% free oxygen were by far the most oxidizing, producing an increase of nearly 50% in oxide formation. Whether or not oxyfuel gas atmospheres increase scaling losses in an actual industrial reheating furnace also depends on other factors, such as potential changes to the reheating time. Differences in scaling losses between free oxygen contents 2,5% and 1,0% were quite significant (in the range of 25-30%).

Table 9. Percentual changes in oxidation for heating curve 1 when compared to the reference gas atmosphere "Natural gas - Air – 2,5% O₂".

Heating curve 1	M1	M2	M3	M4	Mean
H₂ - Oxy – 2,5% O₂	39,5 %	50,6 %	56,5 %	50,4 %	49,3 %
Nat:H₂ - Oxy – 2,5% O₂	41,8 %	52,0 %	54,9 %	44,9 %	48,4 %
H₂ - Oxy – 1,0% O₂	24,5 %	36,5 %	36,6 %	23,9 %	30,4 %
H₂ - Air – 2,5% O₂	15,3 %	17,0 %	18,2 %	11,5 %	15,5 %
Nat - Air – 2,5% O₂	Baseline	Baseline	Baseline	Baseline	Baseline
Nat - Air – 1,0% O₂	-27,7 %	-28,5 %	-27,2 %	-33,3 %	-29,1 %
Electrical	-42,9 %	-43,2 %	-33,4 %	-38,6 %	-39,5 %

When using heating curve 2, the percentual changes in different gas atmospheres were of similar degree to heating curve 1. Heating curve 2 reduced the scaling losses consistently by about 65-70% compared to heating curve 1.

B.3 Changes in the structure of oxide scales

B.3.1 Adhesion of the steel–scale interface

Adhesion of the oxide scale to the steel substrate is one of its' most meaningful properties, as a strong adhesion can lead to issues during the descaling process. The effects of both the gas atmosphere and heating profile on the scale adhesion were estimated from high magnification FESEM-images taken from the steel-scale interface.

HYINHEAT

The interface of each steel grades had their own characteristic appearance, which is expected to be caused by differences in the contents of alloying/residual elements in the parent steels. However, no clear increase in oxide adhesion was seen in hydrogen, or oxyfuel gas atmospheres compared to natural gas. This result is in alignment with previous studies (Haapakangas et al. 2024, Luzzo et al. 2021).

In other words, the steel-scale interface between gas atmospheres was 1-6 for the most part very similar. The only clear difference was the interface in gas atmosphere 7: "Electrical". In this gas atmosphere there was generally a clear void in the lower wüstite layer. In the literature it has been stated that in gas atmospheres with no H_2O a separation occurs between the oxide and steel due to low plasticity of the oxide layer (Chen & Yuen 2013). Some examples of the steel-scale interface are presented in Figure 14. Therefore, no significant descaling issues are expected to be caused by the change in the case of H_2 or oxyfuel reheating. The adhesion of the oxide scale formed during electrical heating is possibly weaker.
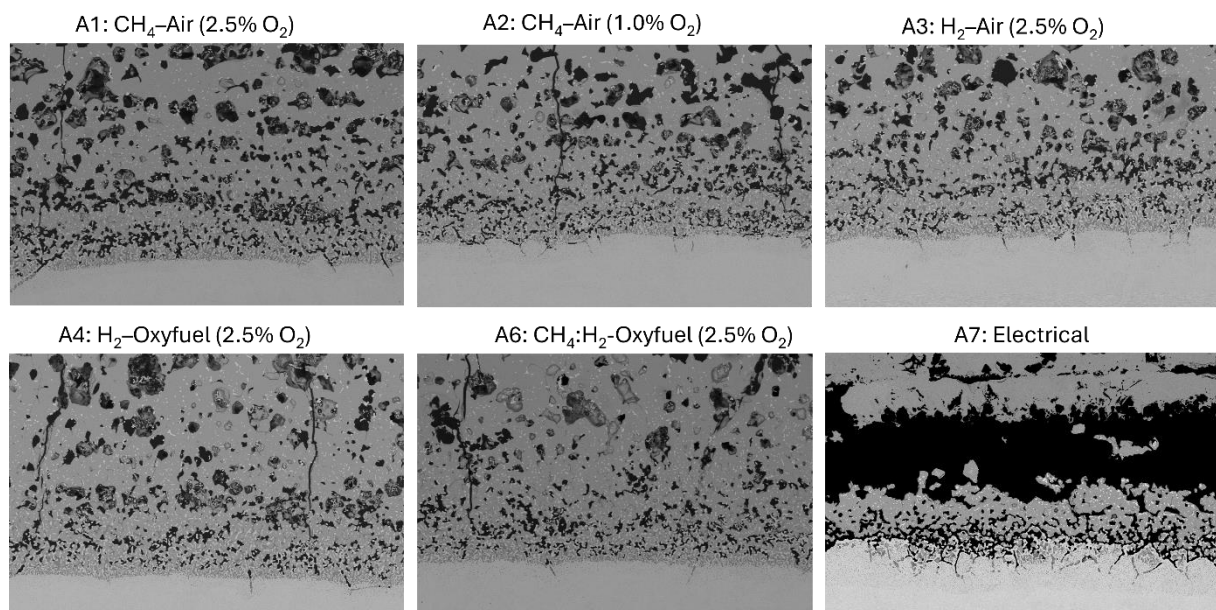
Figure 14. Steel-scale interface in different gas atmospheres for steel grade M2 using heating curve 1. 300x magnification.

B.3.2 Effects on the composition of iron oxides

Free oxygen content in the gas atmospheres was found to have a notable effect on the composition of the iron oxide layers. With a free oxygen content of 2,5% the surface generally had a clearly observable magnetite/hematite layer with a smooth surface. When the free oxygen content was decreased to 1,0% the magnetite layer was generally missing. The result was similar for both "Natural gas–Air" and "H2-Oxyfuel" gas atmospheres.

The surface of the oxide layer changed from smooth to irregular. Changes in the ratios of iron oxides can impact the descaling process since different oxides have their own physical properties. Some examples of the phenomena described above are shown in Figure 15. Examples on the effect of free oxygen content and electrical heating on the oxide scale composition.

Figure 15. Examples on the effect of free oxygen content and electrical heating on the oxide scale composition.

HYINHEAT
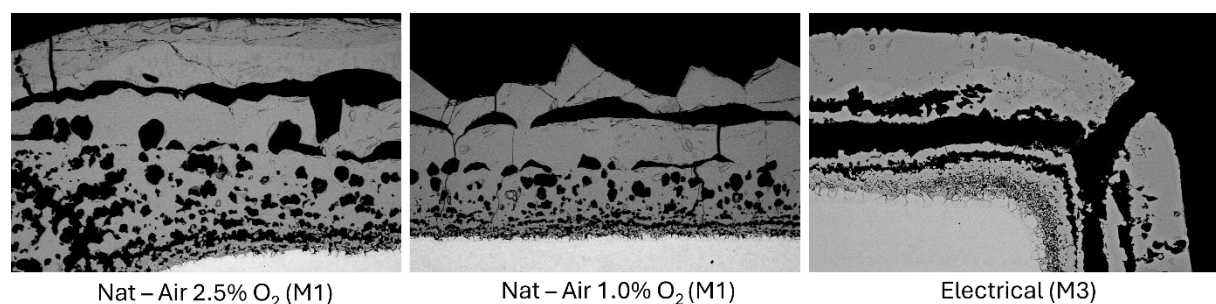
The free oxygen content, however, did not seem to have any effect on the adhesion at the steel-scale interface, or the enrichment of alloying/residual elements. Gas atmosphere 7 ("Electrical") generally produced oxide scales which were completely different from the other gas atmospheres. In general, they contained a much thicker magnetite/hematite layer on the surface, and a significant void inside the wüstite layer.

B.3.3 Enrichment of alloying elements

Certain alloying and residual elements in steel, such as Si, Cr or Ni, have a strong effect on both oxidation kinetics and the adhesion of the steel-scale interface. Especially silicon is known to have a strong influence on the adhesion of the oxide to the steel surface (Fukagawa et al. 1994). The enrichment of these elements in different gas and heating profiles was estimated using FESEM-EDS mapping.

Some examples of changes in silicon enrichment at the interface are shown in Figure 16. Gas atmospheres 1-6 had a subtle differences in the encrichment behavior. The strongest Si-network was formed in atmosphere 4 (H₂-Oxy). Electrical heating produced an Si-network notably less connected than the other gas atmospheres, which could be beneficial from a scale removal standpoint. The heating curve a remarkable effect on the enrichment of alloying elements, including silicon, as seen in Figure 16.
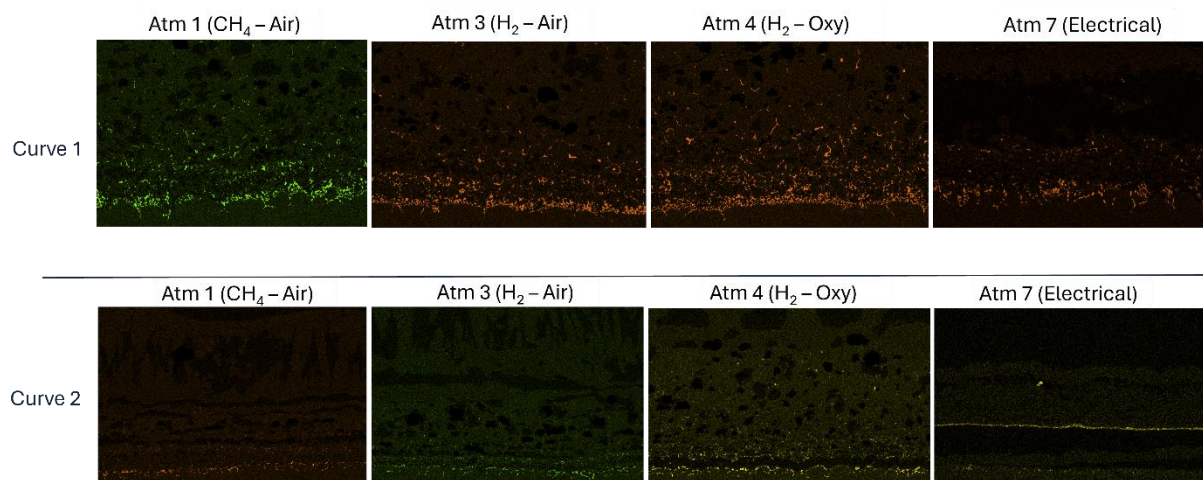
Figure 16. Examples of silicon enrichment of steel grade M2 in different gas atmospheres and temperature conditions.

HYINHEAT

C. Melting tests at Speira's 1.5 t lab scale melting furnace

C.1 Introduction

C.1.1 Overview of equipment and trial objectives

Speira's R&D facility uses a versatile tiltable 1.5t melting furnace to perform melting trials, which are positioned between lab scale experiments and small production units (Figure 17). In its basic configuration the furnace consists of a main (heating) chamber equipped with a 350 kW cold air burner and an external chamber, which has two connections to the heating chamber and can be modified to establish a melt circulation system to investigate different types of melt treatment and measurements of melt quality. In the scope of the HyInHeat project this furnace is used to analyze the impact of a fuel switch from natural gas to hydrogen on the melt quality, especially the formation of dross (oxidation of melt) and the pickup of hydrogen. For this purpose, the installed annular excess air burner was modified for hydrogen combustion and will be later replaced by a low temperature oxyfuel (LTOF) burner. The results in this report focus on the comparison of natural gas – air combustion and hydrogen - air combustion. The results of the LTOF trials will be reported in deliverable D5.3 of work package 5.
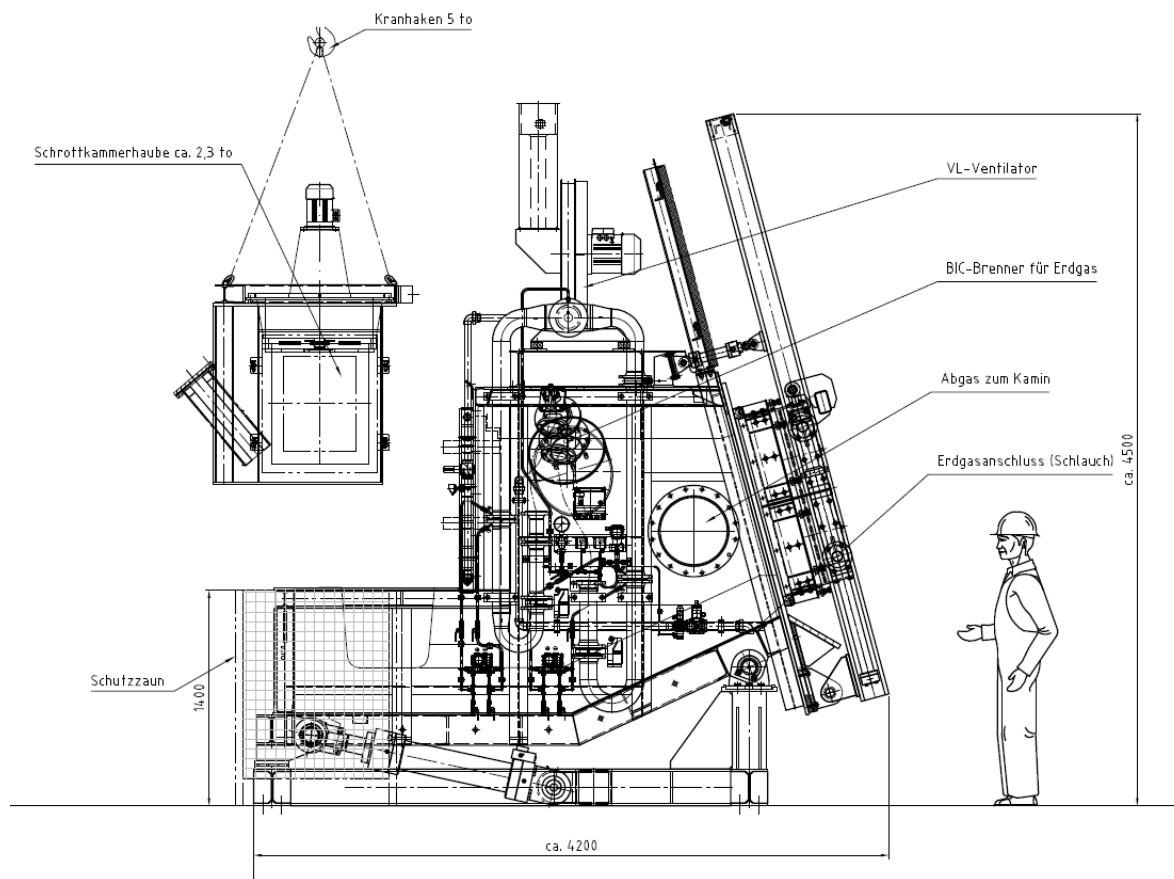
Figure 17: Drawing of 1.5 t lab scale melting furnace at Speira R&, 350 kW cold air burner, melting rate 200 kg/h

C.1.2 Background

Typical modern aluminium casthouses apply natural gas-fired melting furnace to supply the melt for the casting process to produce ingots, which can be rolled to sheet material. Modern regenerative burner systems have a specific energy consumption of less than 650 kW/t for liquid aluminium. In the scope of reduction of CO_2 emissions the replacement of natural gas by green hydrogen appears as a promising approach, because existing installations can be converted with a manageable effort, since properties of hydrogen do not differ so much from natural gas, as is indicated by a similar Wobbe index. The major

difficulties appear to be related to a higher flame temperature, which could lead to more oxidation of the melt i.e. increasing the dross formation and to the pickup of hydrogen in the melt.

C.1.2.1   Pickup of hydrogen

It is well known that aluminium melt in contact with water vapor leads to the oxidation of aluminium and the release of hydrogen, which is dissolved in the melt and can lead to serious problems of harmful porosity during the solidification process (Tiryakioğlu, 2020) (2021). In the further processing steps, the dissolved hydrogen must be removed by purging with inert gases like argon or nitrogen, which adds additional processing time and costs of consumables. The problem of hydrogen pickup in the melt is governed by Sievert's law which relates the equilibrium concentration of hydrogen in the melt to the water vapor partial pressure in the ambient atmosphere. Even in the combustion of natural gas the hydrogen pickup is a serious problem, since each CH_4 molecule generates 2 water molecules. In burner systems with air as an oxidizer the combustion products are strongly diluted by the nitrogen fraction in the air. Comparing air combustion of natural gas with hydrogen, the water vapor content of the combustion gases is roughly twice as much in the case of hydrogen. Due to Sievert's law this results only in a 40% increased hydrogen pickup in the melt. Although this could increase the processing time, the problem seems to be controllable from a technical point of view. The situation might look much more different, when air is replaced by pure oxygen as an oxidizer, since the final flue gas would consist only of water vapor under ideal conditions.

C.1.2.2   Oxidation of aluminium melt / dross formation

Although aluminium has a high potential for oxidation, in melting processes this is mitigated by the formation of a comparatively strong layer of aluminium oxide, which protects the melt from further oxidation. While other reactive metals require special measures (protective gases, vacuum furnaces) aluminium can be molten without protection in an industrial scale furnace. The costs for this simplicity of processing is some loss of the metal, which is transformed into oxide. The density of aluminium oxide (~4000kg/m3) is higher than the density of the melt (~2350 kg/s). Nevertheless, due to capillary effects and adherence of tiny gas bubbles the aluminium oxide skin floats on the top of the melt, as long it is thin. Under these conditions the oxide layer can be removed easily by mechanical skimming, which must be done regularly in a melting furnace, before the oxide layer gets too thick. A thick oxide layer will become brittle and opens fractures, which lead to further oxidation. This detrimental effect is increased by an excess of oxygen in the furnace atmosphere and high furnace and melt temperatures. A low amount of generated dross is an important criterion for the quality of the melting process. Besides the mentioned factors oxygen, temperature and time, the dross formation is also affected by the alloying composition and the shape of the charged material. Especially, magnesium embrittles the oxide layer and increases dross formation. This "breakaway oxidation" is well known (Cochran, C. N.; Belitskus, D. L.; Kinosz, D. L., 1977) and it has been demonstrated that some CO_2 in the atmosphere can reduce the tendency for oxidation. Recently it has been demonstrated that even in H_2 combustion an addition of CO_2 might have a beneficial effect on reduction of dross generation in melting of high magnesium aluminium alloys (Syvertsen, M.; Johannsson, A.; Lodin, J.; Bergin, A.; Ommedal, M.; Langsrud, Y.; Peterson, R. D., 2023)

On an industrial scale, it is hard to compare dross figures of different furnaces, since they depend very much on the installation, the charging material and the processing. In order to compare the impact of a fuel switch, the furnace setup and the processing should be kept as similar as possible.

C.2 Modifications of furnace system for hydrogen combustion with cold air

The first feasibility tests for hydrogen should be performed with minimized modifications of the existing furnace. Although a gradual transition from natural gas to hydrogen might appear logical the technical issues to mix the fuel gases and to control the fractions are not trivial and require expensive equipment. The easiest transition is a complete switch to 100 % hydrogen. This path was chosen in the tests described in this report. The connection to the supply grid for natural gas was replaced by a bottle stack for pressurized hydrogen. The station contains 8 bundles of 12 bottles à 50 l of hydrogen at 200 bar (per bundle approx. 107 Nm³ H₂). Two valves reduced the pressure to the operating pressure of about 50 mbar. The main changes concerned the cold air burner, which is an annular excess air burner of type Honeywell Kromschröder BIC 140R-450/485/47 with a nominal power rating of 350 kW. In this burner the head of type RB47 had to be exchanged to a head HD65 especially designed for hydrogen combustion (Figure 18). It differs by less inclined

HYINHEAT

blades at the tips of the swirl plate and some additional axial exit holes for the fuel. Thereby it generates less swirl and feeds the fuel faster into the furnace chamber in order to prevent a superheating of the burner head. The fuel air ratio of the burner is controlled by a balanced pressure regulator, which had to be adjusted once for the specifics of hydrogen as the new fuel. Since the bottle stack did not provide sufficient hydrogen for overnight operation, the fuel supply could be switched back to natural gas to keep the furnace on high temperature during the night. To compensate the mismatch of the balanced pressure regulator under these conditions (natural gas in place if hydrogen), additional air was fed into the secondary air supply of the annular excess air burner by manual changes in the furnace control system. Some hours before the tests the fuel supply was switched back to 100 % hydrogen.

The control system of the furnace regulates the power of the burner by thermocouples in the melt, the ceiling and the oxygen in the flue gas.
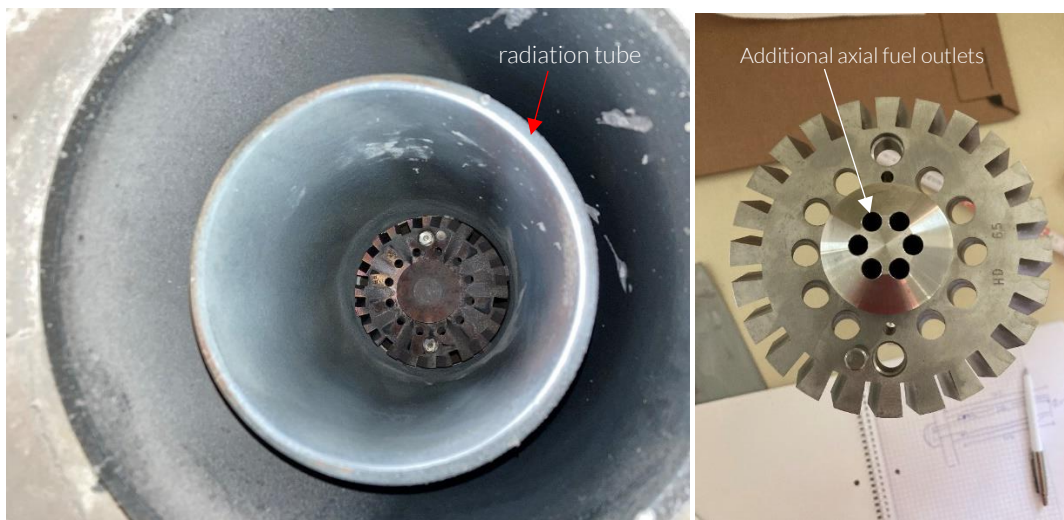
Figure 18: Modification of natural gas burner head RB47 (left) for combustion with hydrogen HD65 (right)

C.3 Test programme

The test comprises several tests to establish a baseline for comparison with natural gas – air combustion and later tests on oxy-hydrogen combustion:

1. Flame appearance
2. Heat transfer conditions
3. Dross formation and specific energy consumption
4. Hydrogen pickup in the melt
5. NOₓ emissions in offgas

C.3.1 Flame appearance / UV light exposition

At the beginning of the trials it was expected that the hydrogen flame would appear less visible than a natural gas flame due to lack of soot particles in the combustion gas. Actually this was not the case, and the hydrogen flame revealed a strong orange colour, see Figure 19. Discussions with the partner RWTH-GHI led to the conclusion that the colour is due to a reaction of the hot water vapor with the silicon carbide radiation tube, which encloses the burner head made of steel. For refractory suppliers it is a well-known corrosion mechanism that water vapor attacks silicon carbide. This could lead to the release of carbon traces causing the orange colour of the flame. Another aspect in the tests was the potentially increased emission of ultraviolet light (UV-B and UV-A, 290-390nm) as a new health risk for the operators. Measurements with a commercial sensor at the open furnace door gave no indication that the burner flame generates higher UV emissions and remained significantly below levels observed in sunlight.

HYINHEAT

Figure 19: Flame appearance hydrogen-air (left) versus natural gas-air (right)

C.3.2 Heat transfer conditions and specific energy consumption

To compare the heat transfer conditions in the furnace a cylindrical block of M=7.5kg of solid aluminium with a surface area A was heated with a specified burner power. The temperatures T_{in} inside the block and the ambient temperature T_{ext} of the furnace atmosphere in a close distance from the block were measured to calculate an effective heat transfer coefficient h at the surface of the block according to the formula:

$$\frac{M \cdot c_p}{A} \frac{(T_{in} - T_{in}^0)}{(T_{ext} - T_{in})(t - t^0)} = h$$

(c_p: specific heat of aluminium, t^0, T_{in}^0 :initial time and temperature of block)

Strictly speaking this formula is only correct for convective heat transfer and neglects that a considerable fraction of heat is transferred by radiation. But it provides a simple qualitative measure for the heat transfer depending on for the two different fuels.

The measurements were performed with the modified burner system for hydrogen and air (H2) and for natural gas and air using additional secondary air (NG2) to compensate the mismatch of the pressure regulator as mentioned earlier. These values were compared to measurements carried out with the old natural gas-air burner system before the modification (NG1). The results are shown in Figure 20. The values of the hydrogen combustion lie between the two series of natural gas combustion. According to this test hydrogen behaves very similar to natural gas in its heating characteristics.

HYINHEAT
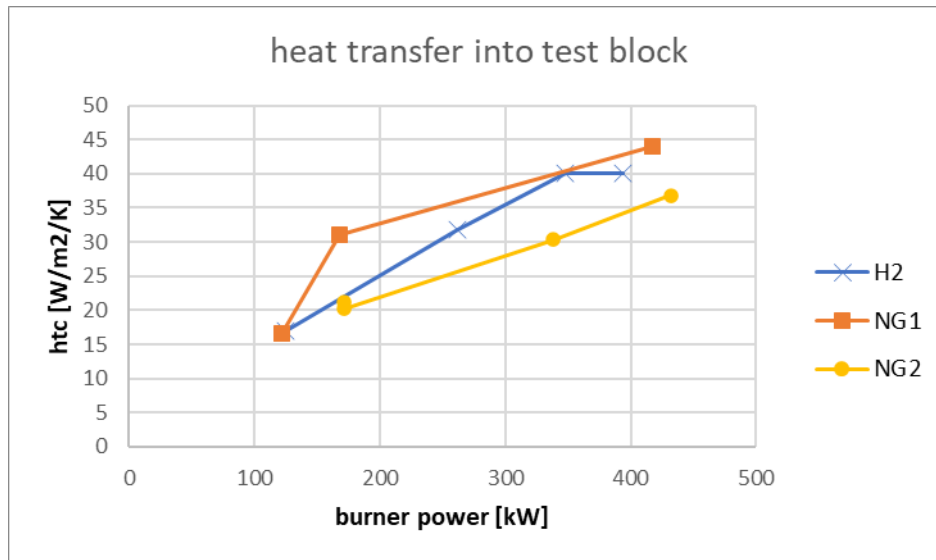
Figure 20: effective heat transfer coefficient in combustion of natural gas – air (NG1, NG2) and hydrogen – air (H2)

C.3.3 Dross generation and specific energy consumption

Four different types of input material were chosen to determine values of dross for comparison with earlier tests on natural gas combustion (see Figure 21: Baled foil scrap (left) and can body stock (cbs) stampings (middle) and trimmings of can lid stock (right). Figure 21:)

1. Al99.8 ingots
2. Can body stock (CBS) stamping scrap (alloy type 3xxx)
3. AlMg5 edge trimmings (alloy type 5xxx)
4. Foil edge trimmings (alloy type 8xxxx)

These charge materials were provided as production scrap with low contamination by lubricants from the milling process (< 0.1% typically). The furnace was operated in single chamber mode. In each charge about 400 – 500 kg of scrap were put into the main chamber (Figure 22). At the end of the melting cycle the dross was skimmed from the melt surface and weighed and the ratio with the input mass calculated. Figure 23 shows a comparison of the measured dross values with historical values from natural gas trials. The utilized energy is compared in a similar way with the long-term average for natural gas (Figure 24). Dross values as well as energy consumption do not differ significantly from typical values for natural gas combustion. It has to be kept in mind that the small furnace anyway has a higher specific energy consumption in comparison to a large industrial size furnace due to its larger surface to volume ratio, which increases the losses.

Figure 21: Baled foil scrap (left) and can body stock (cbs) stampings (middle) and trimmings of can lid stock (right).

HYINHEAT

Figure 22: Scrap charged into melting furnace for dross test.
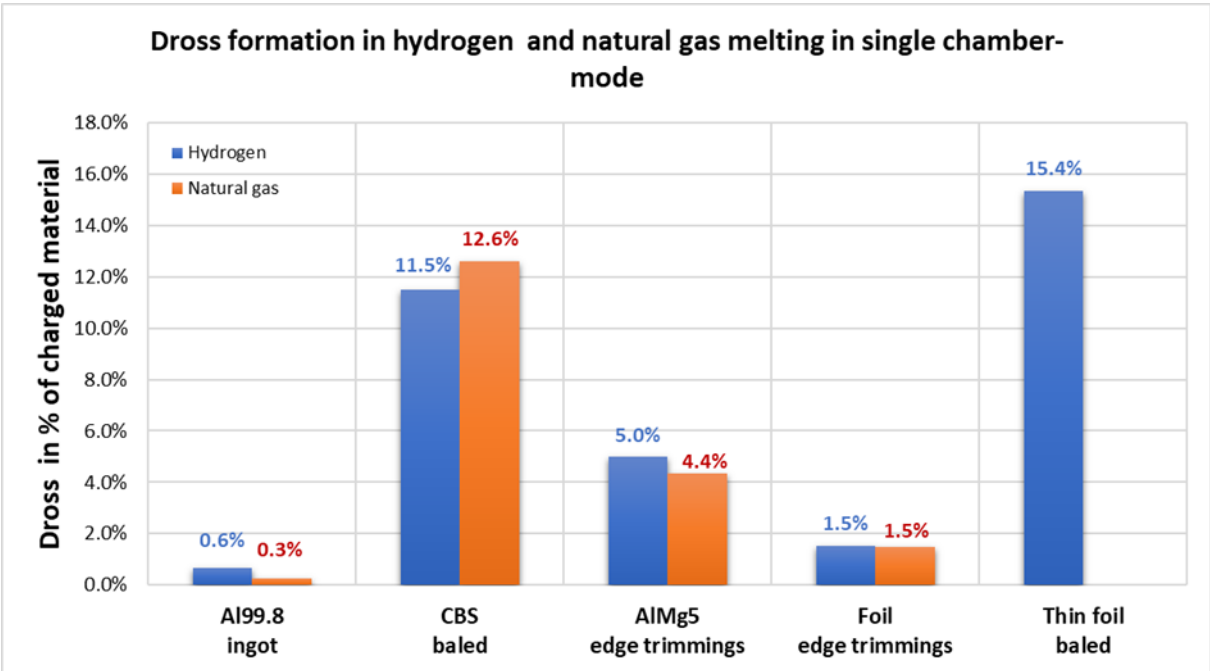
Figure 23: Relative dross figures for hydrogen (H2) combustion in comparison with historical values for natural gas heating (NG)

HYINHEAT
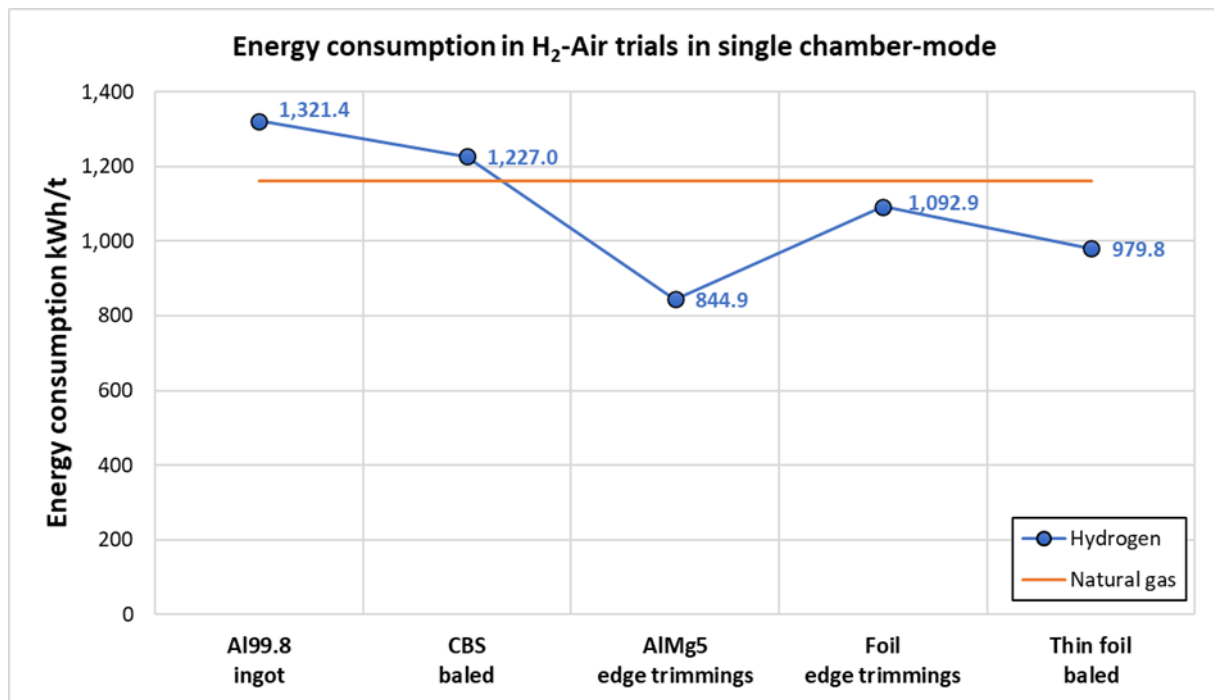
Figure 24: Specific energy consumption of hydrogen for different types of input material. The orange line is the reference determined as the average of previous melting trials of ingots of Al 99.8 with natural gas.

C.3.4 Measurements of hydrogen pickup in melt

In order to compare the hydrogen pickup in the melt, the furnace was operated in a 3-chamber mode: the external furnace chamber was separated by a barrier into two connected compartments, one containing a mechanical melt circulation pump to establish a closed loop of continuous melt flow, the other containing an AlSCAN probe (AlSCAN, 2024) to measure the hydrogen content of the melt. The contact with the burner flue gas in the main chamber is considered as the source for hydrogen pickup of the melt. Since alloying elements have a certain impact on the solubility of hydrogen tests were carried out for two alloys of type Al99.8 and AlMg5. As mentioned earlier, according to the higher fraction of water vapor in the flue gas, slightly higher values of hydrogen were expected in the tests with hydrogen. Actually, the tests did not show an increase compared to combustion of natural gas, but appeared even lower in some cases, which might be due to the typical scatter in this type of measurements (Figure 25, Figure 26).

HYINHEAT
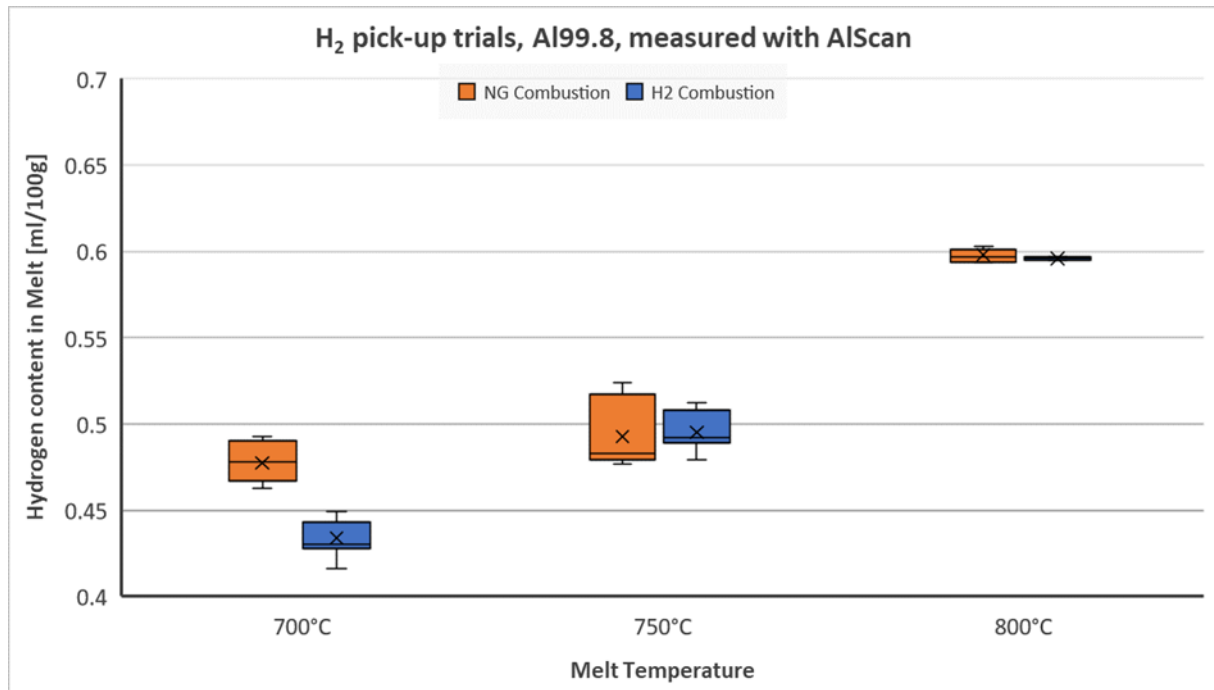
Figure 25: Hydrogen pickup in Al99.8 at different temperatures for natural gas and hydrogen combustion
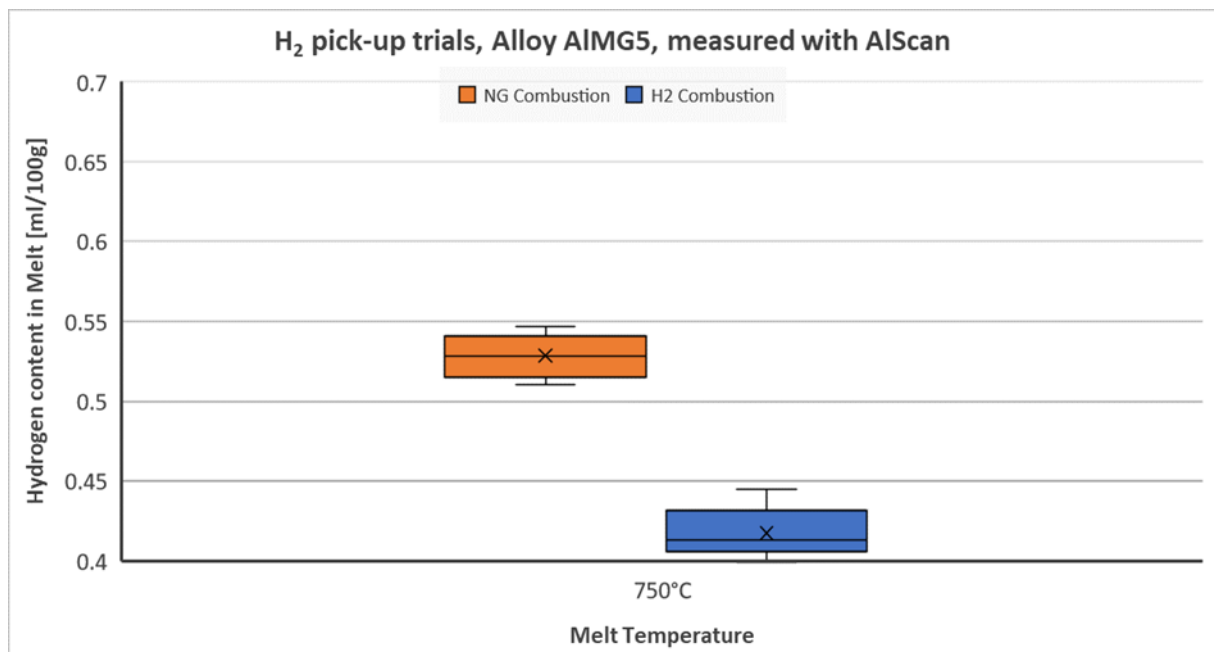
Figure 26: Hydrogen pickup in high magnesium alloy AlMg5 at 750° for natural gas and hydrogen

C.3.5 NOx measurements

NO$_x$ emissions were measured during melting of foil production scrap (alloy type 8xxx) using a chemiluminescence detection system (Eco Physics, CLD 700). The system records the NO and NO$_2$ content in the dried flue gas (Figure 27). The recalculation of the maximum detector value of 182 ppm for the sum of NO and NO$_2$ yields an amount of 373 mg NO$_2$/Nm^3 in the offgas, which is about twice as high as the value of natural gas combustion under similar conditions.

HYINHEAT
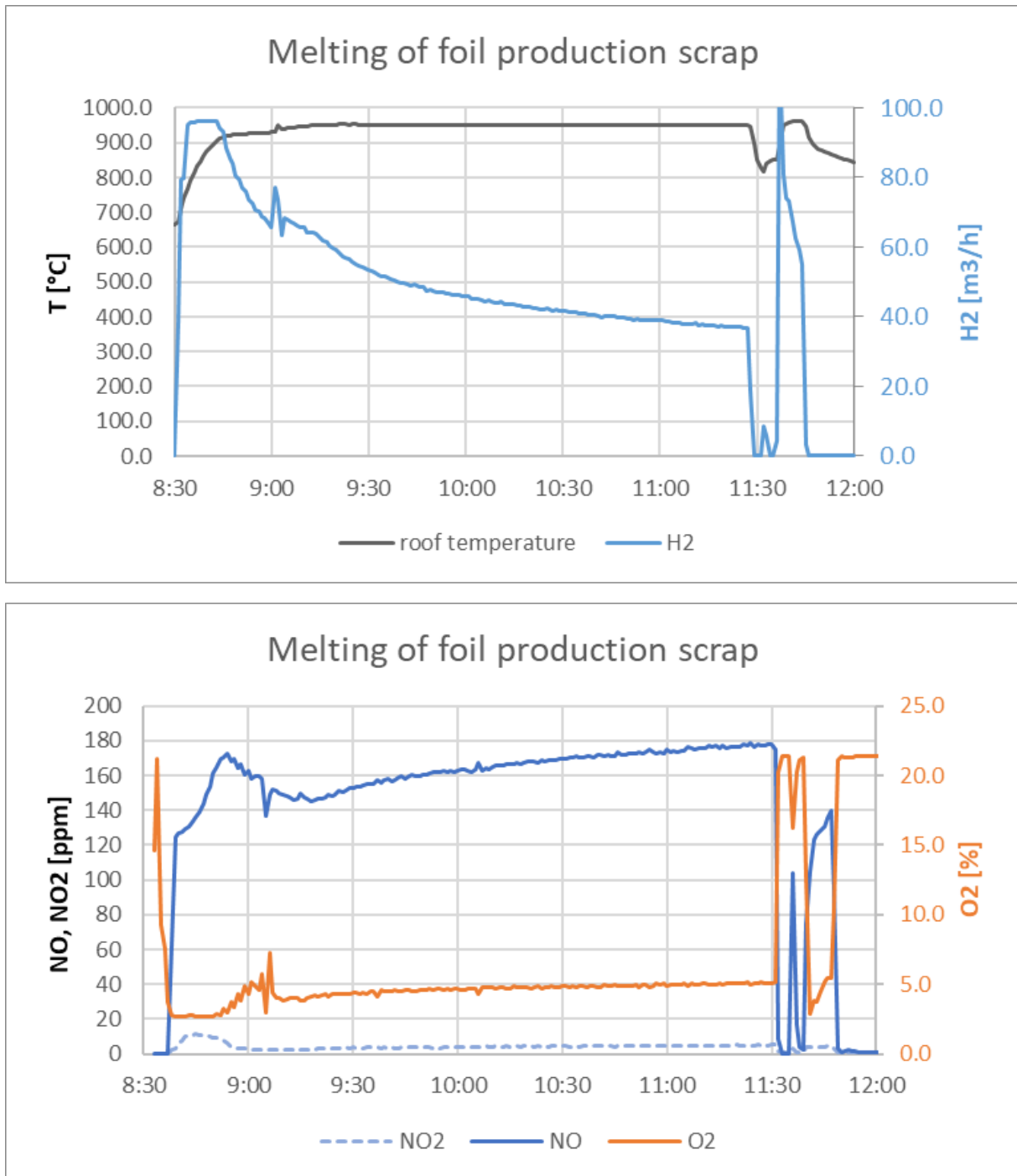
Figure 27: NOx measurements during melting of foil production scrap.

C.4 Summary

Speira R&D carried out melting tests with hydrogen as a substitute fuel for natural gas on a 1.5t lab scale aluminium melting furnace equipped with a cold air burner system to investigate the impact of the fuel switch on the melt quality, especially dross formation and hydrogen pickup and energy efficiency. Only minor changes on the burner system had to be carried out. The changes in the operation appeared rather unspectacular. An expected increased hydrogen content in the melt could not be verified and even dross values do not differ significantly from values for natural gas combustion. Provided a sufficient supply of competitive green hydrogen a decarbonization of existing melting furnaces appears to be feasible with moderate modifications of equipment and without a loss of product quality.

HYINHEAT

D. Impact of H$_2$ reheating cycles on STEELS

D.1 Introduction

The main objective of the work carried out is to support the development of H$_2$ reheating processes in different critical routes. In particular, the presented work focuses on the evaluation of the quality of steel resulting from the implementation of H$_2$ combustion during the reheating stage previous to hot rolling. Steel quality data provide mandatory input for the implementation of the demonstrators and the retrofit/greenfield studies in WP5/6/7.

To this end, lab-scale tests have been carried out on steel products including heat treatments (HT), thermogravimetric analysis (TGA) and thermomechanical tests. Material selection include materials supplied by consortium partner AMOB and a selection of materials carried out at CEIT based on steel product geometry and %C. All materials have been carefully characterised (which include macroscopic measurements as well as microstructural characterisation) after thermal exposure. Industrial heating profiles under defined furnace atmospheres (NG/Air (baseline), H$_2$/Air, NG/O$_2$ and H$_2$/O$_2$) have been applied with the aim of identifying the impact of the new atmospheres on steel quality.

D.2 Materials and experimental procedures

D.2.1 Steel selection

Investigations related to steel reheating processes have been carried out by CEIT. The studies have been carried out on materials of industrial origin, which include materials supplied by consortium partner AMOB and on a selection of materials carried out at CEIT based on geometry and %C. The material selection is as follows:

- AMOB:
    - S235JR Beam Blank
    - S355JR Beam Blank

- CEIT selection:
    - Thin slab: 0.05-0.07%C – Microalloyed (Ti, TiNb,...)
    - Slab: S355: 0.15-0.17%C – Microalloyed Nb-Ti
    - Billets:
        - 0.19%C rebar
        - 0.4%C-0.2%Si
        - 0.8% pearlitic
        - 1%C

D.2.2 Atmospheres

The atmospheres used in the different tests are those derived from the combustion of NG and H$_2$ with air and O$_2$, being NG/Air considered as the reference one. In order to obtain the proportions of the gases resulting from combustion, the stoichiometric ratios of the corresponding reactions have been used assuming standard conditions. In the case of combustion with air, a small excess of the oxidant was included in order to reproduce the industrial conditions. In the case of oxy-combustion, both the theoretical stoichiometric case and the operational case, in which a small excess of oxidant is expected, have been studied. The resulting atmospheres are presented in Table 10.

Table 10. Composition of the combustion atmospheres employed.

Impact of H_2 heating on product quality, yield, and refractory

Combustion atmosphere	CO_2 (% vol.)	O_2 (% vol.)	N_2 (% vol.)	H_2O (% vol.)
NG/Air (λ=1.21)	8.0	3.4	72.6	16.0
H_2/Air (λ=1.21)		3.1	67.3	29.6
NG/O_2 (λ=1)	33.0			67.0
NG/O_2* (λ=1.03)	32.7	2.0		65.3
H_2/O_2 (λ=1)				100.0
H_2/O_2* (λ=1.04)		2.0		98.0

The ID for each atmosphere has been given by its volume percentage of water vapour, being 16%, 30%, 67%, 65%, 100% and 98%, respectively.

D.2.3 Heat Treatments (HT)

In order to evaluate the response to high temperature oxidation of the set of materials under study, HT have been performed in the laboratory. For the simulation of different combustion atmospheres, a set-up has been designed, whose configuration is shown in Figure 28, and consists of:

- Coriolis effect mass flowmeter for the control of distilled H_2O
- CEM (Controlled Evaporator and Mixer) system, by which the defined amount of liquid (H_2O) is vaporized and mixed with the carrier gas
- Temperature controller and power supply
- Mass Flow Controllers (MFCs) with different output pressures and calibrated for different gases. The different MFCs allow the generation of different types of mixtures containing different gases (CO_2, O_2, N_2, Ar, ect.).
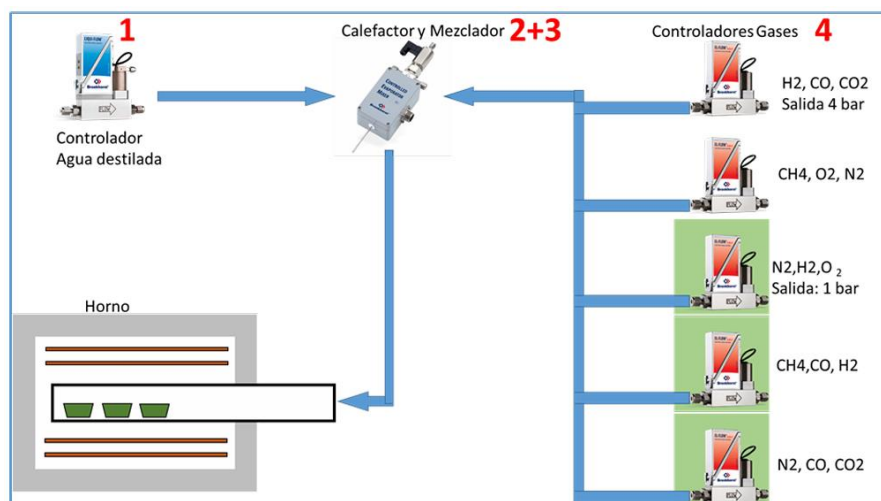
Figure 28. Design of the set-up for the simulation of combustion atmospheres in the laboratory.

The system requires a minimum carrier gas flow rate for proper operation, which means the addition of a minimum carrier gas flow rate in the 100% and 98% H_2O atmospheres.

HYINHEAT

Impact of H₂ heating on product quality, yield, and refractory

Tests have been carried out in an MTS Model 653.04B high-temperature furnace. It consists of a cavity with a quartz tube, into which the samples are introduced. Temperature control is carried out by means of three thermocouples placed in different positions along the tube, which allows a homogeneous heating zone to be achieved. In addition, an external thermocouple is inserted into the tube during the test to record the effective thermal cycle.

The applied thermal cycle consists of a slow heating, until 1250 °C is reached. The samples are then held for 15 minutes at this temperature. Both, heating and isothermal holding correspond to the industrial ramp according to the data provided by the steelmaker, and oxidising atmospheres (Section D.2.2) are applied during these steps. Finally, after the 15 minutes of holding time, the samples are cooled down inside the furnace applying an inert atmosphere (Ar).

Heat treatments have been carried out for all the materials and atmospheres selected. The specimens used were parallelepipeds with dimensions of about 20 mm*10 mm* 4 mm.

All samples tested have been investigated after thermal exposure. The characterisation work carried out includes:

- Macroscopic measurements, which include mass variation measurements, and measurements of mass loss and thickness of oxide layers formed.
- Microstructural characterisation by OM and FEG-SEM, studying the following aspects:
    - On the oxidised surfaces:
        - Study of the morphology of the oxidised layer.
        - Compositional analysis of the external oxide layer using the technique of energy dispersive X-ray spectrometry (EDS).
    - On transversal section:
        - Aspect of the oxide and the interface with reference to the degree of oxide adhesion. The characterisation has been carried out over large areas of the samples.
        - EDS compositional analyses have allowed: chemical mappings in section covering the different oxidised/interface/matrix layers and, point analysis in regions of interest including oxidised layers, internal oxidation and matrix.
        - Electron backscatter diffraction (EBSD) analyses have allowed the identification of the main constituent phases of the oxide and the characterisation of the crystallographic relationships along the layers.

D.2.4 Thermogravimetric analysis (TGA)

All thermogravimetric oxidation experiments have been carried out on a NETZSCH model STA 449 F3 Jupiter® with the TGA (thermogravimetric analysis) sensor. The unit has been equipped with a water vapour furnace capable of operating in a wide temperature range (from room temperature (RT) up to 1250 °C), applying complex atmospheres that can reach 100% water vapour. The materials tested include both steel grades from AMOB as well as a part of the CEIT material selection. Materials tested and test conditions are summarised below:

- Materials:
    - AMOB S235JR
    - AMOB S355JR
    - Slab S355
    - 0.19%C Rebar
    - 0.4%C+0.2%Si
    - Pearlitic
- Atmospheres:
    - NG/Air → 16 %H_2O + 8 %CO_2 + 3 %O_2 + 73 %N_2
    - H2/Air → 30 %H_2O + 3 %O_2 + 67 %N_2

HYINHEAT

- o   GN/O2 ➔ 67 %H2O + 33 %CO2
- o   H2/O2 ➔ 100 %H2O
- o   GN/O2* ➔ 65 %H2O + 33 %CO2 + 2 %O2
- o   H2/O2* ➔ 98 %H2O + 2 %O2
- Thermal cycle:
  - o   Heating: RT up to 1250 °C at ~20°C/min in Ar atmosphere
  - o   Isothermal: 15 min isothermal holding at 1250°C in oxidising atmosphere
  - o   Cooling: from 1250 °C to RT in Ar atmosphere

Samples were parallelepipeds with dimensions of about 10 mm*10 mm* 2 mm. Both the mass and the initial dimensions of the samples have been measured initially in order to express the normalised mass increase per unit area (W). Values for constant kinetics have been determined via thermogravimetric methods, by fitting changes in mass due to the reaction of the base material with oxidised atmospheres which are recorded.

The progression of mass increase per unit area, W, can be described in a simplified way by the linear and parabolic rate laws (Equation 1and Equation 2).

$$W = k_l \cdot t$$

Equation 1

$$W^2 = k_p \cdot t$$

Equation 2

The linear rate law is usually observed under conditions where a phase-boundary process is the rate-determining step for the reaction, and typically, the rate limiting process is assumed to be related to the reactions occurring at the scale-gas interface. As the reaction proceeds at a constant rate the scale layer thickens, at the same time the flux of ions through the scale must be equivalent to the surface reaction rate. To maintain this constant flux, the activity of the metal at the scale–gas interface must fall as the scale thickens, eventually approaching the value in equilibrium with the atmosphere. Since the metal activity cannot fall below this value, further increase in scale thickness must result in a reduction in the metal activity gradient across the scale and, consequently, to a reduction in ionic flux and the reaction rate. At this point the transport of ions across the scale becomes the rate-controlling process and the rate falls with time according to a parabolic rate law (N. Birks, 2006).

D.2.5   Material embrittlement assessment

In order to evaluate embrittlement and ductility loss, hot torsion tests have been implemented. The set-up for simulating combustion atmospheres in the laboratory described in Section D.2.3 was used, as well as an induction system for applying the thermal cycle. After applying the thermal cycle in the corresponding atmosphere, test to fracture or two-pass tests, simulating the first stages of hot rolling, have been carried out. Figure 29 shows the configuration used in hot torsion tests.

HYINHEAT

Impact of H₂ heating on product quality, yield, and refractory
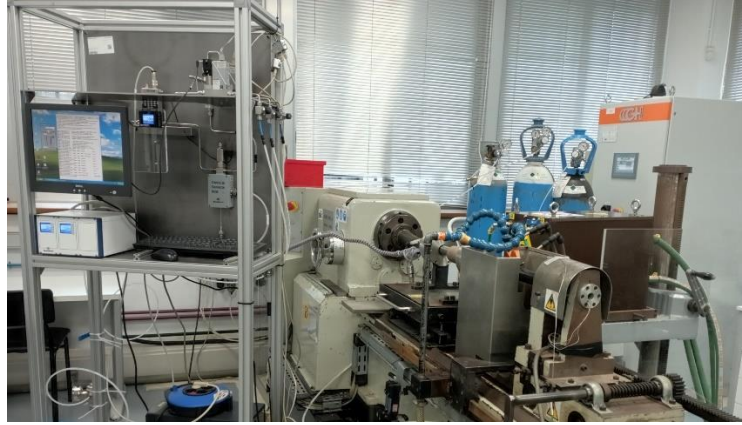
Figure 29. Set-up for the torsion tests.

The materials tested include both steel grades from AMOB and part of the CEIT material selection. The thermal cycle and conditions applied prior to the torsion tests are the same as those used in the heat treatments. Materials tested and test conditions are summarised below:

- Materials:
    - AMOB S235JR
    - AMOB S355JR
    - Thin Slab
    - 1%C Billet
- Atmospheres:
    - NG/Air → 16 %H_2O + 8 %CO_2 + 3 %O_2 + 73 %N_2
    - H₂/Air → 30 %H_2O + 3 %O_2 + 67 %N_2
    - NG/O_2 → 67 %H_2O + 33 %CO_2
    - H₂/O_2 → 100 %H_2O
    - NG/O_2* → 65 %H_2O + 33 %CO_2 + 2 %O_2
    - H₂/O_2* → 98 %H_2O + 2 %O_2
- Thermal cycle:
    - Heating: RT up to 1250 °C in oxidising atmosphere
    - Isothermal: 15 min isothermal holding at 1250°C in oxidising atmosphere
    - Cooling: from test temperature to RT in Ar atmosphere
- Mechanical conditions
    - AMOB S235JR and AMOB S355JR: ε'=3 s⁻¹; test to fracture and two-pass tests, with deformation per pass ε=0.2 at T_1 and T_2 (according to initial industrial rolling pass temperatures) and with 20 s of time between passes.
    - Thin Slab and 1%C Billet: ε'=3 s⁻¹; tests to fracture.

Embrittlement and hot ductility loss have been evaluated by measuring the strain to fracture from hot torsion tests in the different NG/H₂ combustion atmospheres and referred to results in an inert atmosphere (Ar). From the data of the stress-strain curves of the tests to fracture, 2 cracking susceptibility parameters have been defined:

$$E_p(\%) = \frac{\sigma_{Ar} - \sigma}{\sigma_{Ar}} \cdot 100 \qquad \text{Equation 3}$$

$$E_e(\%) = \frac{\varepsilon_{Ar} - \varepsilon}{\varepsilon_{Ar}} \cdot 100 \qquad \text{Equation 4}$$

where σ_{Ar} and σ correspond to maximum stress in Ar and in all other atmospheres, and ε_{Ar} and ε correspond to strain to fracture in Ar and in all other atmospheres, respectively.

HYINHEAT

In addition, two-pass torsion tests simulating first rolling passes after reheating have been carried out in order to compare results of maximum load and elongation on the stress-strain curves obtained for different atmospheres and steel grades.

For the evaluation of surface quality, measurements have been carried out based on quantitative metallography techniques. The analysis of images obtained from the thermomechanically tested specimens sectioned and metallographically prepared have been carried out to obtain:

- Distribution of number of cracks per unit length analysed.
- Cracking susceptibility parameters, defined as a function of the number and length of cracks developed on the surface:

$$\frac{n_{cracks}}{L} = \frac{n_1 + n_2 + n_3 + n_4}{L} \qquad \text{Equation 5}$$

$$\frac{l_{cracks}}{L} = \frac{n_1 \cdot 12.5 + n_2 \cdot 37.5 + n_3 \cdot 100 + n_4 \cdot 225}{L} \qquad \text{Equation 6}$$

where L is the total length analysed, n_1 is the number of cracks with length less than 25 µm, n_2 is the number of cracks between 25-50 µm, n_3 is the number of cracks between 50-150 µm and n_4 is the number of cracks with length greater than 150 µm. These ranges are adaptable to new results. A low value of the parameters n_{cracks}/L and l_{cracks}/L indicates a low susceptibility to cracking, while a high value indicates a high incidence of cracking.

D.3 Results and discussion

D.3.1 Heat treatments (HT)

In order to evaluate the effect of H_2 combustion during reheating on steel, HT have been carried out in the laboratory with the aim of simulating industrial reheating process, as detailed in Section D.2.3.

After HT, various quantitative measurements have been carried out in order to study the effect of the different atmospheres on oxidation. Table 11 shows the results obtained, which include mass change, material loss and external and internal oxide thickness. In general terms, the mass change of the samples indicates that the mass gain achieved is higher for oxy-combustion atmospheres (67%, 65%, 100% and 98% H_2O) than for air combustion atmospheres (16% and 30% H_2O). Particularly high values are obtained for the NG/O_2 case (67% and 65% H_2O), especially when there is 2% free O_2 in the atmosphere (65% H_2O). It should be noted that in this case the remaining gas corresponds to CO_2, whereas in H_2/O_2 atmospheres (100% and 98% H_2O), 18% vol. of the gas actually corresponds to Ar. In any case, the presence of 2% free O_2 seems to produce an increase in mass gain.

Material loss and oxide thickness measurements show, in general terms, similar trends to those found in the mass change measurements, although these measurements have a higher variability, especially oxide thickness measurements.

Table 11. Quantitative measurements after oxidation tests, including mass change, material loss and external and internal oxide thickness.

Steel ID	Atmosphere (%H_2O)	Total mass change (mg/cm²)	Material loss (mm)	Oxide thickness (µm)	
				External	Internal
AMOB S235JR	16%	56.0	0.28	757	59
	30%	71.4	0.45	842	41
	67%	73.4	0.43	773	36
	65%	140.9	0.80	2096	78
	100%	90.5	0.53	1009	33

HYINHEAT

Impact of H_2 heating on product quality, yield, and refractory

	98%	77.3	0.53	948	44
AMOB S355JR	16%	60.0	0.31	794	34
	30%	80.5	0.41	1148	32
	67%	79.3	0.38	913	25
	65%	153.0	0.85	1973	28
	100%	96.0	0.44	1108	25
	98%	94.2	0.58	936	21
Thin Slab	16%	52.9	0.30	720	22
	30%	71.2	0.41	791	17
	67%	97.0	0.46	1053	21
	65%	64.0	0.54	917	17
	100%	91.1	0.61	948	23
	98%	83.2	0.63	875	17
Slab S355	16%	56.7	0.31	834	49
	30%	50.2	0.38	639	29
	67%	90.4	0.51	1025	27
	65%	91.7	0.52	1020	34
	100%	89.9	0.48	956	23
	98%	85.1	0.60	947	24
0.19%C Rebar	16%	58.7	0.37	779	49
	30%	58.6	0.39	797	29
	67%	92.8	0.61	1240	28
	65%	96.9	0.53	1228	26
	100%	95.1	0.52	1123	18
	98%	85.5	0.56	1133	16
0.4%C+0.2%Si	16%	60.4	0.41	962	36
	30%	69.5	0.46	1081	25
	67%	99.2	0.54	1136	22
	65%	100.3	0.46	1178	23
	100%	91.9	0.47	993	17
	98%	90.4	0.52	1027	22
Pearlitic	16%	48.6	0.33	747	38
	30%	78.6	0.43	1252	25
	67%	86.7	0.49	1013	24
	65%	127.9	0.61	1634	84
	100%	81.2	0.39	880	24
	98%	61.3	0.34	617	17
1%C Billet	16%	74.6	0.41	1318	38
	30%	65.7	0.42	972	31
	67%	85.9	0.61	959	27
	65%	126.7	0.62	1745	58
	100%	59.8	0.38	1138	36
	98%	64.5	0.43	744	24

All samples tested have been investigated after thermal exposure. The characterisation work carried out has led to the development of a characterisation methodology starting with the analysis of oxidised surfaces. Both, macro and FEG-SEM images provide interesting information, as they show that, in general terms, oxidised surfaces can present 2 different characteristic aspects. In some cases, the oxide is characterised by very coarse crystallographic units, while in other cases it is characterised by the development of a finer microstructure. The results suggest that obtaining one type of surface or the other depends mainly on the atmosphere applied. In general, coarser grain sizes are associated with higher H_2O contents. Figure 30 shows, as an example, the images obtained by FEG-SEM in the surface characterisation for 0.4%C+0.2%Si material.

In order to carry out a more detailed characterisation of the oxide, the samples were cut, mounted and prepared in section following the metallographic route of grinding and liquid polishing with various water-based diamond suspensions. In addition, the samples were polished with a colloidal silica solution to facilitate phase revelation and electron backscattered diffraction (EBSD) measurements.

HYINHEAT
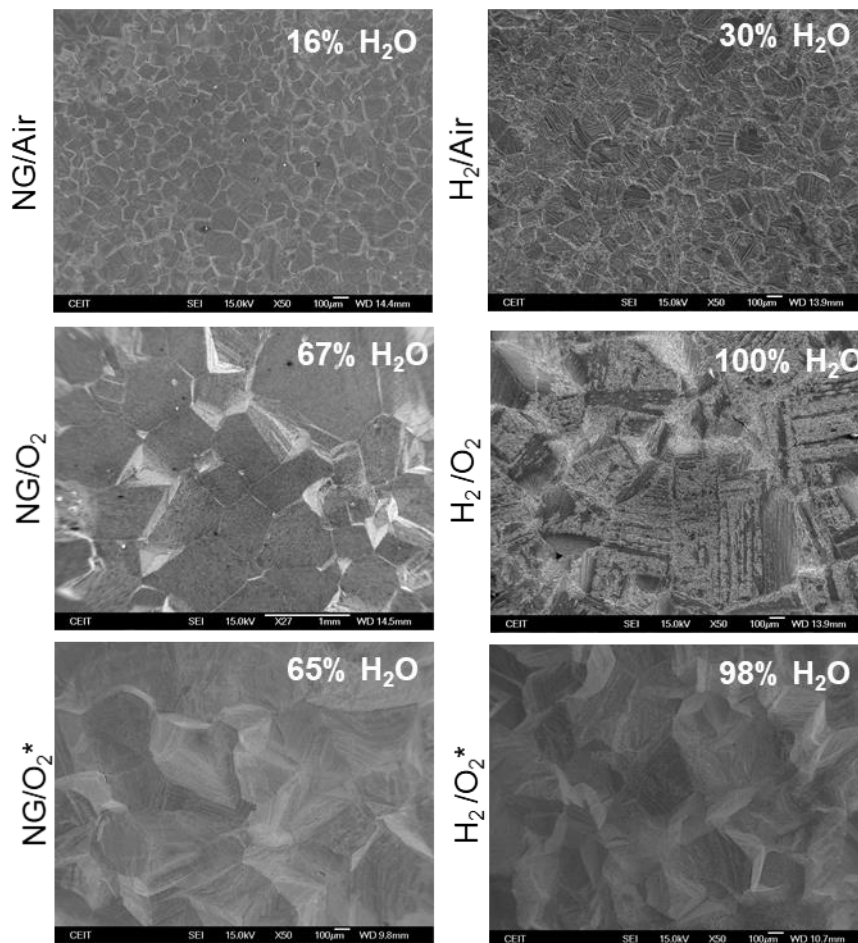
Figure 30. FEG-SEM images of the surface of the oxides generated by applying different atmospheres during HT. Material: 0.4%C+0.2%Si.

Figure 31 shows the type of images obtained from the oxide layer section. The contrast in the FEG-SEM images obtained using backscattered electrons allows the matrix (lighter contrast) to be clearly distinguished from the generated scale. Within the oxide, the images show different contrasts associated with the presence of different phases along with a characteristic pore distribution. Even in these general images it is possible to see significant differences in the development of the layers depending on the material and atmosphere applied. Systematic work has been carried out to identify several regions of interest, which have been studied in greater detail. These are: the outer region and the inner region of the oxide scale, and the interface between the oxide and the matrix. The main results obtained are presented below.

HYINHEAT
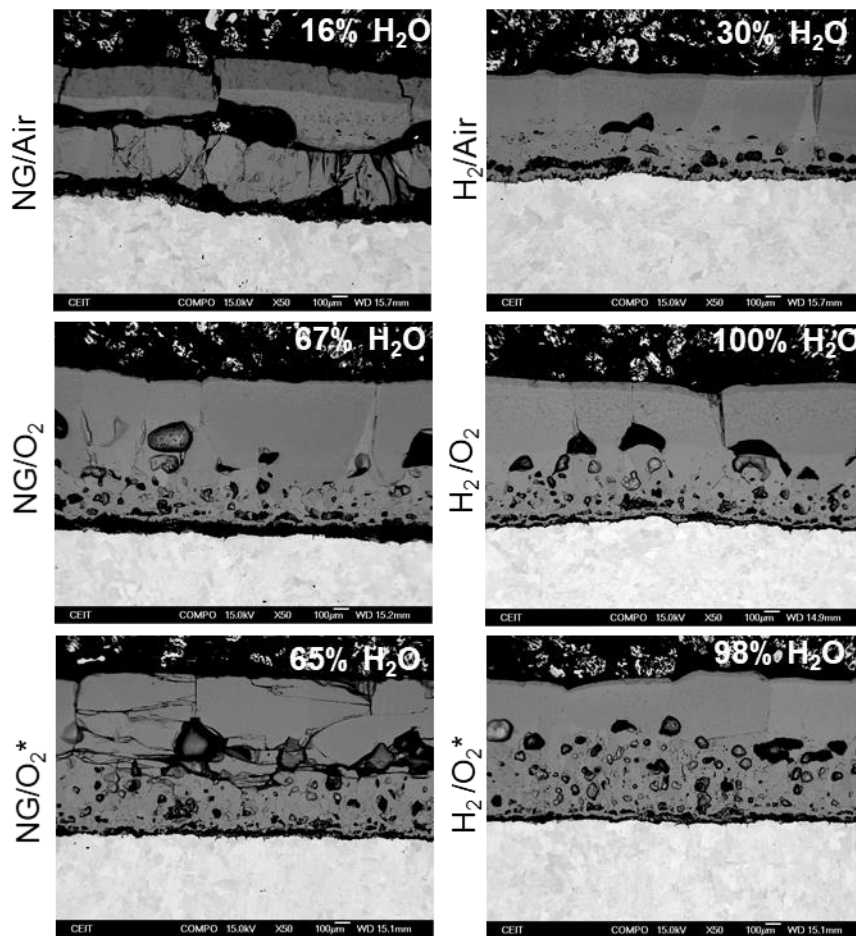
Figure 31. FEG-SEM images of the sections of the oxides generated by applying different atmospheres during HT. Material: Slab S355.

OUTER REGION

The work carried out has shown that the outer region of the oxide layer is of great interest, as it shows significant differences related to the oxidation mechanism developed in each case. Figure 32 shows the type of images obtained in this region, in this case for the Rebar 0.19%C material. This type of study, carried out on all the materials, has shown that the outer region is characterised by the presence of an external layer, which has been identified by EBSD as magnetite. However, this layer can present 2 different morphologies and characteristics, that appear depending on the atmosphere and the material under study. Thus, in some cases, the magnetite layer is thick and has a smooth morphology (16% H_2O case in Figure 32), while in others, the layer is thinner (or even has discontinuities) and has a characteristic island-like morphology (30%, 67%, 65%, 100% and 98% H_2O cases in Figure 32). For all the steels analysed, it has been possible to correlate the appearance of one or other morphology with the macro and surface examination.

HYINHEAT
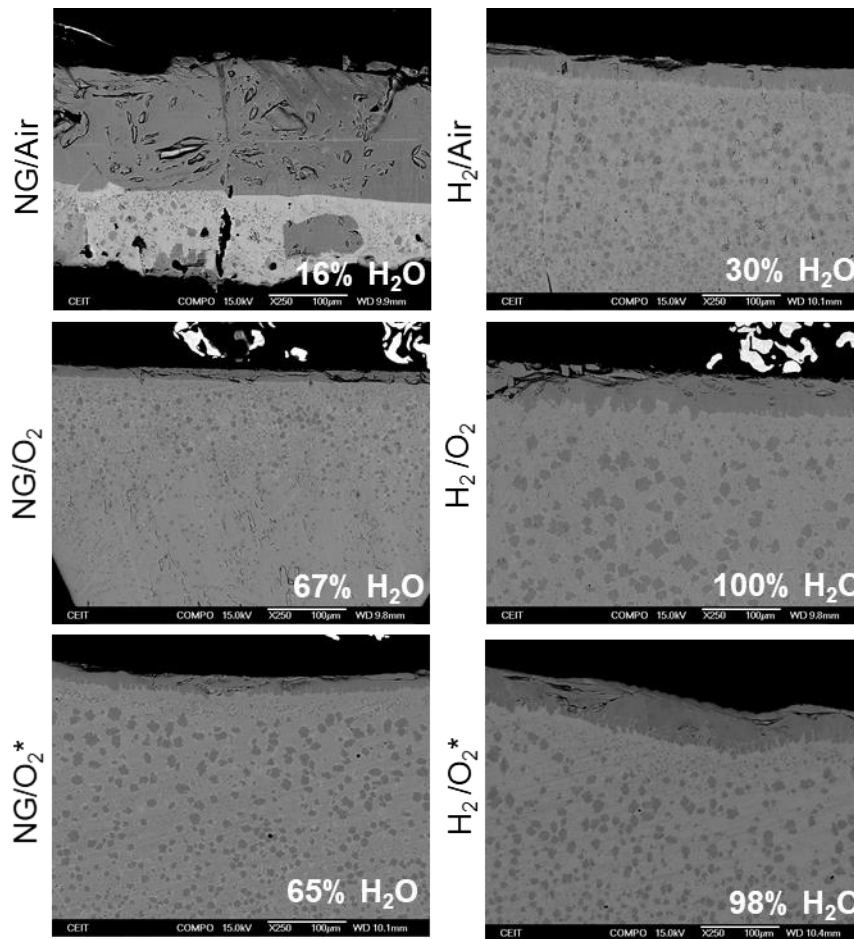
Figure 32. FEG-SEM images of the outer region of the oxides generated by applying different atmospheres during HT. Material: Rebar 0.19%C.

In addition, a phase with acicular morphology and clear contrast has been observed in the outermost region of the magnetite layer, as shown in the optical microscopy (OM) images in Figure 33. This phase has been identified as haematite. The amount of haematite found is very low in all cases, and its presence varies in the section, although in general terms there is a higher fraction in the samples where the magnetite layer is thicker and has a smooth morphology.
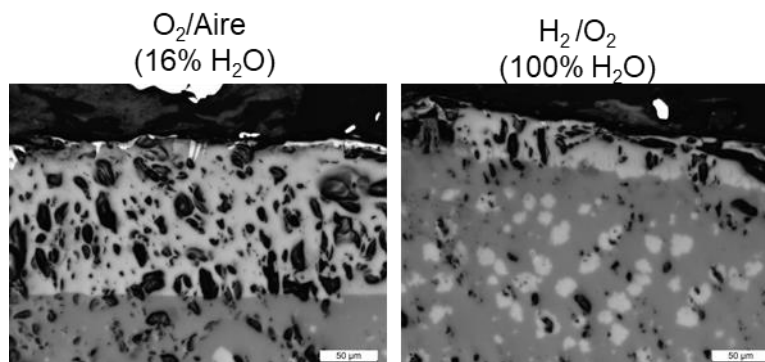
Figure 33. OM images of the outer region of the oxides generated by applying different atmospheres during HT. Material: Billet 1%C.

HYINHEAT

The characterisation of this region has been completed using EBSD measurements, as shown in the examples in Figure 34. Quality images, phase maps and orientation maps are used to illustrate the results obtained. The phase maps allow the identification of haematite, magnetite and wustite according to the associated colour code. The orientation maps (IPF) show the orientation of the different crystallographic units that form the oxide layers. EBSD measurements have shown that in those cases where the outer magnetite layer is thicker and has a smooth morphology, the layer is composed of different crystallographic units (see phase maps and orientation maps together). However, where the magnetite layer is thinner (or has discontinuities) and has an island-like morphology, EBSD studies have shown that in these cases the magnetite has the same orientation as the wustite grains on which it grows. Also noteworthy in the orientation and phase maps is the presence of magnetite within the wustite grains in all cases. This magnetite also has an island-like morphology and has the same orientation as the wustite grains on which it grows. Wustite is not stable below 570 °C and tends to transform. The growth of magnetite with the same orientation seems to indicate that its formation does not take place at high temperature, but during the cooling stage.

Given the significant differences found, it has been concluded that 2 different oxidation mechanisms can be activated in the materials, depending on the atmosphere and material tested. The Type I mechanism is characterised by the presence of a thick, smooth layer of magnetite formed by independent crystallographic units, whereas in the Type II mechanism, the oxide is characterised by being mainly composed of very large grains of wustite. On these grains, in many cases, a thin layer of magnetite with an island-like morphology, formed during cooling, can be observed.
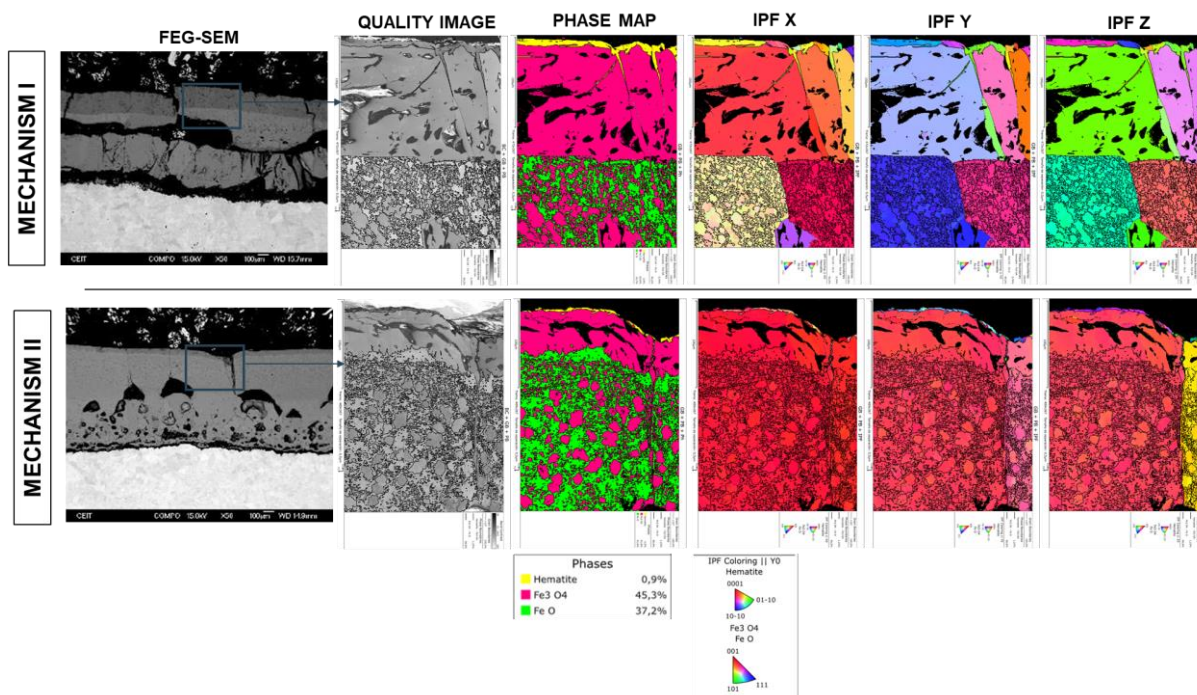
Figure 34. EBSD images (Quality Image, Phase Map and Orientation Maps (IPF)) illustrative of the Type I and Type II oxidation mechanism. Material: Slab S355 (16% H$_2$O (Type I) and 100% H$_2$O (Type II)).

This analysis was extended to all the samples tested. It was observed that, in general terms, the application of the 16% H$_2$O atmosphere activated the Type I oxidation mechanism in all cases, while the 67%, 65%, 100% and 98% H$_2$O atmospheres activated the Type II mechanism. However, the application of the 30% H$_2$O atmosphere was able to activate one or the other mechanism depending on the material. Table 12 summarises the results obtained in the characterisation.

HYINHEAT

Table 12. Summary of the results obtained from the characterisation of the outer region.

Steel ID	Atmosphere (%H$_2$O)	Surface grain size	Mechanism
AMOB S235JR	16%	Fine	Type I
	30%	Coarse	Type II
	67%	Coarse	Type II
	65%	Coarse	Type II
	100%	Coarse	Type II
	98%	Coarse	Type II
AMOB S355JR	16%	Fine	Type I
	30%	Fine	Type I
	67%	Coarse	Type II
	65%	Coarse	Type II
	100%	Coarse	Type II
	98%	Coarse	Type II
Thin Slab	16%	Fine	Type I
	30%	Coarse	Type II
	67%	Coarse	Type II
	65%	Coarse	Type II
	100%	Coarse	Type II
	98%	Coarse	Type II
Slab S355	16%	Fine	Type I
	30%	Coarse	Type II
	67%	Coarse	Type II
	65%	Coarse	Type II
	100%	Coarse	Type II
	98%	Coarse	Type II
0.19%C Rebar	16%	Fine	Type I
	30%	Coarse	Type II
	67%	Coarse	Type II
	65%	Coarse	Type II
	100%	Coarse	Type II
	98%	Coarse	Type II
0.4%C+0.2%Si	16%	Fine	Type I
	30%	Fine	Type I
	67%	Coarse	Type II
	65%	Coarse	Type II
	100%	Coarse	Type II
	98%	Coarse	Type II
Pearlitic	16%	Fine	Type I
	30%	Fine	Type I
	67%	Coarse	Type II
	65%	Coarse	Type II
	100%	Coarse	Type II
	98%	Coarse	Type II
1%C Billet	16%	Fine	Type I
	30%	Fine	Type I
	67%	Coarse	Type II
	65%	Coarse	Type II
	100%	Coarse	Type II
	98%	Coarse	Type II

INNER REGION

The characterisation of the oxide layer has been extended to the inner region. For the set of materials analysed, this region is mainly composed of wustite, which has a significantly smaller grain size than that observed in the outer region, as can be seen in the examples presented in Figure 35. In addition, the inner region of the samples is also characterised by the occurrence of a dark contrasting intergranular phase, which has been identified as (Fe,Si)O. Also typical is the presence of pores that tend to decrease in size as the

HYINHEAT

distance to the interface decreases. These features have been found in all the materials, and are independent of the applied atmosphere.
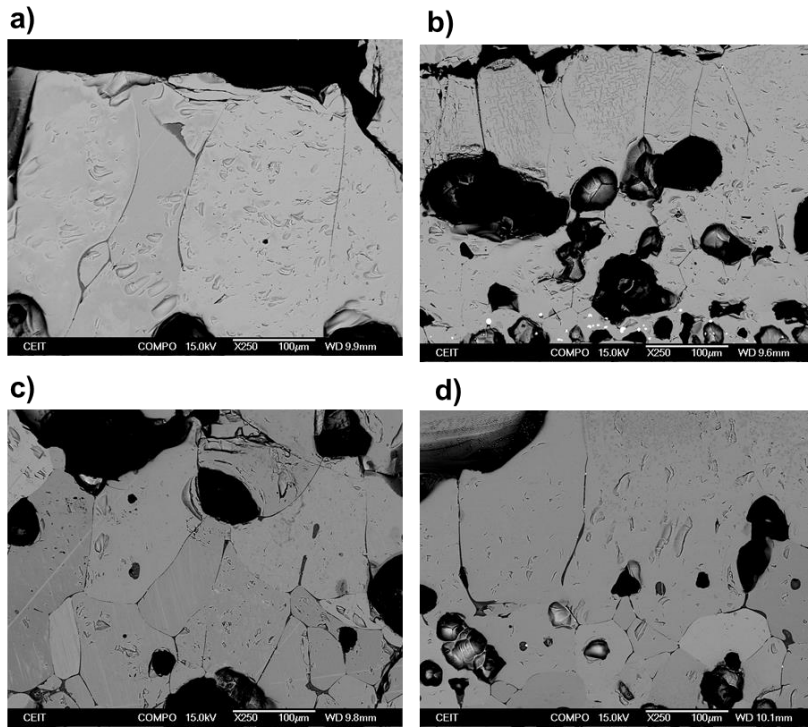
Figure 35. FEG-SEM images of the inner region of the oxides generated by applying different atmospheres during HT. Materials a) Pearlitic – 16% H_2O, b) AMOB S355JR – 30% H_2O, c) Rebar 0.19%C – 67% H_2O and d) Thin Slab – 98% H_2O.

INTERFACE

The study of the samples has been completed by characterising the interface between the oxide and the matrix. This region is of particular interest as it is expected to have a direct impact on the descaling properties (Richard Osei, 2022) and on the possible embrittlement phenomena that can be activated during the following processing stages (Gadadhar SAHOO, 2016).

Characterisation has shown that the morphology, the presence of phases and their characteristics are particularly dependent on the composition of the steel grade (while, in general, there is no obvious effect of the atmosphere). In addition, a high fraction of small oxides in the near-oxide matrix, known as internal oxidation, is typically observed in this region. The composition of the internal oxidation also depends on the composition of the steel grade. Examples of the interface and internal oxidation are shown in Figure 36.

HYINHEAT
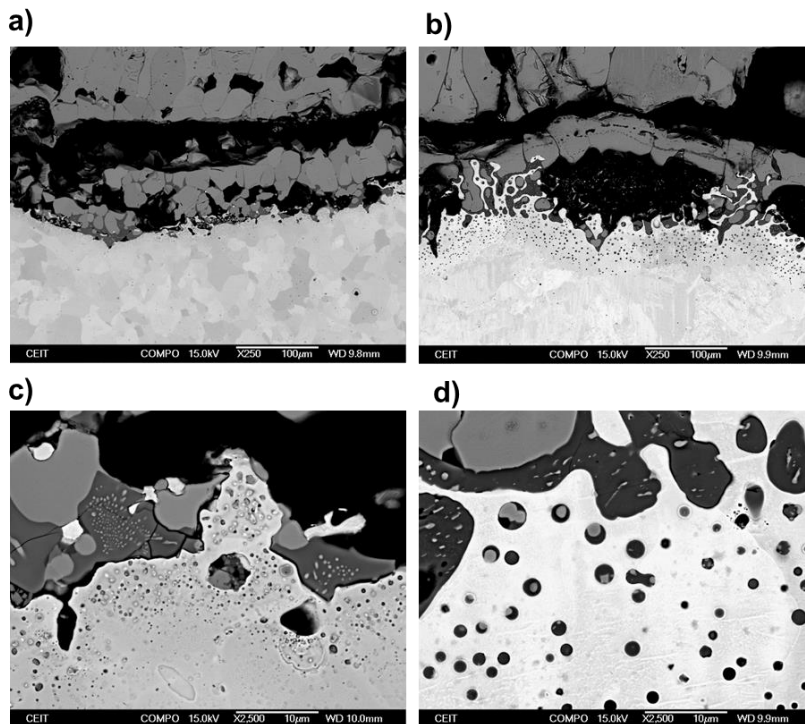
Figure 36. FEG-SEM images of the interface and detail of the internal oxidation. Materials: a) and c) Thin Slab (16% H₂O), b) and d) 0.19%C Rebar (16% H₂O).

A detailed analysis by FEG-SEM and EDS has been carried out in order to identify and describe the interface of all materials. In general terms, the results obtained are independent of the applied atmosphere. The phases typically identified are FeO, (Fe,Si)O and occluded matrix, which tend to be enriched in some elements more noble than Fe. Their presence, fraction, morphology and distribution depend on the steel grade studied, as does the presence of other minority phases. The composition of the internal oxidation also depends on the steel grade. A summary of the results obtained is given in Table 13.

Table 13. Summary of oxide-matrix interface and internal oxidation characterisation for the set of materials tested.

Steel ID	Interface and internal oxidation characteristics
AMOB S235JR	FeO || Intergranular (Fe,Si)O || Enriched occluded matrix (Cu, Ni) || Globular (Fe,Si)O || Slight enrichment in Cu || Int. Ox → (Fe,Cr,Mn,Si)O
AMOB S355JR	FeO || Intergranular (Fe,Si)O || Enriched occluded matrix (Cu, Ni) || Globular (Fe,Si)O || Slight enrichment in Cu || Int. Ox → (Fe,Cr,Mn,Si,Ti)O
Thin Slab	FeO || Intergranular (Fe,Si)O || Enriched occluded matrix (Cu) || Globular (Fe,Si)O || Slight enrichment in Cu || Int. Ox → (Fe,Cr,Mn,Si,Ti,Al,V)O

HYINHEAT

Slab S355	FeO || Intergranular (Fe,Si)O || Globular (Fe,Si)O || Int. Ox → (Fe,Mn,Si,Al)O
0.19%C Rebar	FeO || Intergranular (Fe,Si)O || Globular (Fe,Si)O || Slight enrichment in Cu || Int. Ox → (Fe,Mn,Si,V)O
0.4%C+0.2%Si	FeO || Intergranular (Fe,Si)O || Enriched occluded matrix (Cu, Ni) || Globular (Fe,Si)O || Slight enrichment in Cu || Int. Ox → (Fe,Cr,Mn,Si,V)O
Pearlitic	FeO || Intergranular (Fe,Si)O || Globular (Fe,Si)O || Int. Ox → (Fe,Cr,Mn,Si)O
1%C Billet	FeO || Intergranular (Fe,Si)O || Enriched occluded matrix (Cu,Ni) || Globular (Fe,Si)O || Slight enrichment in Cu || Int. Ox → (Fe,Cr,Mn,Si)O

In general terms, the results obtained are independent of the applied atmosphere. Only for specific steel grades, when a 65% H$_2$O atmosphere was applied, significant changes in the interface have been observed. In particular, this phenomenon has been observed for the materials AMOB S235JR, AMOB S355JR and 1%C Billet (see the example in Figure 37). In these cases, although the type of phases present does not vary, a significant change in morphology is observed as a result of an increase in the occluded matrix, forming a structure of interconnected phases which seems to increase the adhesion of the oxides in the area. It is worth noting that the measurements of total mass change / material loss / oxide thickness for these materials when applying the 65% H$_2$O atmosphere show a very significant increase compared to the 67% H$_2$O atmosphere (and the other atmospheres).
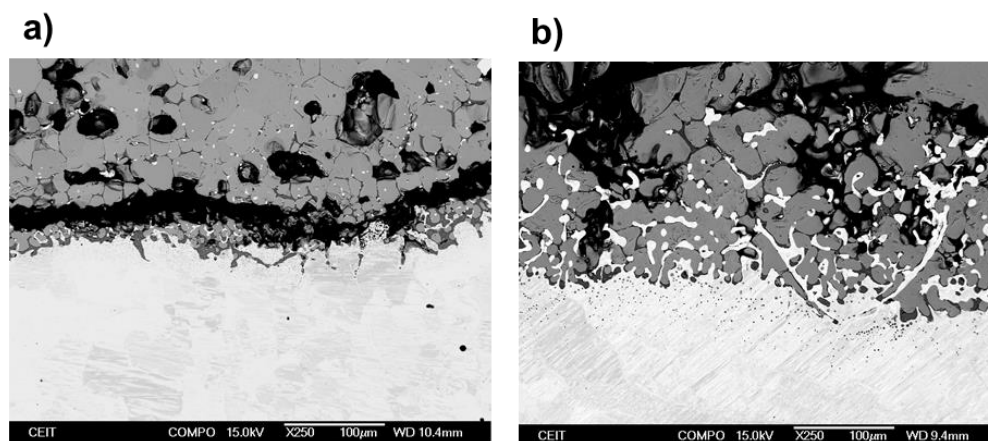
Figure 37. FEG-SEM images of the interface. Material AMOB S235JR, a) 67% H$_2$O and b) 65% H$_2$O.

D.3.2 Thermogravimetric analysis (TGA)

HYINHEAT

Impact of H$_2$ heating on product quality, yield, and refractory

Thermogravimetric tests have been carried out in order to study in detail the isothermal oxidation kinetics of some of the materials under investigation, as described in Section D.2.4.

Figure 38 shows the mass gain (W) obtained in the measurements for the materials a) AMOB S235JR, b) AMOB S355JR, c) Slab S355, d) Rebar 0.19%C, e) 0.4%C+0.2%Si and f) Pearlitic. The applied atmospheres correspond to 16%, 30%, 67% and 100% H$_2$O. The figures show that similar trends are obtained for the set of materials, so that it is observed that the 67% and 100% H$_2$O atmospheres (with higher H$_2$O contents) produce a higher oxidation, while the 16% and 30% H$_2$O atmospheres cause a lower mass gain. It can also be seen that the curves obtained for the 67% and 100% H$_2$O atmospheres are mainly parabolic, while the curves obtained in the 16% and 30% H$_2$O atmospheres show longer linear beginnings with later transitions to the parabolic regime. Linear kinetics typically occurs when the oxide thickness is thin and the limiting reaction is the transfer of oxidising species from the gas phase to the metal oxide phase, whereas the parabolic kinetics occurs when the limiting reaction is due to limited diffusion of ions in the oxide layer.

HYINHEAT
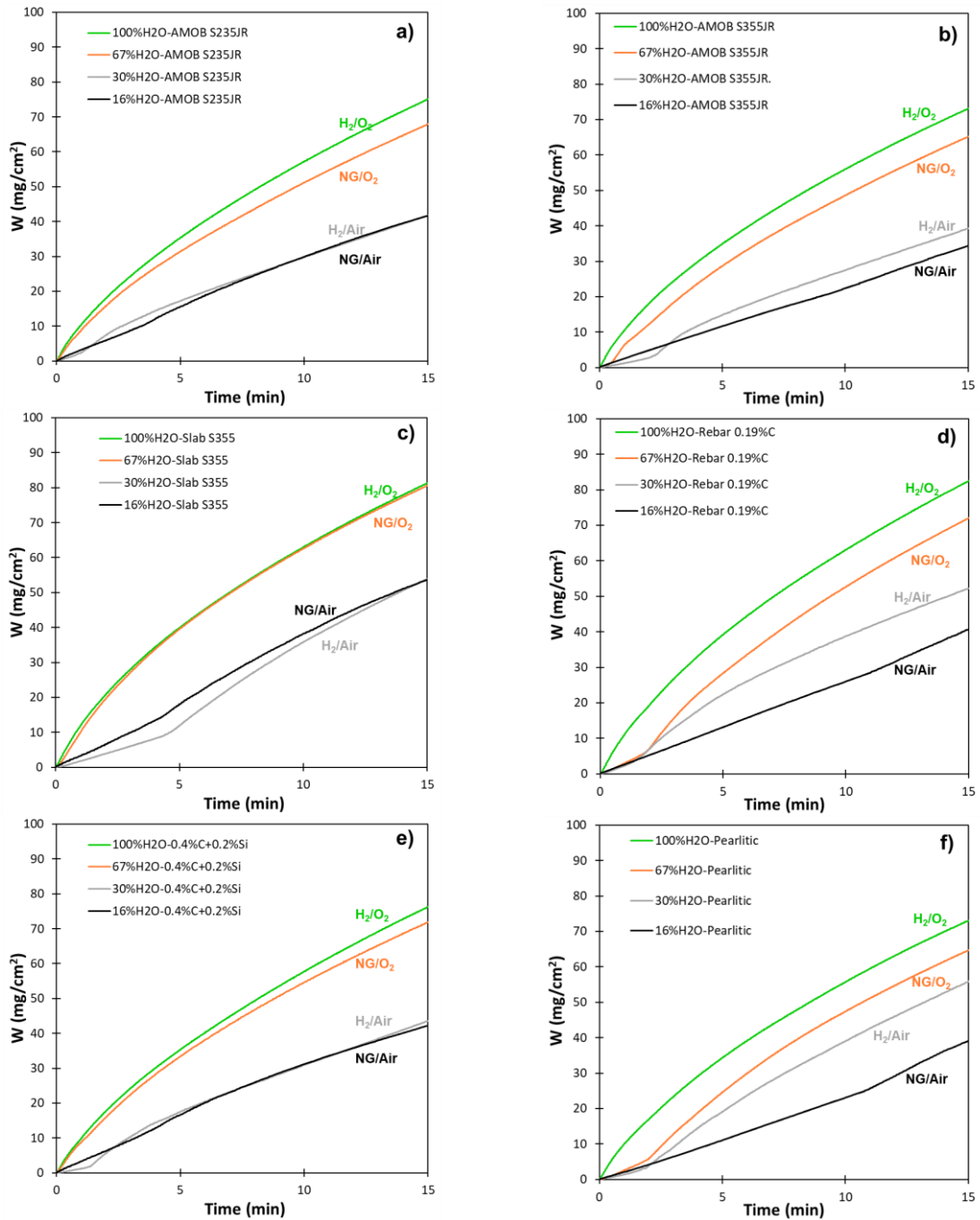
Figure 38. Comparison of the mass gain (W) when applying the atmospheres 16%, 30%, 67% and 100% for materials a) AMOB S235JR, b) AMOB S355JR, c) Slab S355, d) Rebar 0.19%C, e) 0.4%C+0.2%Si and f) Pearlitic.

After the tests, the samples were visually inspected. Figure 40 shows, as an example, the images obtained after the tests for the Rebar 0.19%C material. The visual inspection has shown that different surface appearances develop depending on the atmosphere applied and the material tested. Thus, it is possible to identify surfaces characterised by the presence of coarse grains, while other surfaces are characterised by the presence of finer crystallographic units. These results seem to indicate that, depending on the material and the atmosphere applied, different oxidation mechanisms may be activated, which could be in line with the results obtained in the HT (Section D.3.1).

HYINHEAT
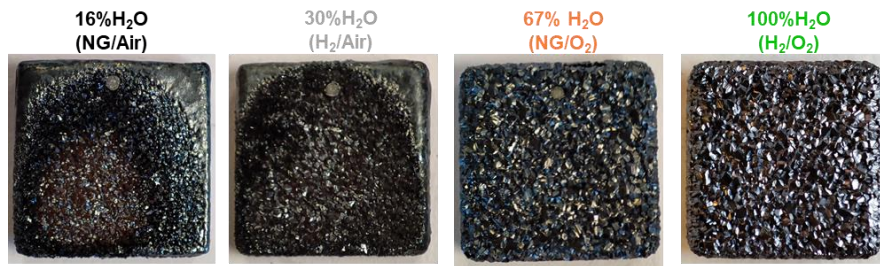
Figure 39. Macro images of the samples after thermogravimetric tests. Material: Rebar 0.19%C.

To evaluate the effect of free O_2 in oxy-combustion atmospheres, addition TGA tests were implemented using 65% and 98% H_2O atmospheres. Figure 40 shows the results obtained using these atmospheres together with those obtained using 67% and 100% H_2O atmospheres. The figures show that similar trends are obtained for the set of materials, and that the presence of 2% free O_2 in these atmospheres causes a slight increase in the kinetics.

HYINHEAT
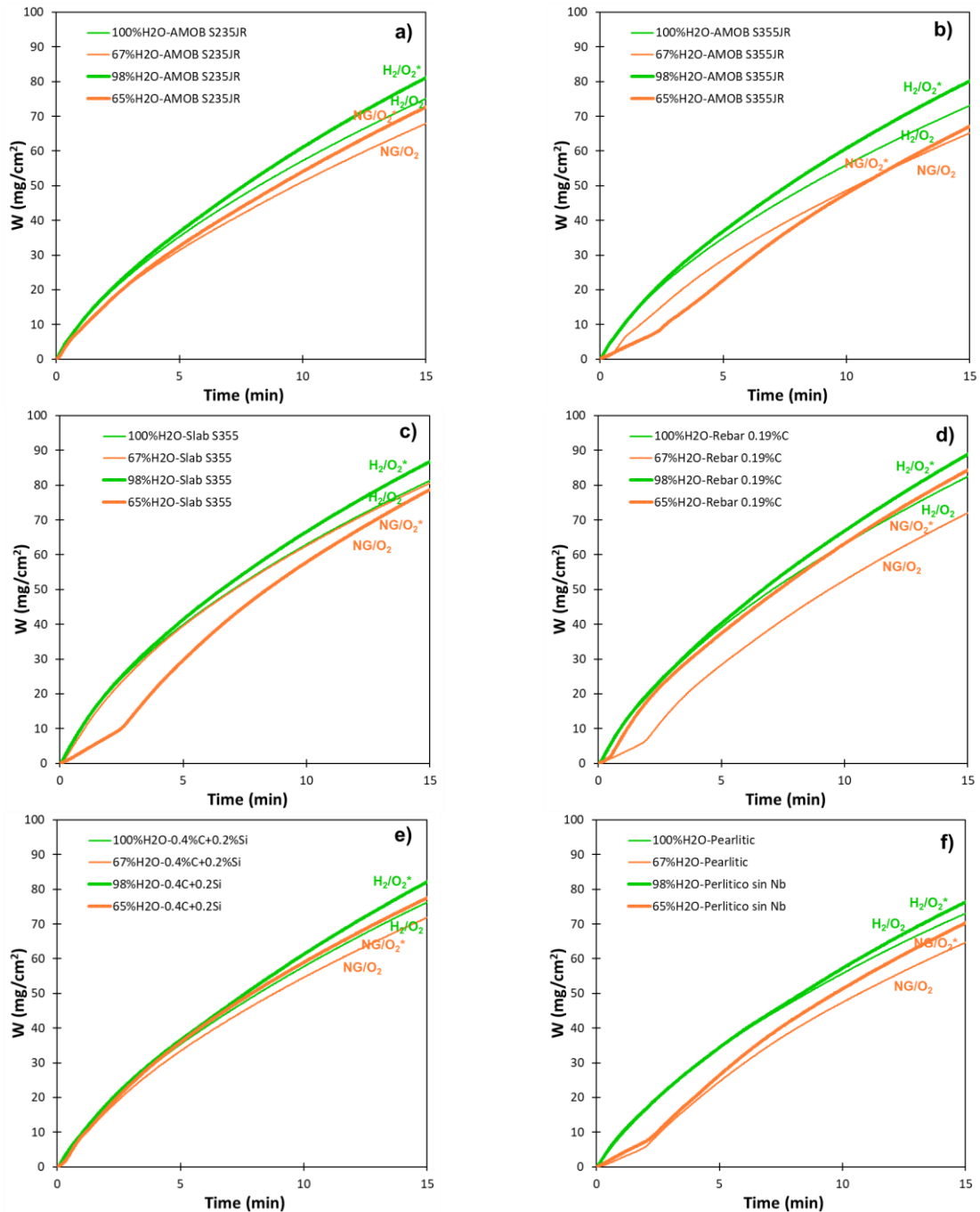
Figure 40. Comparison of the mass gain (W) when applying the atmospheres 67%, 65%, 100% and 98% H₂O for materials a) AMOB S235JR, b) AMOB S355JR, c) Slab S355, d) Rebar 0.19%C, e) 0.4%C+0.2%Si and f) Pearlitic.

Visual inspection after the tests has shown that the application of 65% and 98% H₂O atmospheres, as well as 67% and 100% H₂O atmospheres, produces the development of oxidised surfaces with coarse grain sizes. However, it is noteworthy that in the samples tested in the atmospheres with free O₂ the surfaces show a reddish tone, especially in the case of 98% H₂O. Figure 41 shows, as an example, the images obtained after the tests for the AMOB S355JR material.

HYINHEAT
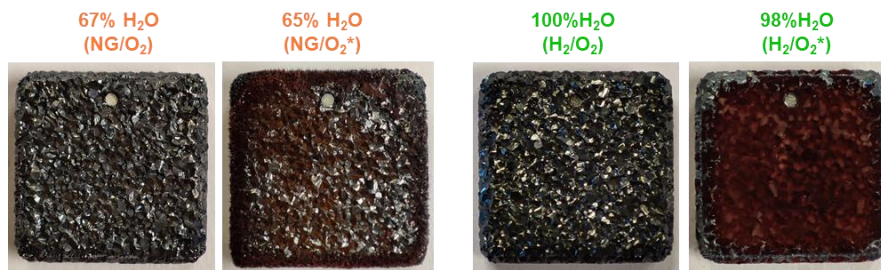
Figure 41. Macro images of the samples after thermogravimetric tests. Material: AMOB S355JR.

X-ray diffraction (XRD) measurements have been carried out in order to identify the red phase formed. Figure 42 shows a comparison of the results obtained for a sample without the presence of this phase (upper diffractogram) and for another sample with a reddish tone (lower diffractogram). The results seem to indicate that it is some kind of hydrated haematite.
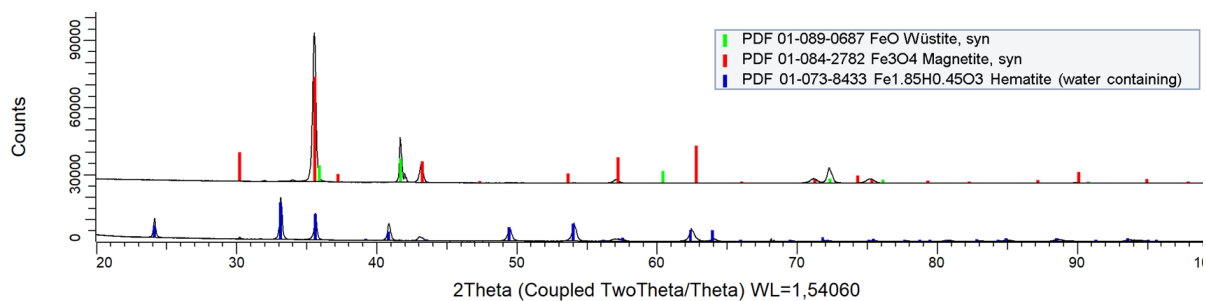
Figure 42. X-ray diffractograms obtained from the samples tested in TGA. Material: 0.4%C+0.2%Si (67%H₂O (upper) and 98% H₂O (lower)).

The mathematical description of the phase boundary controlled part is done by a linear function, whereas the diffusion controlled part is done by a parabolic function. The exact evaluation of k_l and k_p has been done by fitting the corresponding linear and parabolic parts of the curves according to Equation 1 and Equation 2. The values obtained for k_l and k_p are summarised in Table 14 and Figure 43. As can be seen, all the materials present linear starts for the 16% and 30% H_2O atmospheres, while for the 100% and 98% H_2O atmospheres all the materials present a completely parabolic behaviour. For the 67% and 65% H_2O atmospheres different behaviours are observed, depending on the material. The k_l values obtained show a low dispersion in the values, although slightly higher values are obtained for the atmospheres 65 and 67% H_2O when there is linear onset. On the other hand, k_p values obtained show that the kinetics are significantly lower when 16% and 30% H_2O atmospheres are applied. The values of the constants increase significantly with the 67% and 100% H_2O atmospheres. Slightly higher values are generally found when free O_2 is present in these atmospheres, as shown by the results obtained in the 65% and 98% H_2O cases. Finally, the visualisation of kinetic constants (Figure 43) shows that in general some of the materials are more susceptible to oxidation than others. It can be observed that k_p obtained are higher in all the atmospheres studied for the materials Thin Slab, Rebar 0.19%C and Slab S355.

HYINHEAT

Impact of H₂ heating on product quality, yield, and refractory

*Table 14. Values for k_l and k_p obtained for the different atmospheres applied and materials tested. (*Thin Slab and 1%C Billet data from a previous work).*

Steel ID	Atmosphere (%H$_2$O)	k_l (mg s^{-1}cm^{-2})	k_p (mg^{2}s^{-1}cm^{-4})
AMOB S235JR	16%	0.05	2.7
	30%	0.04	2.5
	67%	-	6.0
	65%	-	6.9
	100%	-	7.1
	98%	-	8.6
AMOB S355JR	16%	0.04	2.8
	30%	0.02	2.3
	67%	0.04	5.6
	65%	0.06	6.8
	100%	-	6.7
	98%	-	8.3
Slab S355	16%	0.05	4.5
	30%	0.03	5.2
	67%	-	8.2
	65%	0.07	8.9
	100%	-	8.2
	98%	-	9.5
0.19%C Rebar	16%	0.04	4.4
	30%	0.04	3.8
	67%	0.05	7.3
	65%	0.05	9.2
	100%	-	8.7
	98%	-	10.3
0.4%C+0.2%Si	16%	0.05	2.7
	30%	0.02	2.7
	67%	-	6.6
	65%	0.08	7.7
	100%	-	7.5
	98%	-	9.0
Pearlitic	16%	0.04	4.3
	30%	0.03	4.7
	67%	0.05	5.9
	65%	0.06	7.1
	100%	-	6.8
	98%	-	7.5
Thin Slab*	16%	0.05	5.4
	30%	0.04	6.1
	67%	0.09	8.8
	65%	0.08	9.8
	100%	-	9.4
	98%	-	10.2
1%C Billet*	16%	0.04	4.1
	30%	0.03	2.9
	67%	0.05	6.2
	65%	0.06	7.0
	100%	-	7.9
	98%	-	7.9

HYINHEAT
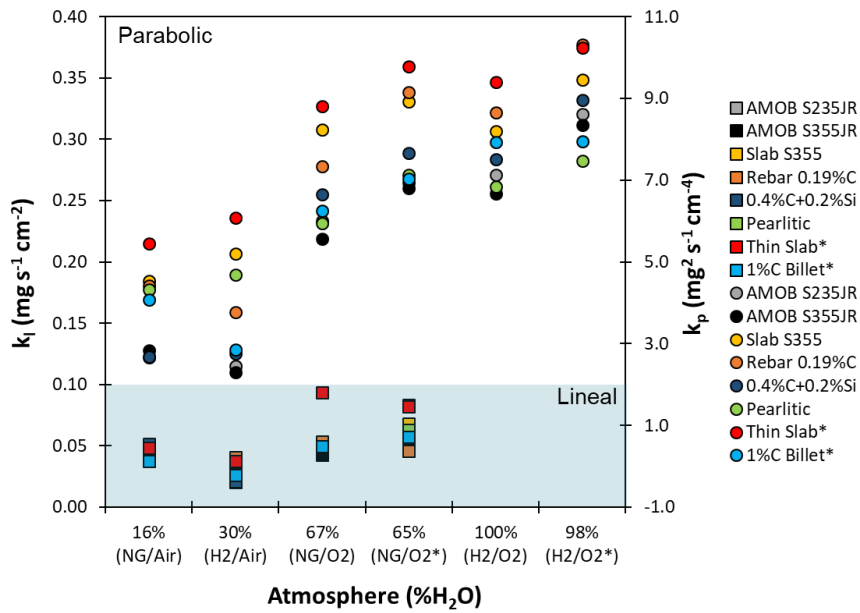
Figure 43. Visualization of k_l and k_p. (*Thin Slab and 1%C Billet data from a previous work).

D.3.3 Material embrittlement assessment

Hot torsion tests have been carried out to investigate the possible embrittlement of the material as a result of the change in atmosphere during the reheating stage prior to hot rolling, as described in Section D.2.5.

As an example, Figure 44 shows the appearance of the specimens after tests to fracture for the material AMOB S235JR.
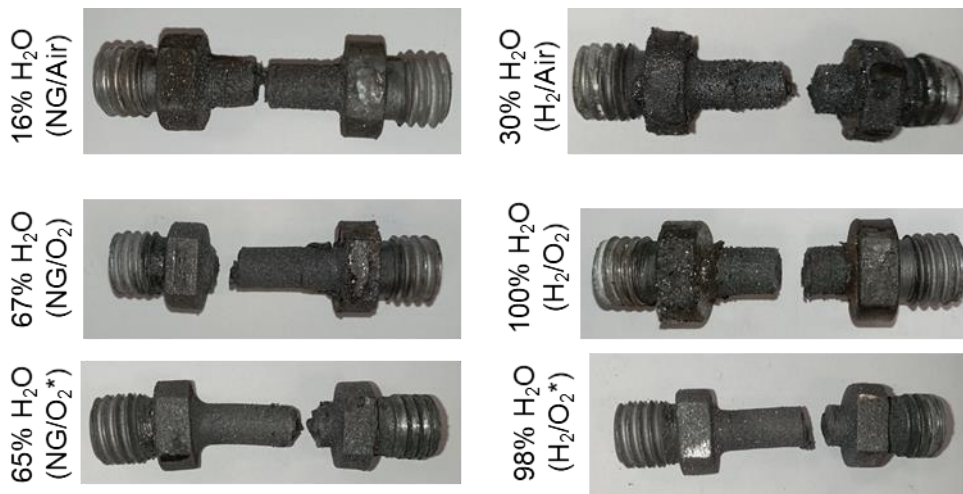
Figure 44. Appearance of the specimens after hot torsion tests to fracture for the material AMOB S235JR.

Figure 45, Figure 46, Figure 47 and Figure 48 show the stress-strain curves corresponding to the tests to fracture and two-pass tests carried out. It should be noted that a correction of the stress levels with the final specimen section is necessary due to the significant loss of mass due to oxidation. Once corrected, no differences in stress levels are observed depending on the atmosphere applied. It has been also observed that the strain to fracture was high in all the cases, indicating all the materials exhibited ductile behaviour.

HYINHEAT
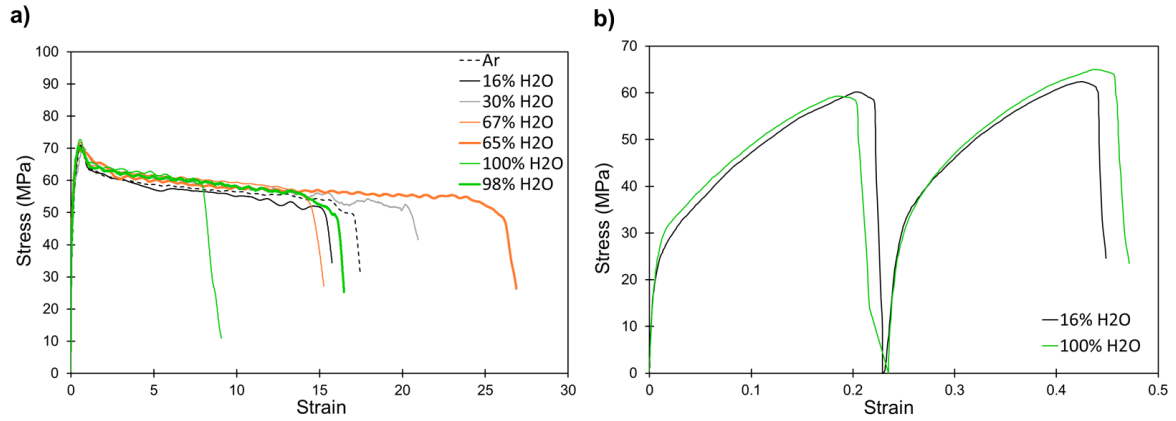
Figure 45. Stress-strain curves for hot torsion testing of AMOB S235JR, a) tests to fracture and b) two-pass tests after application of different atmospheres.
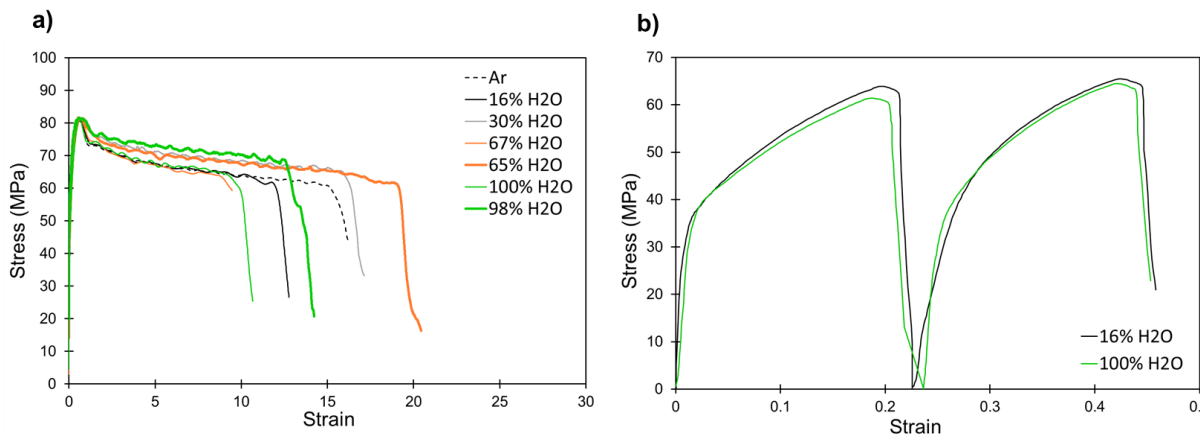
Figure 46. Stress-strain curves for hot torsion testing of AMOB S355JR, a) tests to fracture and b) two-pass tests after application of different atmospheres.
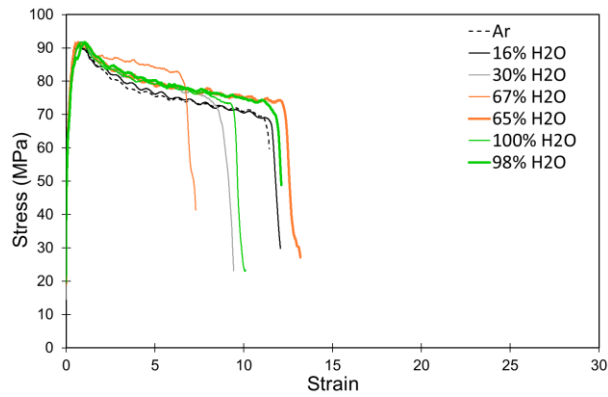
Figure 47. Stress-strain curves for hot torsion tests to fracture of Thin Slab material after application of different atmospheres.

HYINHEAT
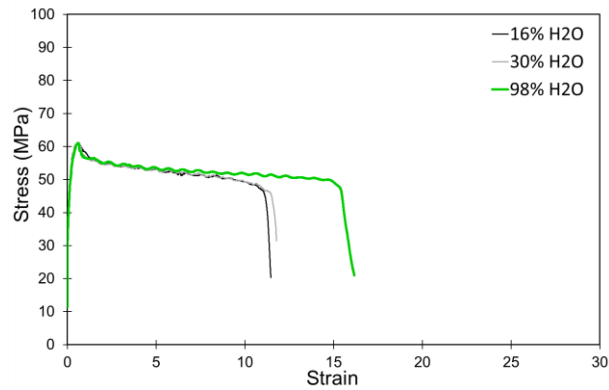
Figure 48. Stress-strain curves for the hot torsion tests to fracture of 1%C Billet material after application of different atmospheres.

Figure 49 shows the distribution of the number of cracks per unit length measured after the two-pass torsion tests under the influence of different atmospheres for AMOB S235JR and AMOB S355JR materials. The results obtained show a similar generation of defects during the first stages of deformation under the influence of the two atmospheres studied in this case (16% and 100% H_2O).
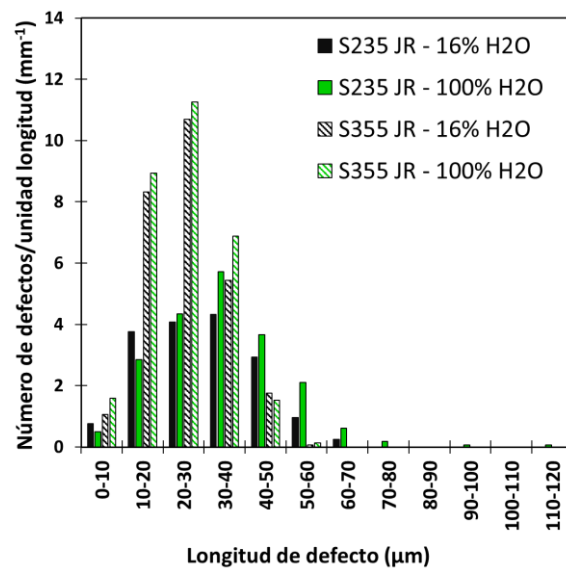
Figure 49. Distribution of the number of cracks per unit length measured after the two-pass torsion tests for materials AMOB S235JR and AMOB S355JR.

Table 15 summarises the main results obtained from the hot torsion test together with the calculated cracking susceptibility parameters n_{cracks}/L, l_{cracks}/L, E_e and E_p (Equation 3, Equation 4, Equation 5 and Equation 6) for the different materials. The results indicate that there is no evidence of severe embrittlement in any of the deformation modes analysed.

HYINHEAT

Table 15. Summary of cracking susceptibility parameters calculated from test to fracture curves (E_e, and E_p) and metallographic analysis of two-pass torsion test specimens (n_{cracks}/L and l_{cracks}/L).

Steel ID	Atmosphere (%H₂O)	ε_{MAX} (mm/mm)	σ_{MAX} (MPa)	E_e (%)	E_p (%)	n_{cracks}/L (cm⁻¹)	l_{cracks}/L (cm⁻¹)
AMOB S235JR	Ar	16.6	70.4	-	-	-	-
	16%	15.2	67.4	8.4	4.4	170	0.56
	30%	20.5	61.9	0*	12.1	-	-
	67%	14.1	63.5	15.3	9.9	-	-
	65%	25.4	63.7	0*	9.5	-	-
	100%	7.9	66.7	52.6	5.3	202	0.80
	98%	16.0	64.8	3.3	8.0	-	-
AMOB S355JR	Ar	15.3	81.6	-	-	-	-
	16%	12.2	74.4	19.8	8.8	273	0.69
	30%	16.2	77.6	0*	4.9	-	-
	67%	8.8	72.9	42.2	10.7	-	-
	65%	19.2	76.5	0*	6.2	-	-
	100%	9.3	64.5	39.1	21.0	303	0.73
	98%	12.7	70.6	16.6	13.5	-	-
Thin Slab	Ar	11.4	91.8	-	-	-	-
	16%	11.6	84.8	0*	7.6	-	-
	30%	8.6	80.7	23.4	12.0	-	-
	67%	6.6	63.9	41.8	30.4	-	-
	65%	12.4	74.0	0*	19.4	-	-
	100%	9.4	77.0	17.2	16.05	-	-
	98%	11.9	76.0	0*	17.2	-	-
1%C Billet	16%	11.2	57.3	-	-	-	-
	30%	11.5	55.3	-	-	-	-
	98%	15.4	56.4	-	-	-	-

*When strain values at break are higher than those obtained for Ar, (which is defined as the reference condition with the expected highest strain to fracture values) the resulting negative values of the E_e **(%)** parameter are converted to 0.

D.4 Conclusions

1. Different heat treatments, thermogravimetric analyses and thermomechanical tests have been successfully carried out for a set of carbon steels in order to evaluate the impact of H₂ heating during the reheating stage.

2. Quantitative measurements carried out after anisothermal heat treatments (industrial cycles with a holding time of 15 minutes) show that the major effect is given by the use of oxy-combustion conditions rather than by the type of fuel (NG/H₂). The use of oxy-combustion (67% and 100% H₂O) causes a higher oxidation than the air combustion (16% and 30% H₂O). Moreover, the presence of 2% free O₂ during oxy-combustion was found to increase this effect (atmospheres 98% and especially 65% H₂O).

3. Microstructural characterisation has shown that there is an effect on the modification of surface as a function of the applied atmosphere, which is related to the type of oxidation mechanism activated. Two different types of mechanisms have been identified. The Type I mechanism is characterised by the presence of a thick, smooth layer of magnetite formed by independent crystallographic units, whereas in the Type II mechanism, the oxide is characterised by being mainly composed of very large grains of wustite. In general terms, 16% H₂O atmosphere activates the Type I oxidation mechanism, while 67%, 65%, 100% and 98% H₂O atmospheres activated the Type II mechanism. 30% H₂O atmosphere is able to activate one or the other mechanism depending on the material.

4. Characterisation has also shown that in the interface region the morphology, the presence of phases and their characteristics, as well as the internal oxidation, are particularly dependent on the composition of the steel grade (while, in general, there is no obvious effect of the atmosphere). Only for specific steel grades, when a 65% H₂O atmosphere was applied, significant changes in the interface have been observed.

5. Thermogravimetric analyses carried out in isothermal oxidation tests show the same trends as those obtained in the anisothermal heat treatments. K₁ and especially k_p values obtained confirm that the

HYINHEAT

kinetics are lower when 16% and 30% H_2O atmospheres are applied than when 67% and 100% H_2O are used. Slightly higher k_p values are generally found when free O_2 is present in these atmospheres (65% and 98% H_2O atmospheres). Additionally, k_p values show that, in general, some of the materials are more susceptible to oxidation than others for the same atmosphere.

6. Hot torsion tests have been successfully carried out to investigate the possible embrittlement of the materials as a result of the change in atmosphere during the reheating stage prior to hot rolling. Strain-stress curves have shown that the strain accumulation was high in all the cases, indicating that all the materials studied exhibited ductile behaviour. Cracking susceptibility parameters also indicate that there is no evidence of severe embrittlement in any of the conditions analysed.

HYINHEAT

E. Impact of H₂ heating cycles on refractory materials from TCUK

E.1 Introduction

The objective of this study is to evaluate the behaviour of the refractory materials used as linings in the reheating furnaces for steel reheating process when they are heating and exposed to H_2 combustion atmospheres instead of NG. On the one hand, fibre-based blankets and modules and on the other hand, bricks produced by TCUK have been studied. For that, laboratory heating cycles have been performed under different water vapour atmospheres that reproduce the atmospheres generated in the combustion of NG and H_2 with air or O_2.

E.2 Materials and experimental procedure

E.2.1 Selection of refractory materials (TCUK)

Refractories from TCUK used in AMS and AMO reheating furnaces were selected for this study. Additionally, TCUK made an alternative selection of some of their promising material grades used for these applications. The evaluation of their behaviour under the atmospheres that arise from the combustion of H_2 with both, air or oxygen, in comparison to GN combustion, was studied. Two blanket, two modules (pyrolog) and three different bricks have been supplied to CEIT (Figure 50) by TCUK to perform this study at laboratory scale.
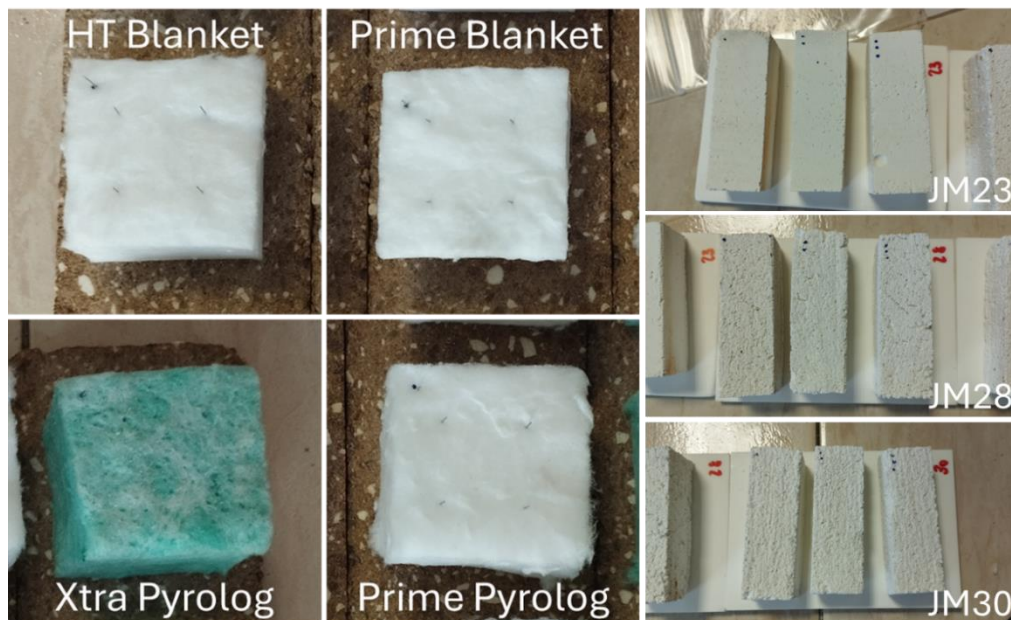
Figure 50. Materials supplied by TCUK for this study.

The composition and classification temperature of the fibre-based materials and brick is shown in Table 16 and Table 17, respectively.

Table 16. Fibre-based insulation materials from TCUK used for this study.

Fibre-based materials	Base composition	Classification T (°C)	Used in furnace
Superwool® HT Blanket	SiO_2-CaO-MgO	1300	Reheating – AMOB Tunnel - AMS
Superwool® Prime Blanket	SiO_2-CaO	1300	TCUK proposal
Superwool® Prime Pyrolog	SiO_2-CaO	1300	TCUK proposal
Superwool® Xtra Pyrolog	Al_2O_3-SiO_2-K_2O-ZrO_2	1450	TCUK proposal

HYINHEAT

Table 17. Refractory brick from TCUK used for this study.

Bricks	Base composition	Classification T (°C)
JM23	SiO_2-Al_2O_3-CaO	1260
JM28	Al_2O_3 - SiO_2	1540
JM30	Al_2O_3 - SiO_2	1650

E.2.2 Experimental procedures

E.2.2.1 Characterization of as-received materials

The as-received materials have been characterized to define their baseline properties. The characterisation carried out includes bulk density, microstructure and compositional analysis by FEG-SEM/EDS and XRD, resilience and mechanical properties. The tests were carried out on samples of different dimensions according to their nature. The fibre-based materials were cut to size: 45 x 45 mm^2 with a height of ~ 20 mm for the blankets and 30 mm for the modules. The refractory bricks were cut to size: 60 x 16 x 20 mm^3 (L x b x h - Figure 51).
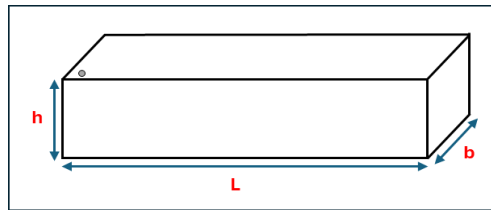
Figure 51. Sample dimensions of the JM bricks studied.

The bulk density and porosity have been measured in two different ways depending on the nature of the material:

- *Blankets and modules*: bulk density was determined geometrically. The volume has been measured using a steel rule, capable of being read to 0.5 mm and the thickness was determined using a digital indicator, a metallic disc (50 mm diameter, 1.47 N) and a reference plate, according to the ISO 1063:1999.
- *Bricks:* bulk density, apparent porosity and skeletal density were calculated by Archimedes' method, using the following equations:

$$Bulk\ density, kg/m^3 = \frac{m_1}{m_3 - m_2} \cdot \rho_{water} \cdot 1000 \qquad \text{Eq. 1.}$$

$$Skeletal\ density, kg/m^3 = \frac{m_1}{m_1 - m_2} \cdot \rho_{water} \cdot 1000 \qquad \text{Eq. 2.}$$

$$Apparent\ porosity, \% = \frac{m_3 - m_1}{m_3 - m_2} \cdot \rho_{water} \cdot 1000 \qquad \text{Eq. 3.}$$

m_1: initial mass $\qquad$ m_3: mass outside the water
m_2: mass inside the water $\qquad$ ρ_{water}: water density at room temperature

Fibre diameter

The fibre's diameter has been measured using an equipment from Sympatec that measure the particle size distribution by dynamic image analysis. Samples were previously dried at 110 °C for 2 hours to eliminate any moisture present and then were crushed to detach the fibres from each other. The equipment can evaluate millions of particles in short time guaranteeing statistically relevant results. Additionally, different filters, like

HYINHEAT

the size of fibre diameter or ones related to the morphology of the particles, can be applied to remove the non-fibre particles as shots, powder or fibres agglomerations.

Resilience

Resilience is the ability of a ceramic fibre products to spring back after compression of 50% of thickness. This property has only been measured on blankets and modules according to the ISO 10635:1999 using samples of 45 x 45 mm^2. Instron 5982 equipment (Figure 52.a) was employed to perform these measurements and the materials under investigation were previously dried at 110 °C for at least two hours. The resilience is calculated after the test using *Eq. 4*. and the reported value is based on the average of two samples.

$$Resilience, \% = \frac{h_f}{h_0} \cdot 100$$

h_0: initial height
h_f: final height

Eq. 4.

Figure 52. a. Instron 5982 – resilience test setup; b. Upper tooling; c. Lower tooling.

Mechanical strength: Three-point bending test

The mechanical properties of the refractory bricks have been determined by three-point bending tests. The Instron 5982 (Figure 53) machine has been used for this test with the tooling shown in the Figure 53.b with a distance of 50 mm between bolts and a crosshead speed of 0.5 mm/min. Results reported are the average value of three samples.
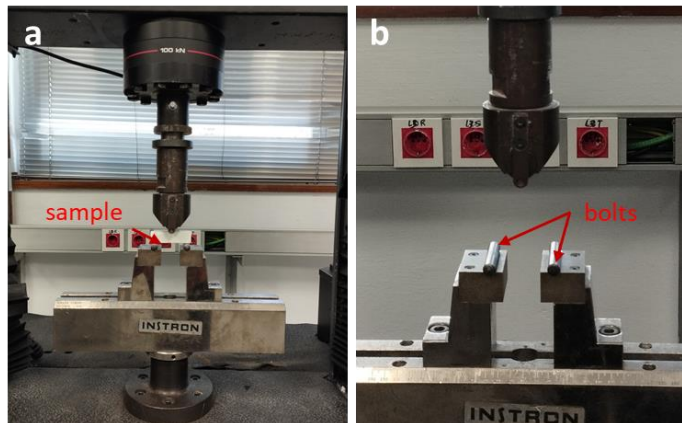
Figure 53. a. Instron 5982 – three-point bending test setup; b. Upper and lower tools.

E.2.2.2 Heat treatments (HTs)

In order to assess the suitability of the materials under the conditions of the combustion atmospheres when replacing natural gas (NG) by hydrogen (H₂), different HTs under the four atmospheres shown in Table 18 have been carried out. Samples of 45 x 45 mm^2 cut from the original blanket and modules have been used for this study, always maintaining the production direction, while in the case of refractory bricks, samples of 18 x 60 x 20 mm^3 were used.

Impact of H_2 heating on product quality, yield, and refractory

Table 18. Composition of the combustion atmospheres employed. White for reference and light grey for proposed atmospheres // Ar* is used only as carrier gas.

Combustion atmosphere	Products, %				
	CO_2	O_2	N_2	H_2O	Ar*
NG/Air	8.0	3.4	72.6	16.0	
NG/O_2	33.0			67.0	
H_2/Air		3.1	67.3	29.6	
H_2/O_2				86.0	14.0

For the simulation of different combustion atmospheres, a set-up has been designed at CEIT, whose configuration is shown in Figure 54 and consists of:

- Coriolis effect mass flowmeter for the control of distilled H_2O.
- CEM (Controlled Evaporator and Mixer) system, by which the defined amount of liquid (H_2O) is vaporized and mixed with the carrier gas.
- Temperature controller and power supply.
- Mass Flow Controllers (MFCs) with different output pressures and calibrated for different gases. The different MFCs allow the generation of different types of mixtures containing different gases (CO_2, O_2, N_2, Ar, ect.).
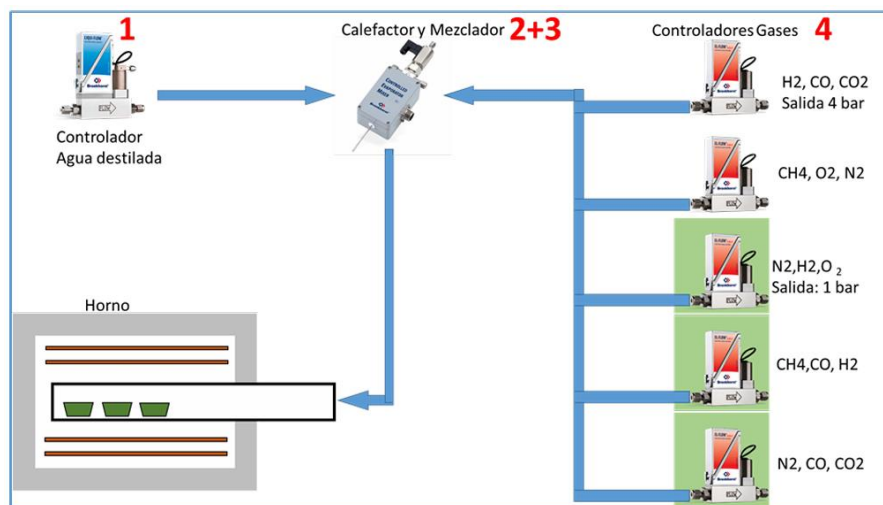
Figure 54. Steam generator-gas mixer system scheme.

The system requires a minimum carrier gas flow rate for proper operation, which means the addition of a minimum carrier gas flow rate in the 100% H_2O atmospheres. The carrier gas (Ar) accounts for 18% vol. of the total mixture in this case.

The thermal cycles under the previously mentioned atmospheres have been carried out in a Carbolite TZF tubular furnace with an Al_2O_3 tube, where the samples are introduced, and the steam generator-gas mixer system that has been described above. The test temperature has been set at 1200 °C with a holding time of 28 and 48 hours for fibre-based materials and 1250 °C with a holding time of 48 h for refractory bricks, heating and cooling rates was 3 °C/min in both cases.

Additionally, HTs under pure H_2 have been also performed to assess the stability of the materials in the case of an incomplete H_2 combustion takes place. These HTs have been performed at 1200 °C with a dwell time of 8 and 24 h applying a heating rate of 20 °C/min and a free cooling.

HYINHEAT

E.2.2.3   Characterization after HT

To evaluate the impact of water vapour exposure on the materials, a series of characterisations have been carried out. These include mass loss and dimensional changes, which have been determined in each case to assess the potential changes that could compromise the integrity of the materials during their service life. Microstructural and compositional analysis have been performed by FEG-SEM/EDS and XRD to investigate the potential alterations in the microstructure or composition of the materials that may be associated with the loss of their refractory properties. In addition, fibre diameter analysis, resilience and three-point bending tests have been performed in accordance with the procedures explained in the section E.2.2.1.

Dimensional changes have been measured as follow depending on the type of material:

- *Blankets and modules*: a procedure based on ISO 10635 has been followed. Samples of 45x45 mm² were used and four platinum wires were inserted as shown in Figure 55. Measurements between the inner and outer ends of each wire were taken to determine the distances L1, L2, L3 and L4 before and after the thermal cycle using a digital microscope DinoLite AM4013MZTL. The calculation of the dimensional of the sample is based on the difference of each distance L and calculated with the Eq. 5.

$$Dimensional\ change, \% = \frac{L_f - L_0}{L_0} \cdot 100$$

L_0: initial distance   *Eq. 5.*
L_f: final distance

According to the similar results obtained in both dimensions (L1/L3 and L2/L4), it was decided to report the average of the four L distances as the value of dimensional change for each material after the thermal cycles.
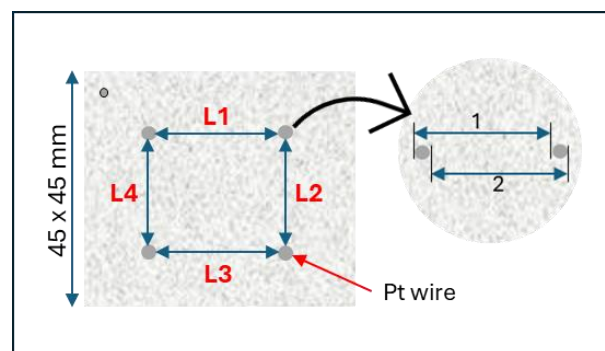
Figure 55. Measurement configuration for dimensional changes on blankets and modules.

- *Bricks*: the dimensional change has been determined measuring the three dimensions of the bars. Width (b) and height (h) were measured using a digital indicator while the measurements of the length (L) were made with a calliper. Measurements were taken before and after the thermal cycles, and the dimensional changes were calculated according to Eq. 5.

E.3   Results and discussion

E.3.1   Characterisation of as-received materials

The initial step was to characterise the selection of materials provided by TCUK included in section E.2.1 The objective was to identify the intrinsic properties of each material and to establish a reference point for subsequent evaluations of the potential degradation after the thermal cycles. The characterisation was carried out following the procedures explained in the section E.2.2.1. The properties of the as-received materials, fibre-based and bricks, are shown below.

Fibre-based materials

The density and resilience of the fibre-based materials in the as-received state are shown in Table 19. A debinding cycle at 650 °C for 1 hour in air was applied to the pyrolog-type materials to remove the binder that may affect to the reference resilience value.

HYINHEAT

Impact of H₂ heating on product quality, yield, and refractory

Table 19. Density and resilience values obtained for the fibre-based materials in as-received state and after debinding in the case of modules.

Material	Density (kg/m³)	Resilience, %	
		As-received	Debinded
Superwool® HT Blanket	136 ± 6	70 ± 1	-
Superwool® Prime Blanket	150 ± 10	77 ± 1	-
Superwool® Prime Pyrolog	175 ± 7	87 ± 3	71 ± 7
Superwool® Xtra Pyrolog	210 ± 20	74 ± 2	70.8 ± 0.5

As observed, materials with different density have been evaluated, having higher density the modules-type materials, specially the Xtra Pyrolog. Regarding resilience, in general there are no significant differences between materials if values after debinding are compared. Prime Pyrolog is the one that shows a higher value, which is much higher than its blanket version. However, the resilience after removing the binder is similar in both cases. This reduction in resilience after de debinding cycle has been attributed to the presence of moisture in the as-received samples rather than to the removal of binder, since the mass loss of this material during debinding cycle is negligible.

In the case of the Xtra Pyrolog, this material has a binder content of 1% approximately and when this binder is removed, a reduction in resilience is observed, having a similar value than Prime Pyrolog and Prime blanket.

The fibre diameter distribution is presented in Figure 56 where an average of the indicators D10, D50 and D90 are represented from 11490, 7282, 2379, and 1474 fibres for the materials HT Blanket, Prime Blanket, Prime Pyrolog and Xtra Pyrolog, respectively. The average fibre diameter (D50) is quite similar among materials (10, 9, 8 and 11 μm for HT Blanket, Prime Blanket, Prime Pyrolog and Xtra Pyrolog, respectively), while the distribution is narrower for the Prime formulation, both blanket and pyrolog.

These values correlate well with the fibre diameter measurements obtained via electron microscopy (FEG-SEM) on a smaller number of fibres.
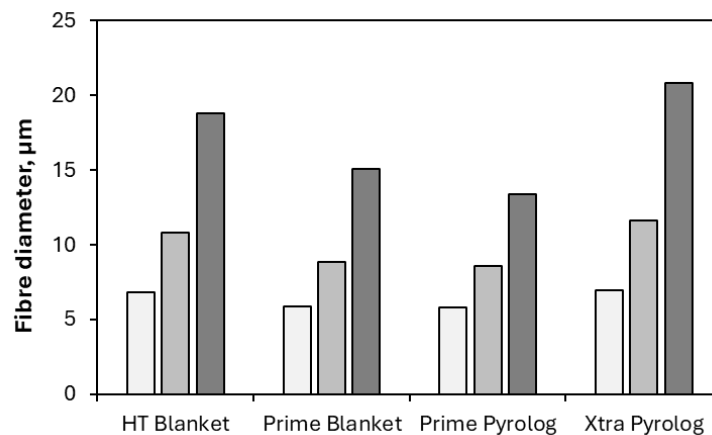
Figure 56. Fibre diameter of unfired materials analysed by dynamic image analysis with QICPIC equipment and VIBRI module. From lightest to darkest D10, D50 and D90.

The microstructure of the unfired HT Blanket, Primer Blanket, Prime Pyrolog and Xtra Pyrolog are shown in the Figure 57, Figure 58, Figure 59 and Figure 60, respectively. Is it observed that all the materials have a presence of shots, which are non-fibrous particles or particles that are not completely transform into fibres during the production process and that can compromise the insulating capacity of the materials. The number of shots seems to be lower in the Prime formulation (blanket and module) and in the Xtra Pyrolog.

The materials seem to have a homogeneous composition, as no significant differences in compositional contrast can be observed, only in the Xtra Pyrolog can be distinguished dark areas on the surface of the fibres that have been identified with the dye/binder that is present in this formulation. Regarding the morphology

HYINHEAT

of the fibres, there are no significant differences between HT and Prime while the fibres of the Xtra Pyrolog are more flattened.
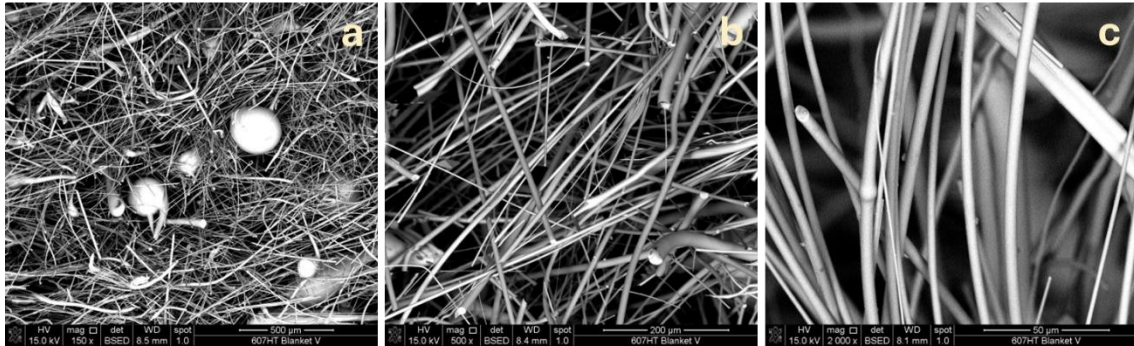
Figure 57. BSED micrographs of unfired HT Blanket; a. 150x; b. 500x; c. 2000x.
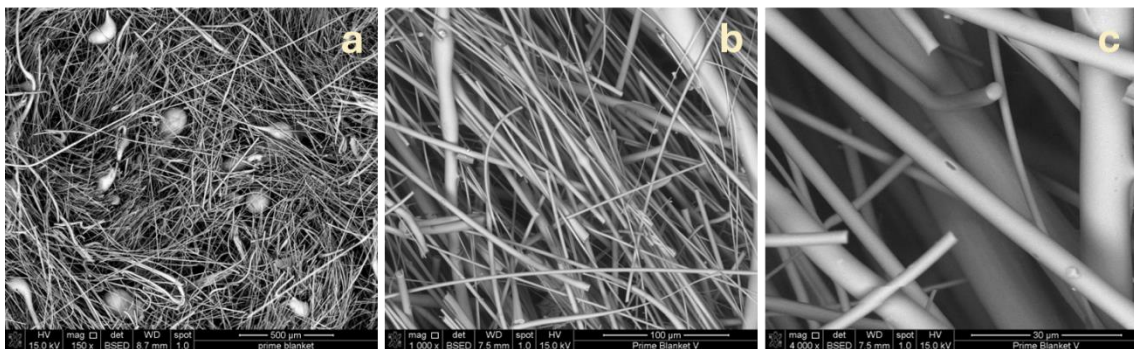
Figure 58. BSED micrographs of unfired Prime Blanket; a. 150x; b. 1000x; c. 4000x.
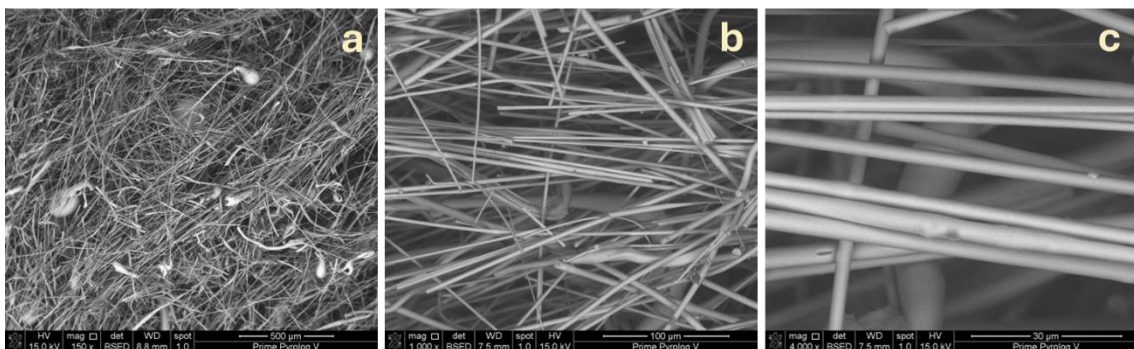
Figure 59. BSED micrographs of unfired Prime Pyrolog; a. 150x; b. 1000x; c. 4000x.

Figure 60. BSED micrographs of unfired Xtra Pyrolog; a. 150x; b. 1000x; c. 4000x.

The elemental composition of each fibre-based material was determined by EDS, and the corresponding semi-quantitative weight percentages of the oxides were calculated and shown in the Table 20. XRD patterns

HYINHEAT

of the fibre-based materials have not been included in this study, as their unfired nature is amorphous, and they do not provide relevant information.

Table 20. Compositional analysis of unfired fibre-based materials determined by EDS.

wt. % by EDS	MgO	Al$_2$O$_3$	SiO$_2$	K$_2$O	CaO	ZrO$_2$
Superwool® HT Blanket	0.7	1.4	69.9	1.2	27.4	-
Superwool® Prime Blanket	0.1	0.7	62.0	0.2	37.0	-
Superwool® Prime Pyrolog	0.1	0.7	62.1	0.2	36.8	-
Superwool® Xtra Pyrolog	0.6	29.6	34.0	28.8	-	6.9

Refractory bricks

The density and porosity of the bricks are shown in Table 21. As observed, the three materials exhibit different grades of densification, increasing the density with the amount of Al$_2$O$_3$ in the formulation (JM23 < JM28 < JM30).

Table 21. Density measurements for unfired refractory bricks by hydrostatic weighing method.

Materials	Bulk density, kg/m^3	Skeletal density, kg/m^3	Apparent porosity, %
JM23	508 ± 4	2413 ± 3	79.0 ± 0.1
JM28	942 ± 13	3052 ± 1	69.1 ± 0.4
JM30	1086 ± 7	3204 ± 2	66.1 ± 0.2

The module of rupture (MOR), measured by three points bending test, of the three bricks are presented in Table 22. Although there are no significant differences among the materials, the values obtained are in line with their density, with JM23 exhibiting the lowest mechanical strength.

Table 22. Module of rupture measurements for unfired JM bricks.

Material	MOR, MPa
JM23	0.8 ± 0.1
JM28	1.4 ± 0.3
JM30	1.1 ± 0.1

X-ray diffraction (XRD) analyses were conducted on unfired refractory bricks to identify their main phases. Additionally, the composition was determined by quantitative analysis based on the X-ray diffractograms. The diffractograms for JM23, JM28 and JM30 are presented in Figure 61, Figure 62 and Figure 63, respectively.

As observed, the JM23 brick consists of two phases, anorthite (1) and mullite (2), being the anorthite the main one (91%). In the case of brick JM28 (Figure 62), two distinct crystallographic phases were identified, which are 67% mullite (Al$_{2.25}$Si$_{0.75}$O$_{4.87}$) and 33% corundum (Al$_2$O$_3$). For brick JM30 (Figure 63), quantification analyses reveal that this material is composed of 52% mullite (Al$_{2.25}$Si$_{0.75}$O$_{4.87}$), 47% corundum (Al$_2$O$_3$), and 1% quartz (SiO$_2$).

HYINHEAT
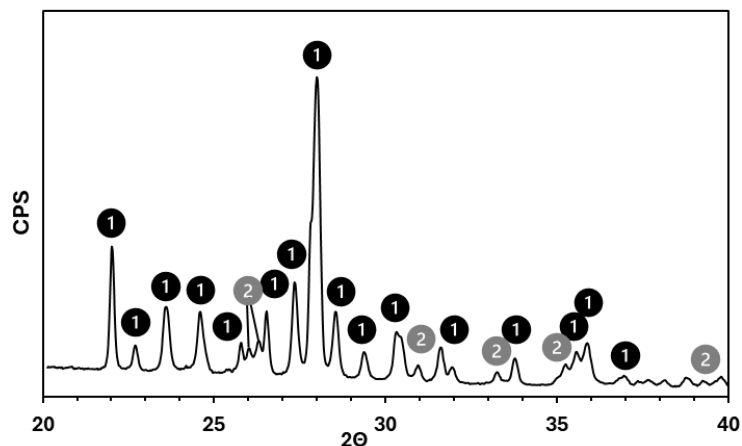
Figure 61. X-ray diffraction pattern of unfired JM23; 1. Anorthite ($Al_2CaSi_2O_8$); 2. Mullite ($Al_{2.25}Si_{0.75}O_{4.87}$).
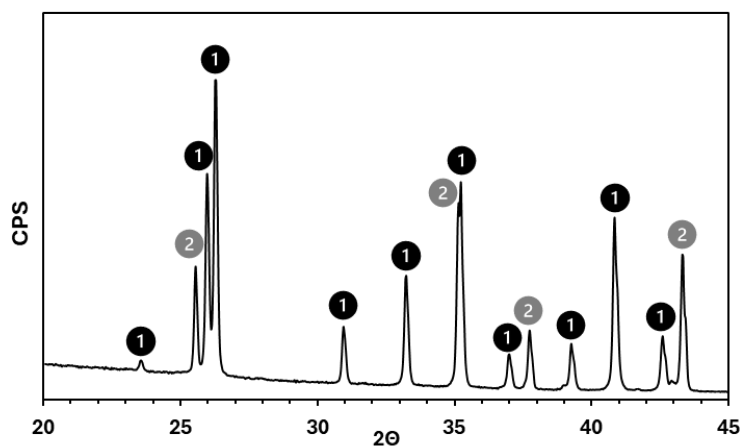
Figure 62. X-ray diffraction pattern of unfired JM28; 1. Mullite ($Al_{2.25}Si_{0.75}O_{4.87}$); 2. Corundum ($Al_2O_3$).
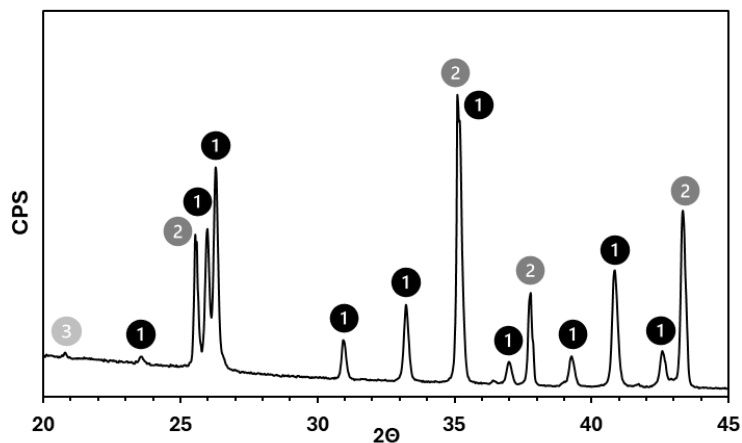
Figure 63. X-ray diffraction pattern of unfired JM30; 1. Mullite ($Al_{2.25}Si_{0.75}O_{4.87}$); 2. Corundum ($Al_2O_3$); 3. Quartz ($SiO_2$).

Micrographs of the backscattered electrons (BSED) of the JM23, JM28 and JM30 are shown in Figure 64, Figure 65 and Figure 66, respectively. In general, JM28 and JM30 bricks show a more cohesive microstructure than JM23, which is in well agreement with the density/porosity values (Table 21). The different phases identified by XRD in each brick are not easily distinguished in the microstructure.

HYINHEAT
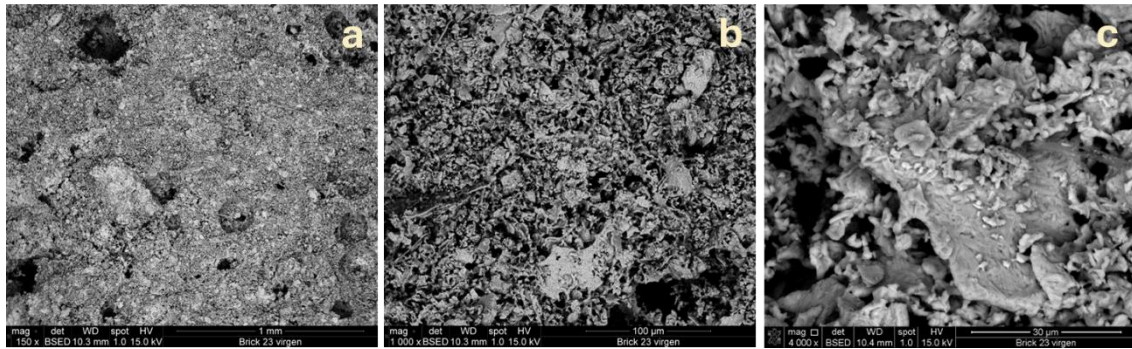
Figure 64. Micrographs of unfired JM23; a. 150x; b. 1000x; c. 4000x.

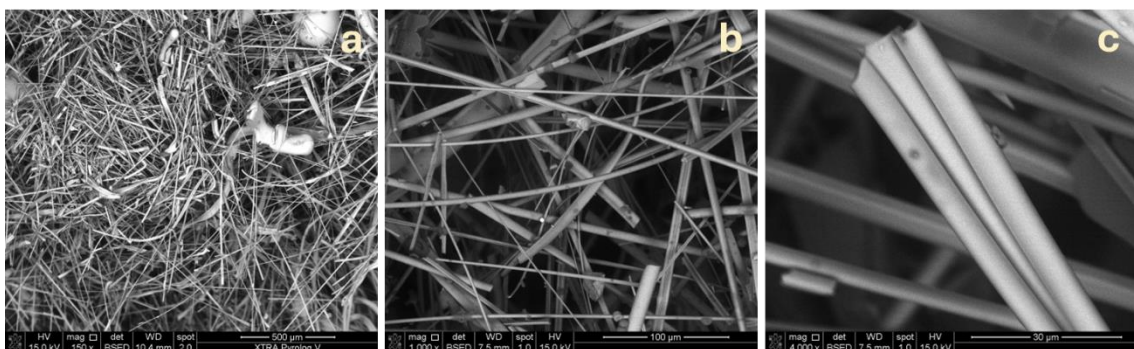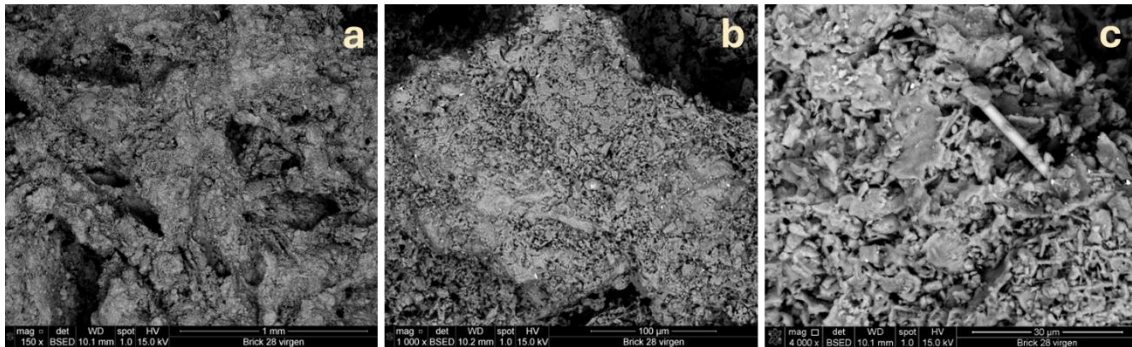*Figure 65. Micrographs of unfired JM28; a. 150x; b. 1000x; c. 4000x.*
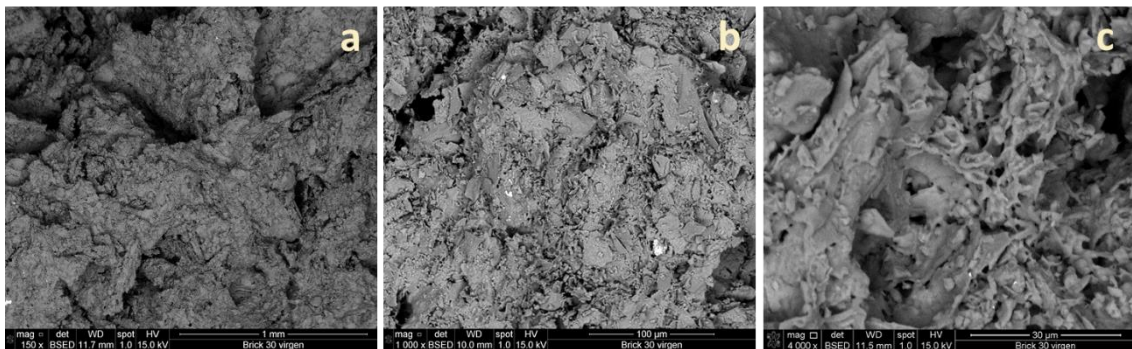
Figure 66. Micrographs of unfired JM30; a. 150x; b. 1000x; c. 4000x.

The elemental composition of each refractory brick was determined by EDS, and the corresponding weight percentages were calculated based on the oxides present and shown in the Table 23. The values obtained by EDS for the majority of the oxides present in the bricks are slightly lower than the corresponding ones to the phases identify by XRD. This may be due to the fact that the minority oxides, like K$_2$O, TiO$_2$ and Fe$_2$O$_3$, have not been detected by XRD and, consequently, the rest of the oxides are being overestimated.

Table 23. Compositional analysis of unfired refractory bricks determined by EDS.

wt. % by EDS	Na$_2$O	MgO	Al$_2$O$_3$	SiO$_2$	K$_2$O	CaO	TiO$_2$	Fe$_2$O$_3$
JM23	0.0	0.2	32.4	42.5	0.8	22.5	0.4	1.2
JM28	0.3	0.2	60.1	36.3	1.2	0.2	0.8	1.0
JM30	0.5	0.2	55.8	40.0	1.0	0.3	1.2	1.0

E.3.2 Heat treatments on fibre-based materials

To evaluate the effect of H$_2$ combustion during the heating of the industrial furnaces on the refractory lining, HTs at laboratory scale have been carried out following the procedure explained in the section E.2.2.2. The main results obtained from this study is shown in the following sections.

HYINHEAT

E.3.2.1 Effect of water vapour atmospheres
First loop: HTs 1200 °C – 28 hours

The four materials have been heating in the four different atmospheres (NG/Air, H$_2$/air, NG/O$_2$ and H$_2$/O$_2$) proposed in this study following the procedure explained in the section E.2.2.2. In a first approach, a holding time of 28 hour were applied. An additional cycle in air, with the same condition that the previous ones, were carried out to identify the changes produced by the intrinsic crystallisation of the materials regardless the atmosphere used.

The mass losses and dimensional changes of each material were measured after each HT and the results are shown in Figure 67. As observed, there is a trend for all materials, with a higher mass loss as the water vapour content in the atmosphere increases, being the Xtra Pyrolog the one that presents a higher mass loss in all the atmospheres tested. This has been related to the burn-out of the binder of this material. It is important to note that the values reported for HT Blanket and Prime, both blanket and pyrolog, might to be higher than the real one due to a slight reaction with the plates.

On the other hand, no significant trends could be established for the dimensional changes in neither of the materials with the different atmospheres (Figure 67-b).

Figure 67. Mass loss (a) and dimensional changes (b) of fibre-based materials after HT-28h at different atmospheres. Air in grey, NG/Air in violet, H$_2$/Air in blue, NG/O$_2$ in orange, H$_2$/O$_2$ in green.

In order to check the occurrence of microstructural and compositional alterations after HTs, XRD analyses were performed. After HTs, regardless the atmosphere used, all the material crystalizes in the same crystalline structures.

For the HT Blanket, Prime Blanket, and Prime Pyrolog, cristobalite (SiO$_2$), wollastonite (CaSiO$_3$), and pseudowollastonite (CaSiO$_3$) were detected, with CaSiO$_3$ representing the predominant component and SiO$_2$ the minor one. The Xtra Pyrolog shows different crystalline phases due to their different composition, these are Kalsilite (AlSiKO$_4$), Leucite (AlSi$_2$KO$_6$) and ZrO$_2$.

A series of micrographs were taken at different magnifications of the selected materials subjected to different combustion atmospheres. These images, representing the backscattered electron micrographs (BSED) of the materials, are presented in Figure 68, Figure 69, Figure 70 and Figure 71. Additionally, images of the as-received materials are included for comparison.

Figure 68 presents the microstructure of the Superwool HT Blanket. After HTs, two primary phases can be identified, EDS analysis has determined that the whiter contrast phases correspond to wollastonite/pseudowollastonite (CaSiO$_3$), while the darker contrast areas correspond to cristobalite (SiO$_2$). Despite the fact that there are not differences in the crystallized phases with the HT atmosphere, the size of CaSiO$_3$ grains increases with the increase of water vapour content, (Figure 68 e and f).

HYINHEAT
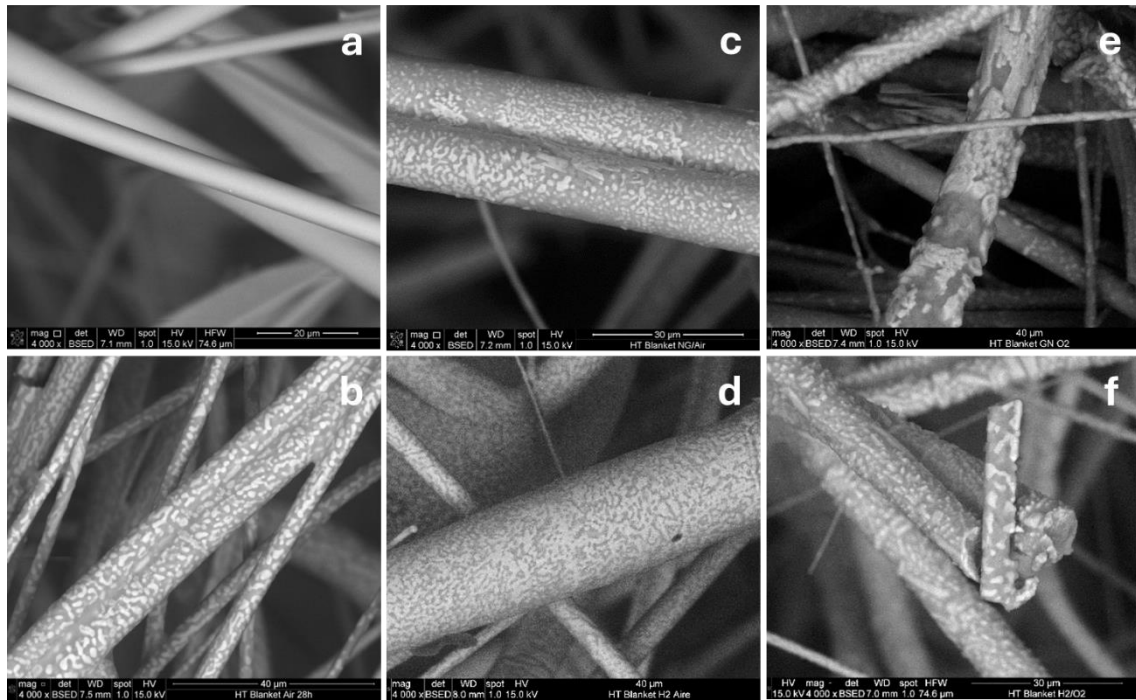
Figure 68. Micrographs of Superwool HT Blanket unfired and after the different heat treatments at 1200 °C - 28h; a. Unfired, b. Air, c. NG/Air, d. H_2/Air, e. NG/O_2, f.H_2/O_2.

Figure 69 and Figure 70 show the micrographs of the Superwool Prime blanket and Pyrolog, respectively. A crystallisation behaviour analogous to that observed in the HT Blanket (Figure 68) has been identified in these materials. Two main phases can be distinguished, $CaSiO_3$ and SiO_2. In these materials, a slightly lower wollastonite/pseudowollastonite ($CaSiO_3$) grain growth than in HT Blanket material can be observed.
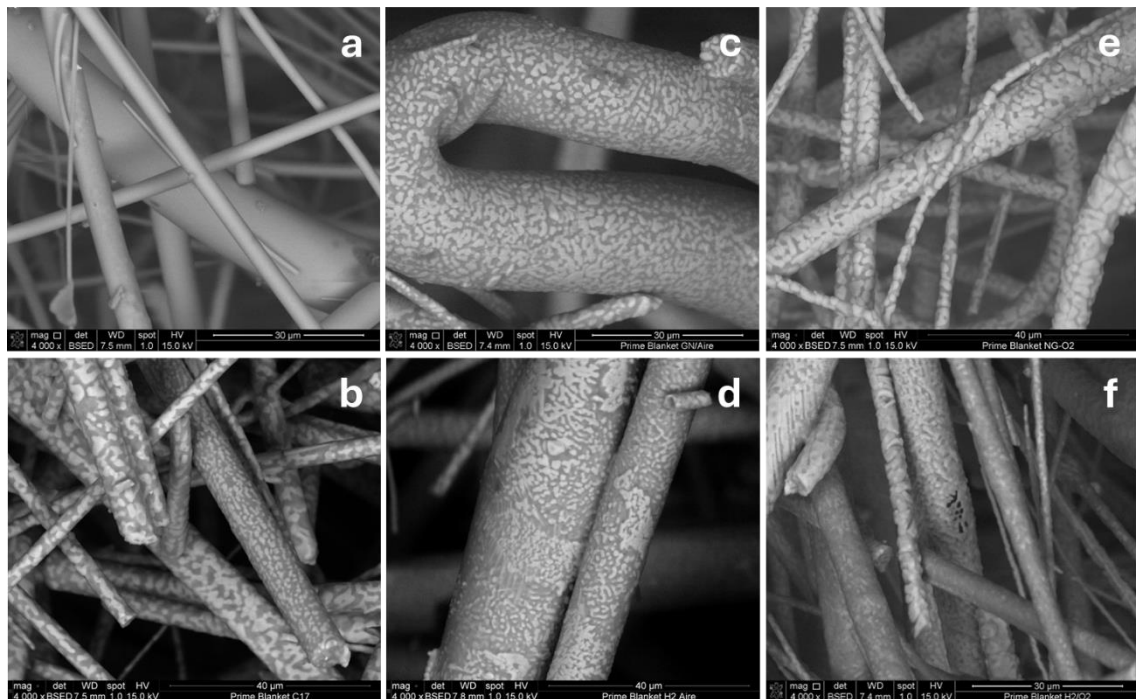
Figure 69. Micrographs of Superwool Prime Blanket unfired and after the different heat treatments at 1200 °C- 28h: a. Unfired, b. Air, c. NG/Air, d. H_2/Air, e. NG/O_2, f.H_2/O_2.

HYINHEAT
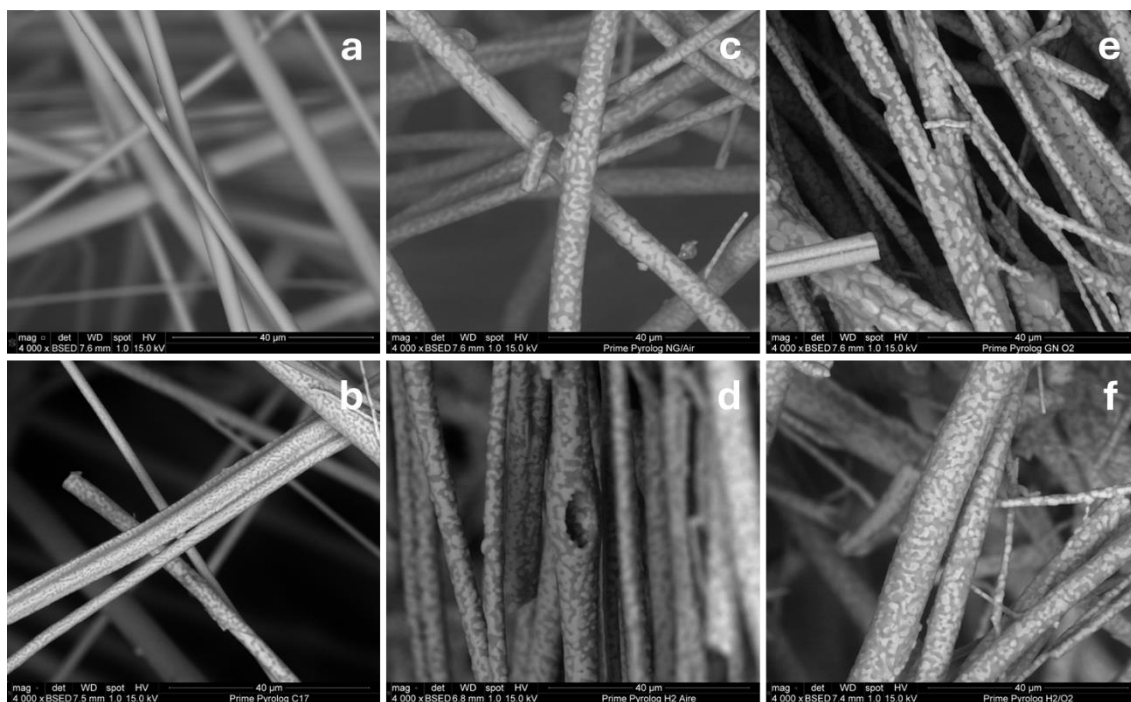
Figure 70. Micrographs of Superwool Prime Pyrolog unfired and after the different heat treatments at 1200 °C – 28 h: a. Unfired, b. Air, c. NG/Air, d. H₂/Air, e. NG/O₂, f.H₂/O₂.

The micrographs of the Superwool Xtra Pyrolog (Figure 71) show that an increase in the water vapour content is accompanied by a grain growth of the ZrO_2 crystals, which are the white points in the Figure 71 e and f.

The semi-quantitative results obtained by EDS analysis showed that no significant changes in the composition of the materials after heat-treatments were observed, for that, these tables have not been included in this report.
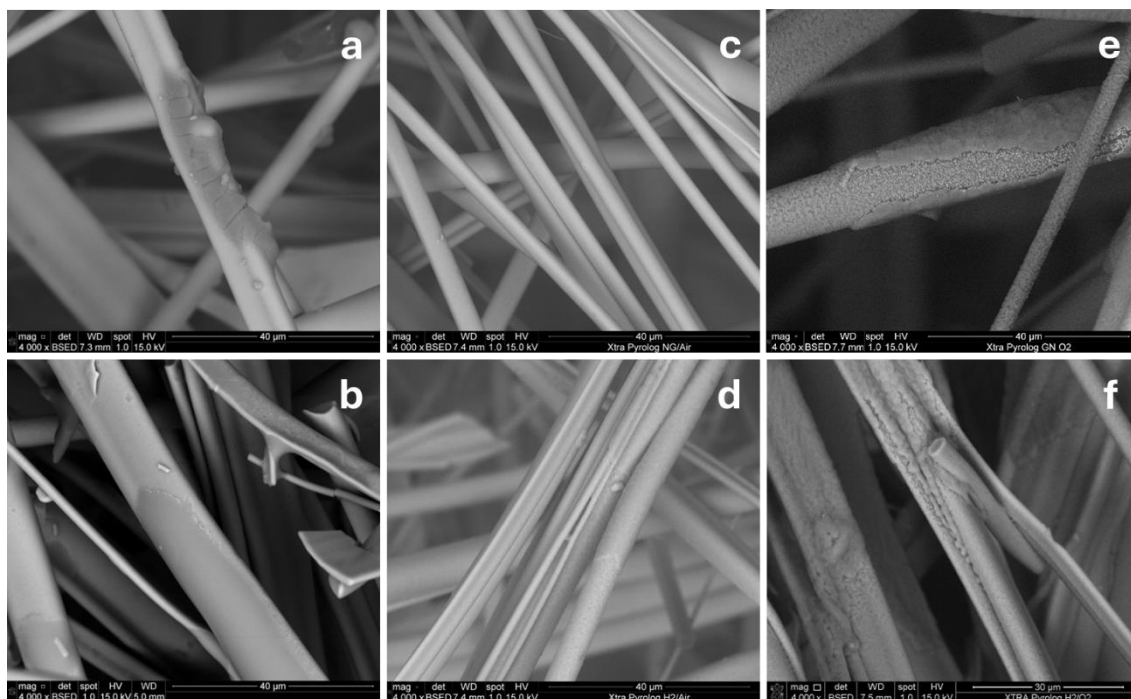
Figure 71. Micrographs of Superwool Xtra Pyrolog unfired and after the different heat treatments at 1200 °C – 28 h: a. Unfired, b. Air, c. NG/Air, d. H₂/Air, e. NG/O₂, f.H₂/O₂.

The results obtained in the first loop of HTs show no significant changes in the materials after HTs in the different atmospheres. This lack of consistent results, together with the fact that this kind of materials is

HYINHEAT

designed to have a service life of several months, indicates that HTs with higher holding time are required. However, due to the limitations of the laboratory resources and the timeline of the project, it has not been possible to perform very long HTs.

To determine the minimum holding time required to obtain more consistent results and to be able to see differences among atmospheres, a study of the effect of the holding time has been carried out. For that, HTs at 1200 °C during 28, 48 and 96 hours has been performed in air.
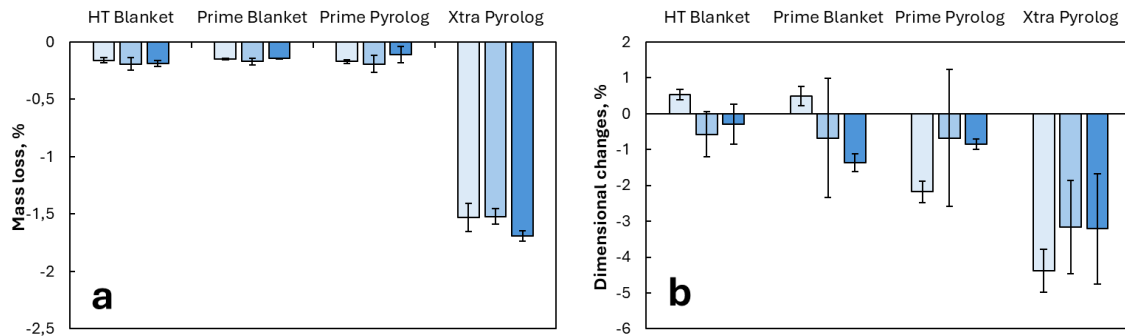
Figure 72. Mass loss and dimensional changes of fibre-based materials after HT in air under different holding times. From lightest to darkest: 28, 48 and 96 h.

The results of the mass loss and dimensional changes of each material after these HTs are shown in Figure 72. No significant differences were observed in the mass loss of the materials as function of the holding time. However, more consistent shrinkage results were obtained from 48 hours of dwelling time.

The resilience of the materials after HTs in air at the three different holding times are presented in Table 24. It is observed that the resilience exhibits minimal variation as function of holding time being the differences related to the experimental error.

Table 24. Resilience measurements after HT in air with different holding times.

Materials	Resilience, %			
	Unfired	28 h	48 h	96 h
Superwool® HT Blanket	70 ± 1	77 ± 2	71 ± 2	76 ± 2
Superwool® Prime Blanket	77 ± 1	67.1 ±0.3	63.8 ± 0.6	66 ± 1
Superwool® Prime Pyrolog	71 ± 7	62.4 ± 0.0	60.4 ± 0.4	64 ± 2
Superwool® Xtra Pyrolog	70.8 ± 0.5	58.4 ± 0.3	57.0 ± 0.7	58 ± 2

Second loop: HTs 1200 °C – 48 hours

Considering the results of the study of the effect of the holding time in air explained above, a second loop of HTs in the four water vapour atmospheres (NG/Air, H$_2$/air, NG/O$_2$, H$_2$/O$_2$) were performed at the same temperature than the ones before, 1200 °C, but with 48 h of holding time. The results obtained are shown and explained hereafter.

Figure 73 shows the dimensional changes of the fibre-based materials after the 2nd loop of HTs under the selected combustion atmospheres. As observed in this figure, the results obtained after 48 hours of holding time are more consistent than those obtained in the first loop of HT (Figure 67). After longer time HTs, the shrinkage of all the materials takes place, in contrast to the observations made in Loop 1, in which only the Xtra Pyrolog showed shrinkage in all the atmospheres. The graph shows that the shrinkage behaviour is dependent on the type of material, blanket or pyrolog, showing the last ones a higher shrinkage in all the atmospheres tested.

Analysing the effect of water vapour content during the HTs, no clear tendency in the dimensional changes of the materials as function of the HT atmosphere can be determined, especially in the blanket-type materials.

HYINHEAT

Impact of H$_2$ heating on product quality, yield, and refractory

In the case of the modules (Prime and Xtra), higher shrinkage takes places during the HT in the 100% water vapour atmosphere in both materials.
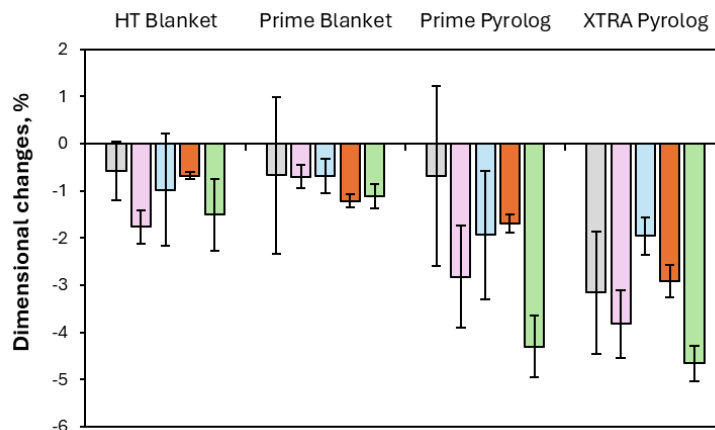
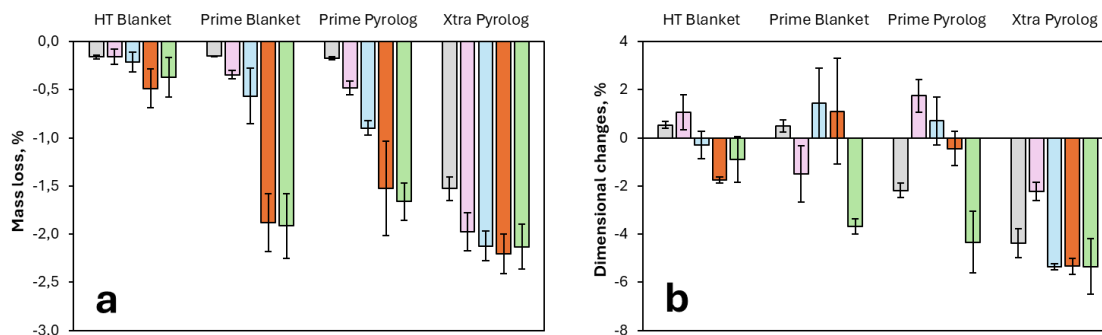*Figure 73. Dimensional changes of fibre-based materials after HT-48h at different combustion atmospheres. Air in grey, NG/Air in violet, H$_2$/Air in blue, NG/O$_2$ in orange, H$_2$/O$_2$ in green.*

The mass loss of the materials after the second loop of tests are presented in the Figure 74. Like the dimensional changes, the measured mass losses show a more consistent trend, compared to the results of the HTs performed during 28 h, shown in Figure 67, increasing in all materials as the water vapour content increases.

In this case, it is clearly seen how the mass loss increases with the water vapour content in the four materials tested. Prime formulation in both type of formats (blanket and pyrolog) is the one that shows lower mass loss (~ 1%) when is heated in the atmosphere with 100% of water vapour (H$_2$/O$_2$). This suggests that the dimensional changes are more related to the type of material, i.e., blanket or module (pyrolog), while the mass loss is more dependent on the composition. On the other hand, as in the previous loop of HTs, the Xtra Pyrolog is the one that shows a higher mass loss, although it has to be considered that 1% of the weight loss is due to the binder removal, so the mass loss related to the material itself is similar to that of the Prime formulation.
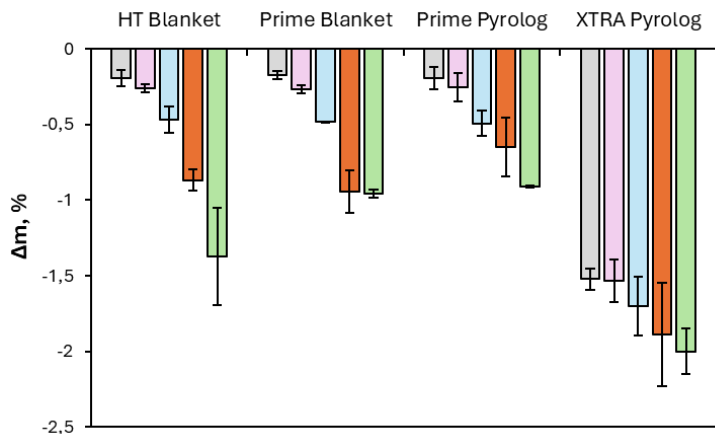
Figure 74. Mass loss of fibre-based materials after HT-48h at different combustion atmospheres. Air in grey, NG/Air in violet, H$_2$/Air in blue, NG/O$_2$ in orange, H$_2$/O$_2$ in green.

The resilience results obtained for the fibre-based materials are represented in Figure 75. Comparing the resilience obtained after HTs with the value of the unfired material (grey stripped columns), it was observed that there is a general decrease in the resilience after HTs regardless the atmosphere used, especially in the pyrolog materials, Prime and Xtra. Taking this into consideration, the loss of resilience has been attributed to the heating treatment itself, rather than the water vapour content of the HT atmosphere.

It should be mentioned that, although there are not differences in the resilience of Xtra Pyrolog as function of the HT atmosphere, it can be stated that the strength of the samples HT-ed in water vapour atmospheres

HYINHEAT

is much lower than the one of the samples HT-ed in air since the first ones exhibit a tendency to crumble upon removal from the testing machine while this behaviour was not observed in the unfired and air-treated samples.
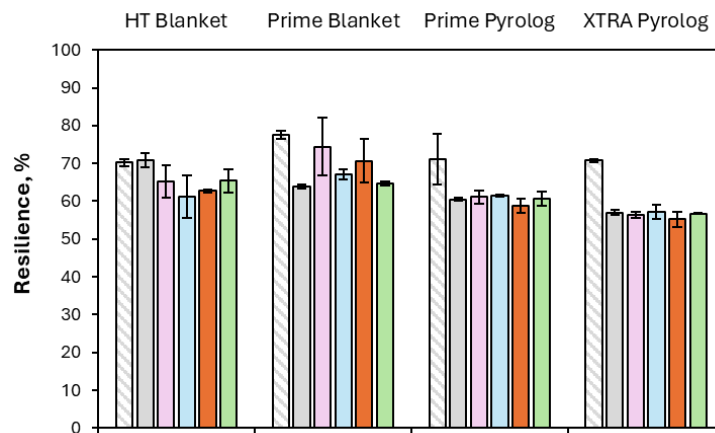
Figure 75. Resilience measurements of fibre-based materials after HT-48h at different combustion atmospheres. Unfired in grey striped, air in grey, NG/Air in violet, H_2/Air in blue, NG/O_2 in orange, H_2/O_2 in green.

Figure 76 shows the apparent density of the fibre-based materials after the HTs performed during 48 h. No significant density variations are observed for any material, apart from the Superwool Prime Pyrolog that suffers a reduction on density when it is heated, especially in air. The lower density of the Prime Pyrolog material after HTs has been attributed to the fact that the unfired material is noticeably softer than after HTs, in comparison to the other materials. Therefore, the initial height measured before the heat treatments is lower than the real one because the sample is compressed during measuring (and consequently the density is higher), resulting in an overestimation of the unfired density.
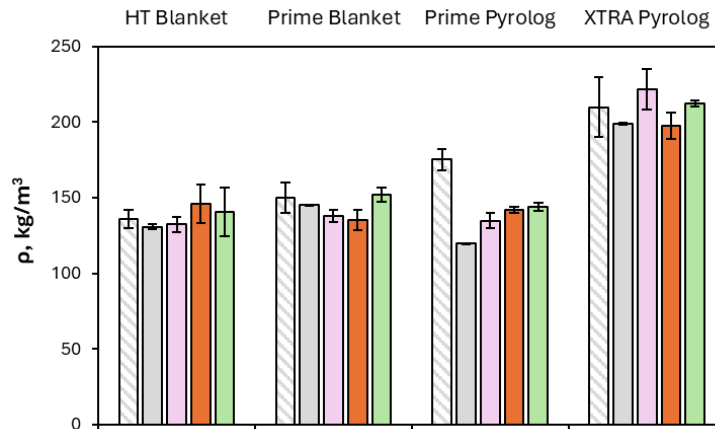
Figure 76. Bulk density measurements of fibre-based materials after HT-48h at different combustion atmospheres. Unfired in grey striped, air in grey, NG/Air in violet, NG/O_2 in orange, H_2/O_2 in green.

The fibre diameter distribution (D10, D50 and D90) of the materials after HTs is presented in Figure 77. The number of fibres measured to determine the fibre diameter distribution of each fibre-based material are shown in Table 25.

These charts indicate that, in general, the diameter of the fibres increases slightly after HTs, regardless the type of atmosphere. Based on these observations, it seems that the main change in fibres diameter is due to the intrinsic crystallization of the materials. Comparing the effect of water vapour on the increase of fibre diameter, no significant changes among the different atmospheres can be detected, despite the increase in fibres roughness with the water vapour content that can be observed in Figure 79, Figure 80 and Figure 81. The only material that shows a slightly increase of fibre diameter with the water vapour content in the HT is the Xtra Pyrolog (Figure 77.d.) but the change is almost negligible.

HYINHEAT
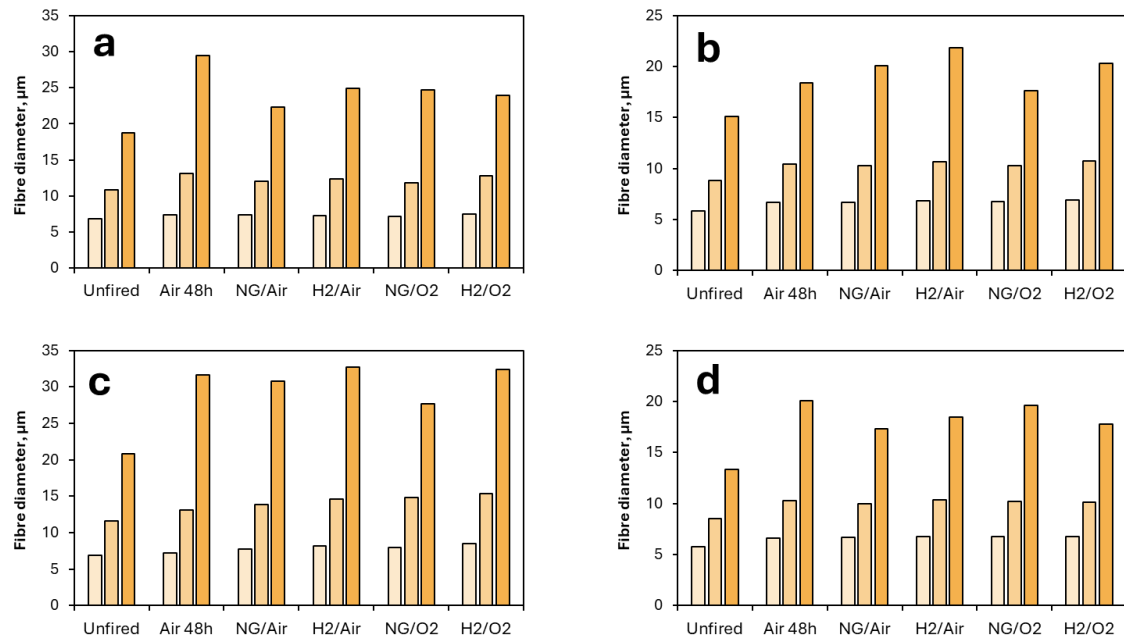
Figure 77. Fibre diameter analysed by dynamic image analysis with QICPIC equipment and VIBRI module. From lightest to darkest D10, D50 and D90; a. HT Blanket; b. Prime Blanket; c. Xtra Pyrolog; d. Prime Pyrolog.

Table 25. Number of fibres measured to determine the fibre diameter distribution of each fibre-based material.

Materials	Number of fibres measured					
	Unfired	Air	NG-Air	H_2-Air	NG-O_2	H_2-O_2
Superwool® HT Blanket	11490	2514	1802	5113	2613	1245
Superwool® Prime Blanket	7282	3222	6708	7380	3300	2206
Superwool® Prime Pyrolog	2379	5485	5203	8352	2337	2093
Superwool® Xtra Pyrolog	1474	4327	5616	7203	1744	680

Figure 78 illustrates the variations in the concentration of the crystallographic phases of each material as a function of water vapour content, quantified from the XRD diffractograms. It can be observed that the content of each phase remains almost constant in the four combustion atmospheres for the Prime Blanket (b), Prime Pyrolog (d) and Xtra Pyrolog materials (c). In contrast, the results show that in the HTs atmospheres with a high-water vapour content, the wollastonite phase is favoured over pseudowollastonite in the case of the HT Blanket (a).

HYINHEAT
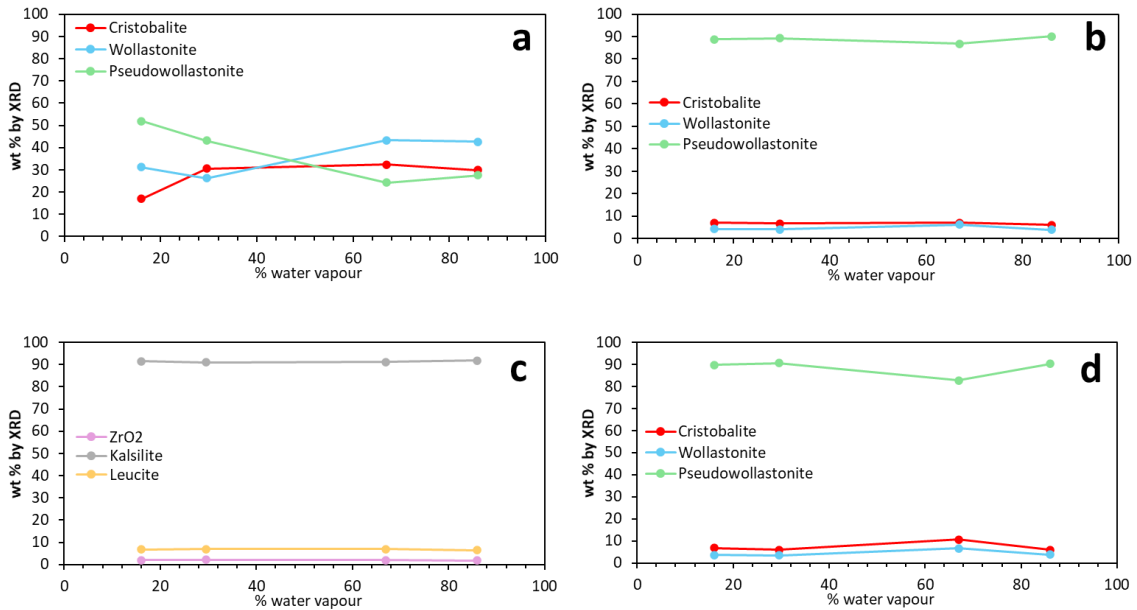
Figure 78. Variation of the crystallographic phases determined by XRD according to the water vapour content in the combustion atmospheres; a. HT Blanket; b. Prime Blanket; c. Xtra Pyrolog; d. Prime Pyrolog.

The microstructure of the HT Blanket, Prime Blanket and Prime Pyrolog material are presented in Figure 79, Figure 80 and Figure 81, respectively. A similar crystallisation pattern to that presented in the results of the HTs performed during 28 h (Figure 68, Figure 69 and Figure 70) can be observed, but in general there is a higher number of fibres with larger grain sizes than those observed after a shorter HT holding time.

The microstructure of the Superwool Xtra Pyrolog material are shown in Figure 82. For this material, a growth of zirconia grain size with water vapour content can be observed clearer than after the shorter HTs (Figure 71).
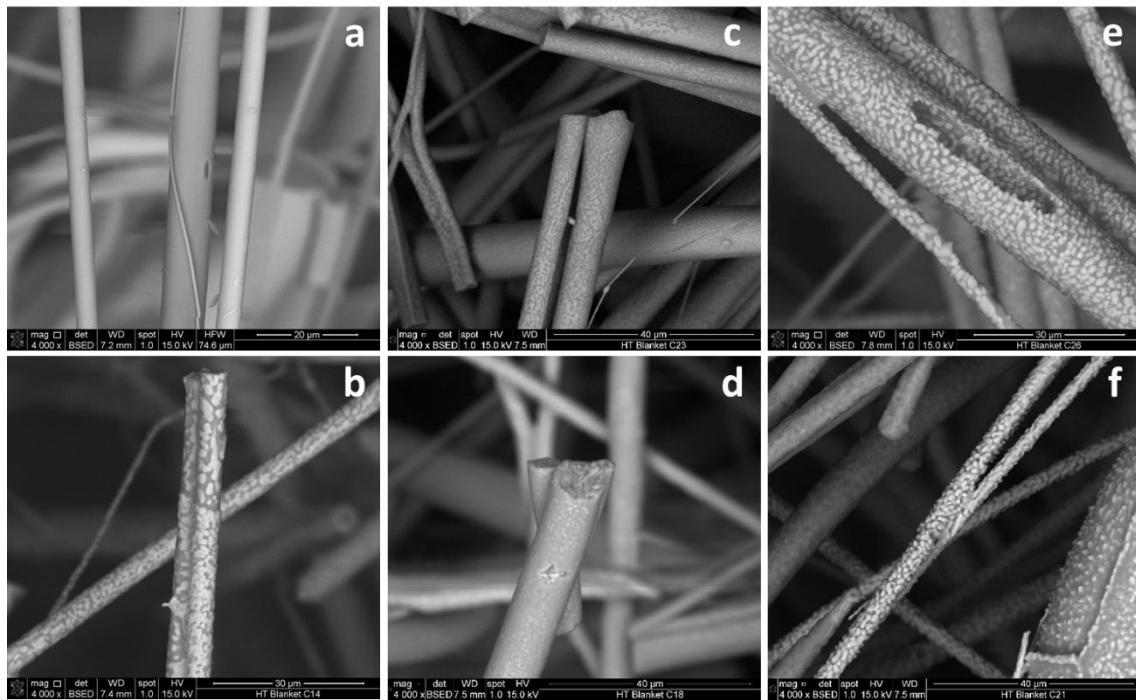
Figure 79. Micrographs of Superwool HT Blanket unfired and after the different heat treatments at 1200 °C – 48 h; a. Unfired, b. Air, c. NG/Air, d. H$_2$/Air, e. NG/O$_2$, f.H$_2$/O$_2$.

HYINHEAT
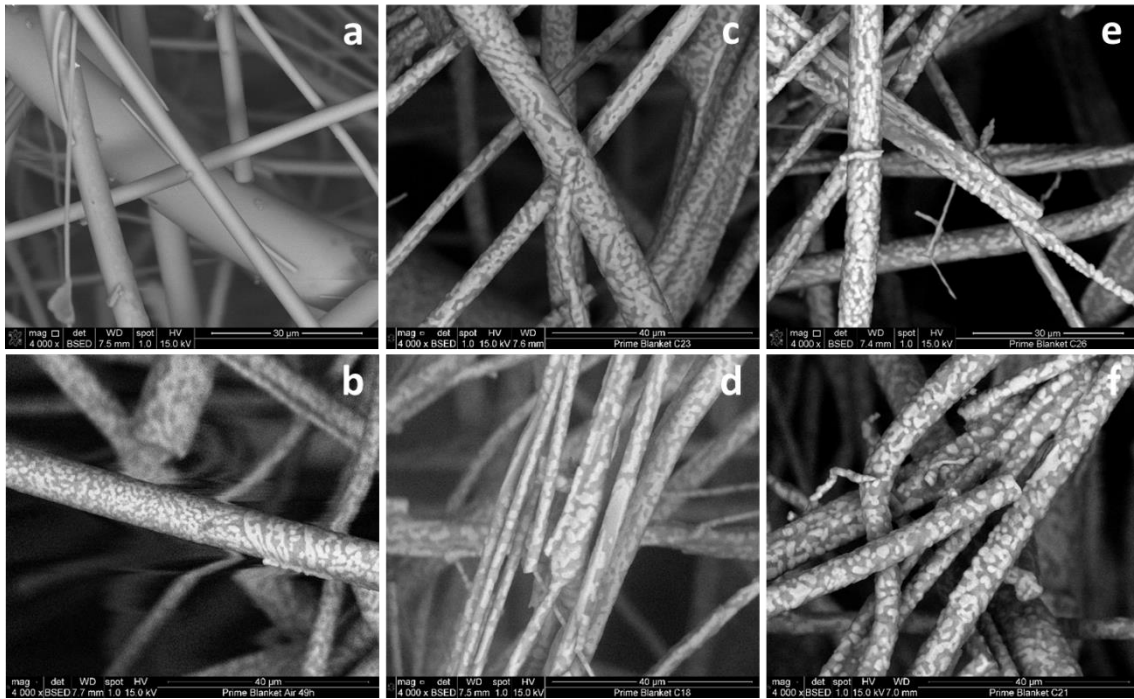
Figure 80. Micrographs of Superwool Prime Blanket unfired and after the different heat treatments at 1200 °C – 48 h: a. Unfired, b. Air, c. NG/Air, d. H₂/Air, e. NG/O₂, f.H₂/O₂.
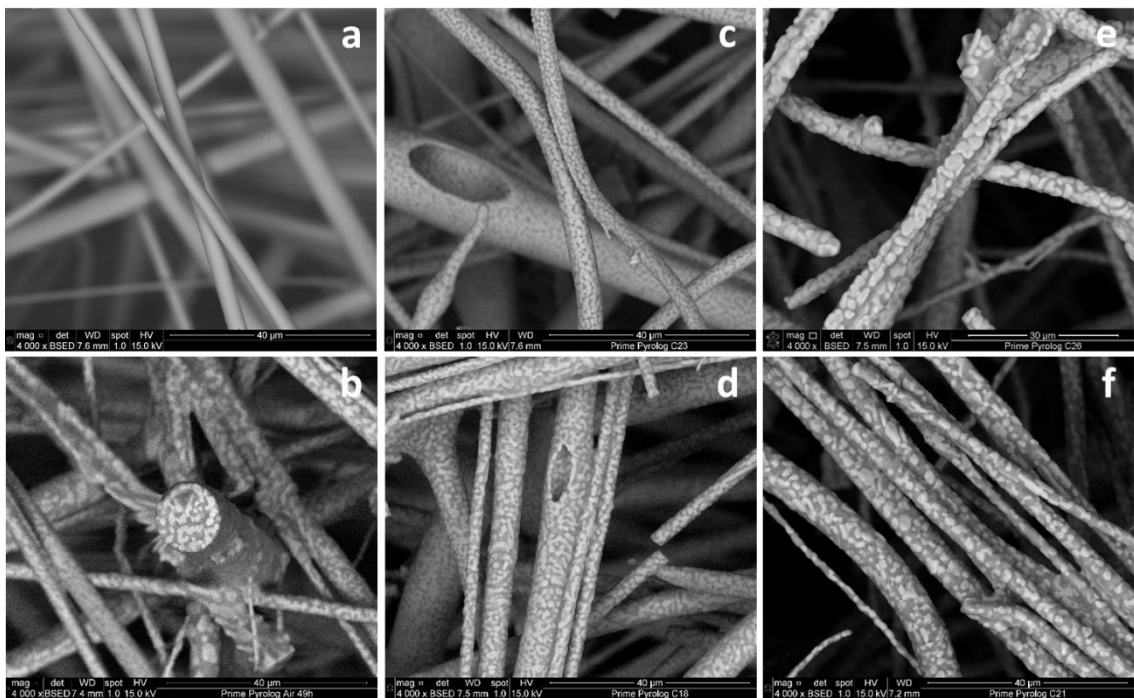
Figure 81. Micrographs of Superwool Prime Pyrolog unfired and after the different heat treatments at 1200 °C – 48 h: a. Unfired, b. Air, c. NG/Air, d. H₂/Air, e. NG/O₂, f.H₂/O₂.

HYINHEAT
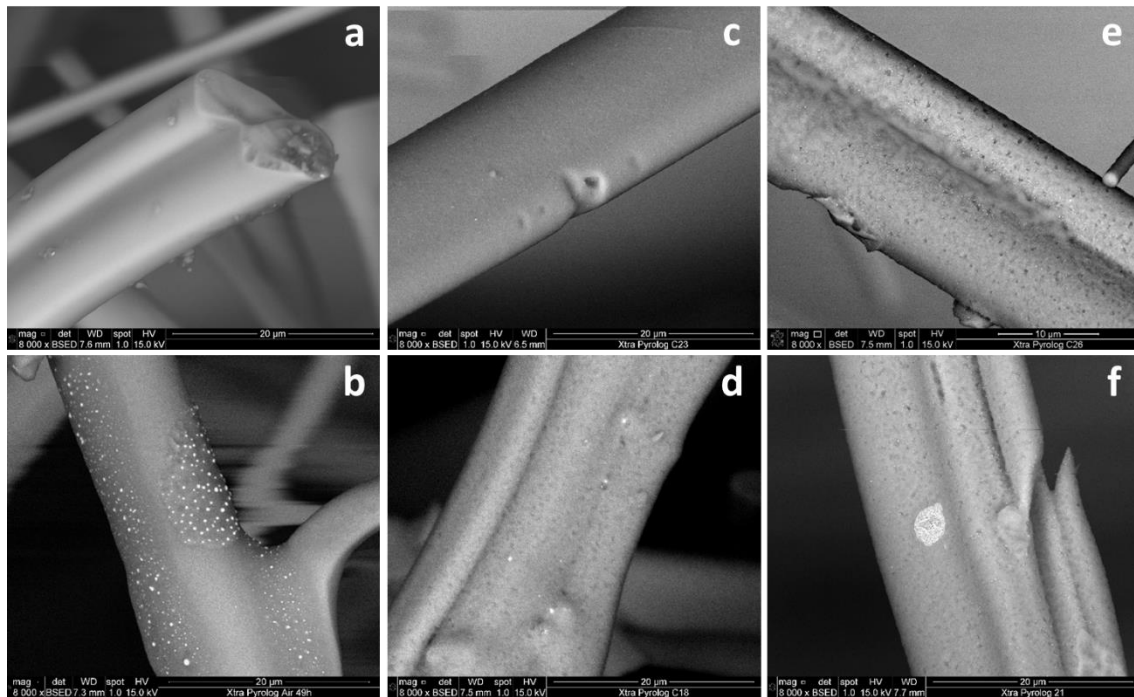
Figure 82. Micrographs of Superwool Xtra Pyrolog unfired and after the different heat treatments at 1200 °C – 48 h: a. Unfired, b. Air, c. NG/Air, d. H₂/Air, e. NG/O₂, f.H₂/O₂.

The composition of the fibre-based materials after the heat treatments of the second loop has been determined by EDS. In general, it has not been found any significant compositional variations as function of the HT atmosphere that explains the higher mass loss determined after the HTs performed in NG/O₂ and H₂/O₂. The composition of the Prime Blanket and Xtra Pyrolog are shown in Table 26 and Table 27 as an example.

Table 26. Compositional analysis of Prime Blanket determined by EDS for each Loop 2 heat treatment.

wt. % by EDS	Unfired	Air	NG-Air	H₂-Air	NG-O₂	H₂-O₂
MgO	0.3	0.1	0.3	0.2	0.2	0.2
Al₂O₃	1.8	0.7	0.7	2.0	1.1	0.9
SiO₂	66.2	62.0	59.5	66.1	59.3	62.0
K₂O	0.3	0.2	0.2	0.2	0.4	0.4
CaO	31.5	37.0	39.2	31.5	39.0	36.5

Table 27. Compositional analysis of Xtra Pyrolog determined by EDS for each Loop 2 heat treatment.

wt. % by EDS	Unfired	Air	NG-Air	H₂-Air	NG-O₂	H₂-O₂
MgO	0.6	0.6	0.8	0.4	0.6	0.4
Al₂O₃	29.6	29.2	30.1	28.2	28.8	29.7
SiO₂	34.0	33.6	33.6	34.7	35.3	32.5
K₂O	28.8	28.5	29.1	29.2	29.0	30.5
ZrO₂	6.9	6.8	6.4	7.2	6.2	6.8

HYINHEAT

E.3.2.2   Effect of pure H₂

In addition to the HTs performed in the atmospheres that arise from the combustion of NG and H₂, HTs in pure H₂ were carried out at the same temperature, 1200 °C, with a holding time of 8 and 24 hours.

The results of the dimensional changes and mass loss are presented in Figure 83 a and b, respectively. The results demonstrate that there is a considerably greater shrinkage in the materials than that observed after the HTs performed in the combustion atmospheres. HT Blanket and Xtra Pyrolog are the ones that suffer higher shrinkage. In contrast, no significant mass loss was observed for HT Blanket, Prime Blanket, and Prime Pyrolog. However, the Xtra Pyrolog loses twice the mass of the air HT and also more than after the HTs in water vapour atmospheres. This suggests that in the presence of H₂, some of the oxides not present in the other fibre-based materials, such as K_2O, are being evaporated.
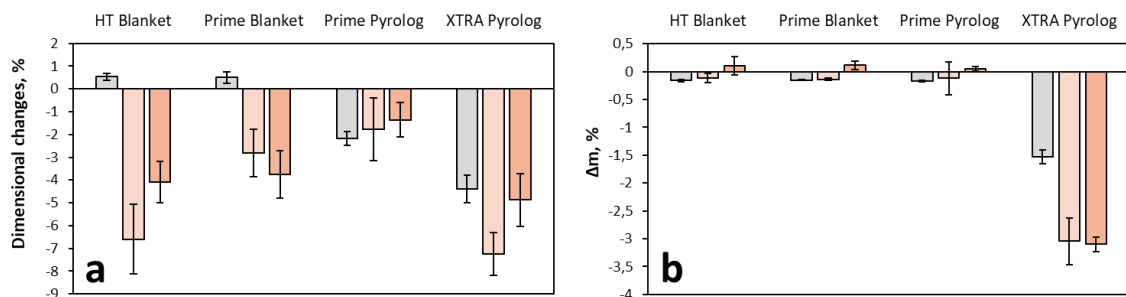
Figure 83. Dimensional changes and mass loss of fibre-based materials after different HTs at 1200 °C; Air 24h in grey, H2 8h in light orange, H2 24h in orange.

The resilience values of the materials after HT in H₂ are presented in Figure 84 where the values of the unfired and air HT-ed samples are also included for comparison. Upon examination of the image, it can be observed that the resilience of the blanket-type materials (HT and Prime) is reduced after being exposed to H₂ during 24 h, while the one of the pyrolog ones remains practically constant with respect to the reference value (HT in air). Additionally, it should be mentioned that contrary to what happens with the Xtra Pyrolog samples that are HT-ed in water vapour atmospheres, after the HT in pure H₂ the sample did not crumble after the resilience test.
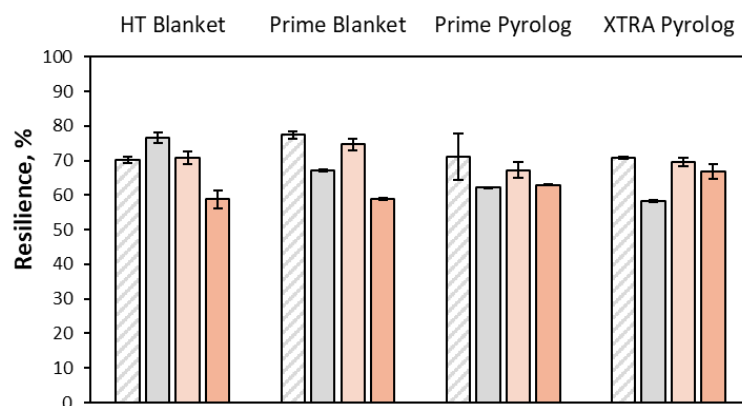
Figure 84 . Resilience measurements of fibre-based materials after different HTs at 1200 °C; Unfired in grey striped, air 24h in grey, H2 8h in light orange, H2 24h in orange.

Figure 85 shows the fibre diameter distribution after the HTs in pure H₂. and in air, as reference. As observed, the fibre diameter remains almost constant after the HTs in H₂ comparing to the values of the air HT-ed samples.

HYINHEAT
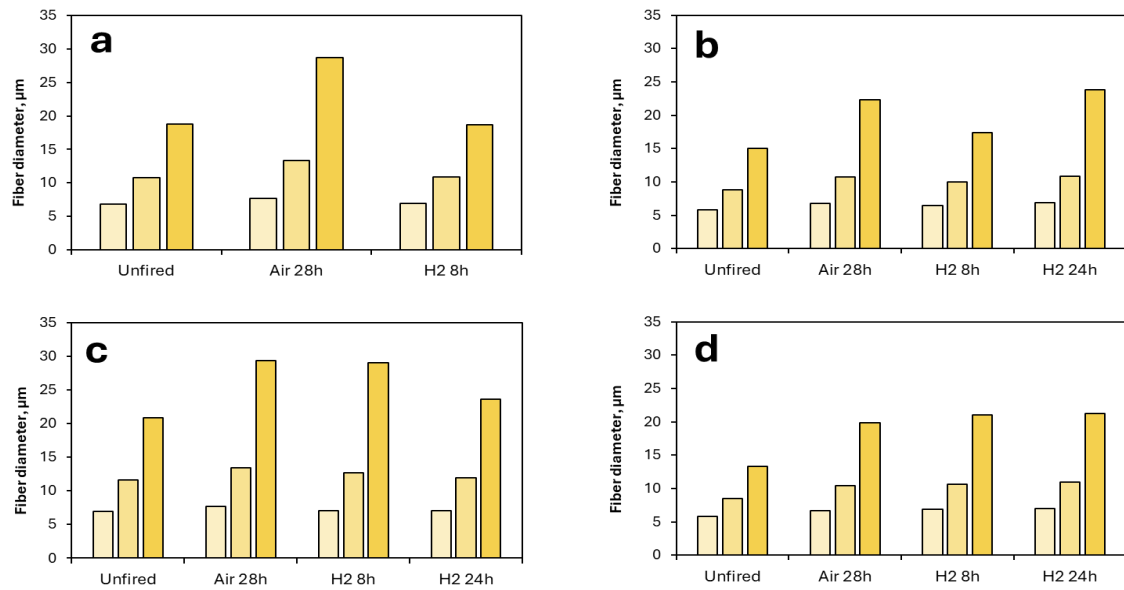
Figure 85. Fibre diameter analysed by dynamic image analysis with QICPIC equipment and VIBRI module of the H₂ HT-ed samples. From lightest to darkest D10, D50 and D90; a. HT Blanket; b. Prime Blanket; c. Xtra Pyrolog; d. Prime Pyrolog.

Figure 86 presents a comparison between the X-ray diffractograms of the fibre-based materials after the HTs in air (black line) and in H₂ (red line) for a 24 h of holding time and the quantification of the phases is shown in Table 28.

For the HT blanket (Figure 86 a) the most noticeable changes are observed in the relative concentration of the crystalline phases. In the diffractograms from the samples HT-ed in H₂ (red line), the intensity of the main cristobalite peak is approximately 50% lower in comparison to the samples HT-ed in air. Additionally, a modification of the relative concentration between wollastonite and pseudowollastonite phases takes place during the HT in pure H₂, being the formation of wollastonite favoured.

On the other hand, the Prime grade materials, both blanket and pyrolog, show no significant changes in the relative concentration of wollastonite and pseudowollastonite and in the amount of cristobalite that crystallize after being exposed to pure H₂

The most relevant changes in the Xtra Pyrolog material are related to the increase in Leucite and the decrease in Kalsilite concentrations when the material is heated in H₂. The change in crystallization patterns might be related to the evaporation of part of the K₂O, which has been confirmed by EDS analysis (Table 28).

Table 28. Quantification based on the X-ray diffractograms of the phases of the materials after HTs in air and in pure H₂ at 1200 °C.

Materials	HT	Wt. %		
		Cristobalite	Wollastonite	Pseudowollastonite
Superwool® HT Blanket	Air-28h	33	34	33
	H₂-24h	3	95	2
Superwool® Prime Blanket	Air-28h	17	79	4
	H₂-24h	12	86	2
		Kalsilite	Leucite	ZrO₂
Superwool® Xtra Pyrolog	Air-28h	96	2	2
	H₂-24h	83	14	3

HYINHEAT
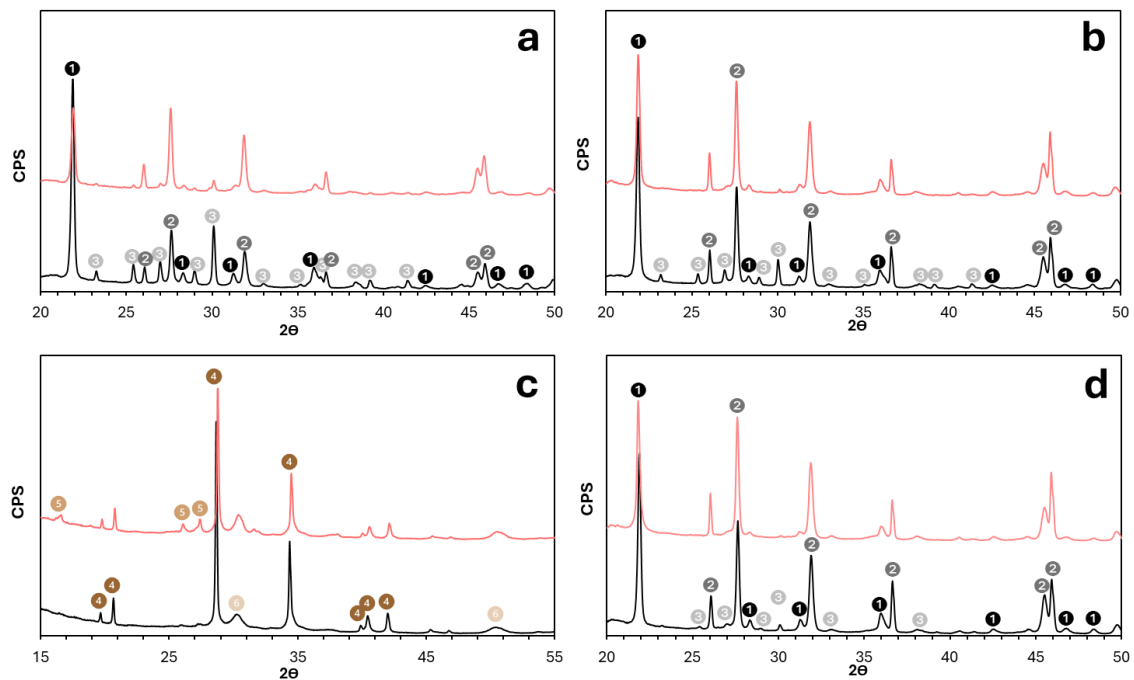
Figure 86. XRD patterns of heat-treated fibre-based materials; a. Superwool HT Blanket; b. Superwool Prime Blanket; c. Superwool Xtra Pyrolog; d. Superwool Prime Pyrolog; 1. Cristobalite (SiO2); 2. Wollastonite (CaSiO3); 3. Pseudowollastonite (CaSiO3); 4. Kalsilite (AlSiKO4); 5. Leucite (AlSi2KO6); 6. Zirconia (ZrO2).

A series of micrographs were taken at different magnifications of the selected materials subjected to different holding times in pure H₂ and heated on air for reference (Figure 87, Figure 88, Figure 89 and Figure 90). Significant differences have been identified in the images of the HT Blanket material (Figure 87) following heat treatment. In the presence of H₂, a different crystallised phases morphology is observed. CaSiO₃ grains appears smaller and shows a distinct morphology with regions of varying grain sizes. Furthermore, after 24 hours of exposure to H₂, some of the fibres exhibited small 'spikes' that could have been formed by vapour deposition (Figure 87.f). However, most of the fibres were found to be more similar in appearance to the Figure 87.d.

A reduction in the grain size of the zirconia component has been identified in the Xtra Pyrolog material. Zirconia crystals (light contrast) can be observed in Figure 90.b and Figure 90.d, which are not so discernible after 24 hours exposure to H₂, though they can be identified with greater magnification. Moreover, XRD and EDS analyses do not show significant decreases of ZrO₂.

HYINHEAT
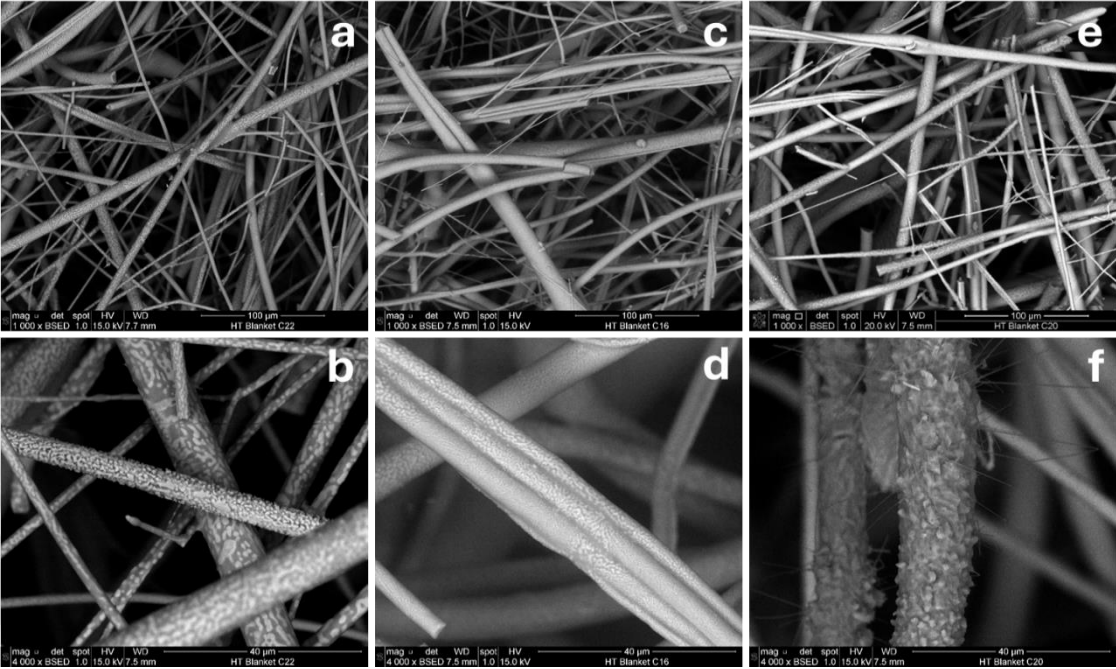
Figure 87. Micrographs of Superwool HT Blanket after the different heat treatments at 1200 °C; a-b. Air 24h; c-d. H2 8h; e-f. H2 24h
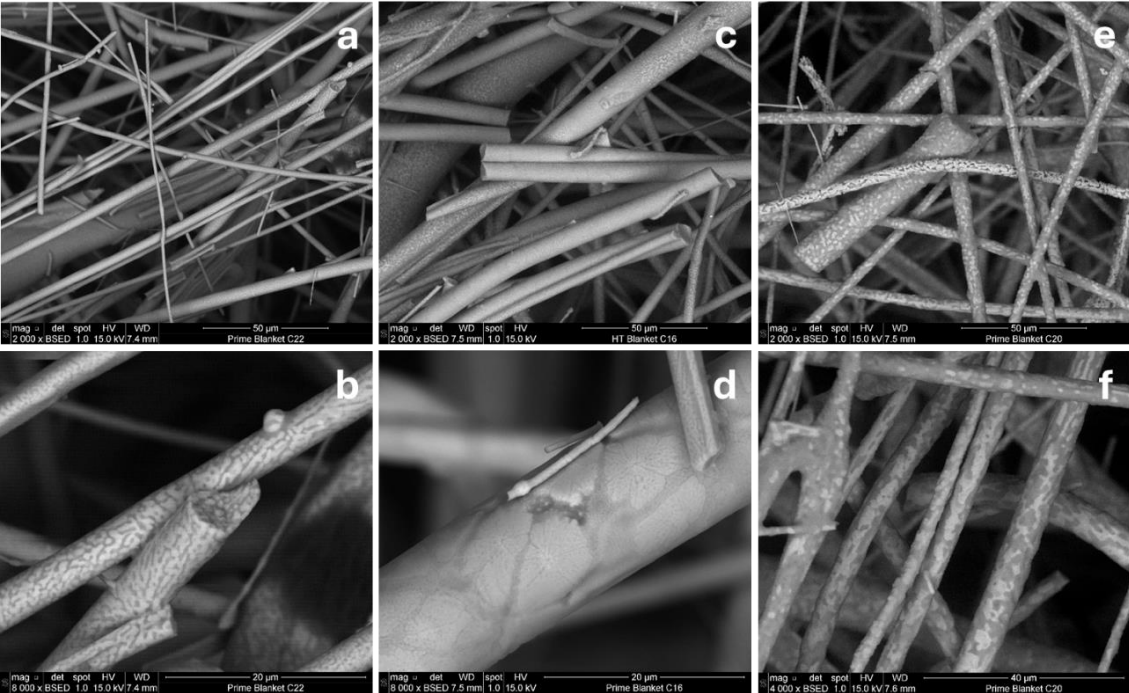
Figure 88. Micrographs of Superwool Prime Blanket after the different heat treatments at 1200 °C; a-b. Air 24h; c-d. H2 8h; e-f. H2 24h

HYINHEAT
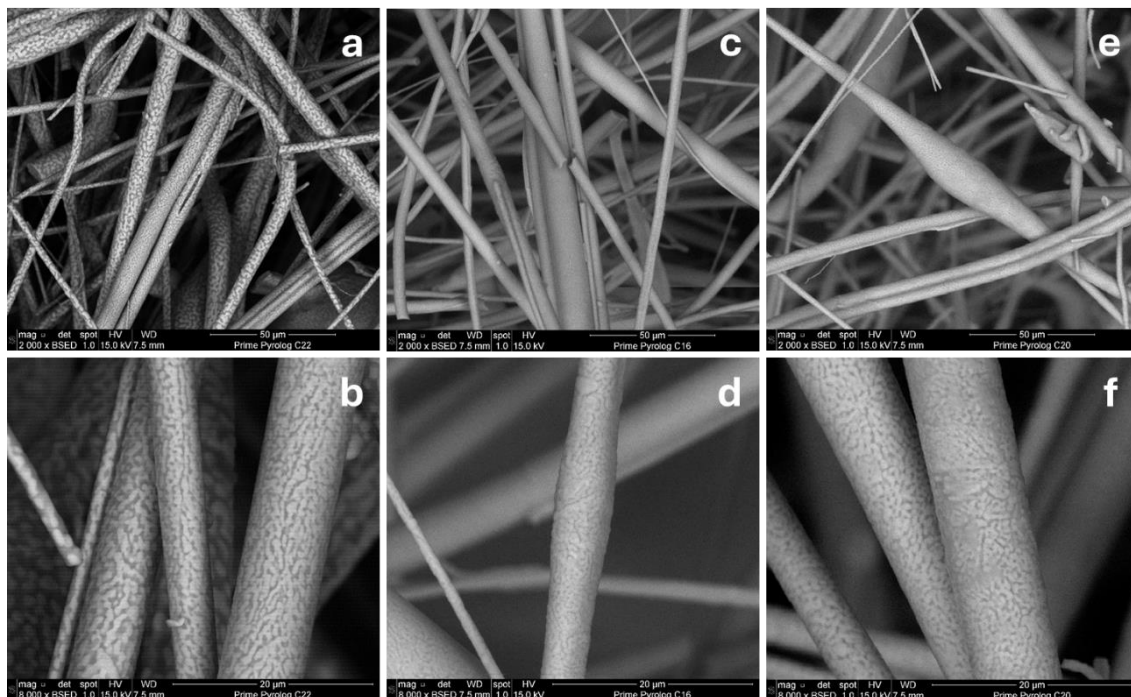
Figure 89. Micrographs of Superwool Prime Pyrolog after the different heat treatments at 1200 °C; a-b. Air 24h; c-d. H2 8h; e-f. H2 24h
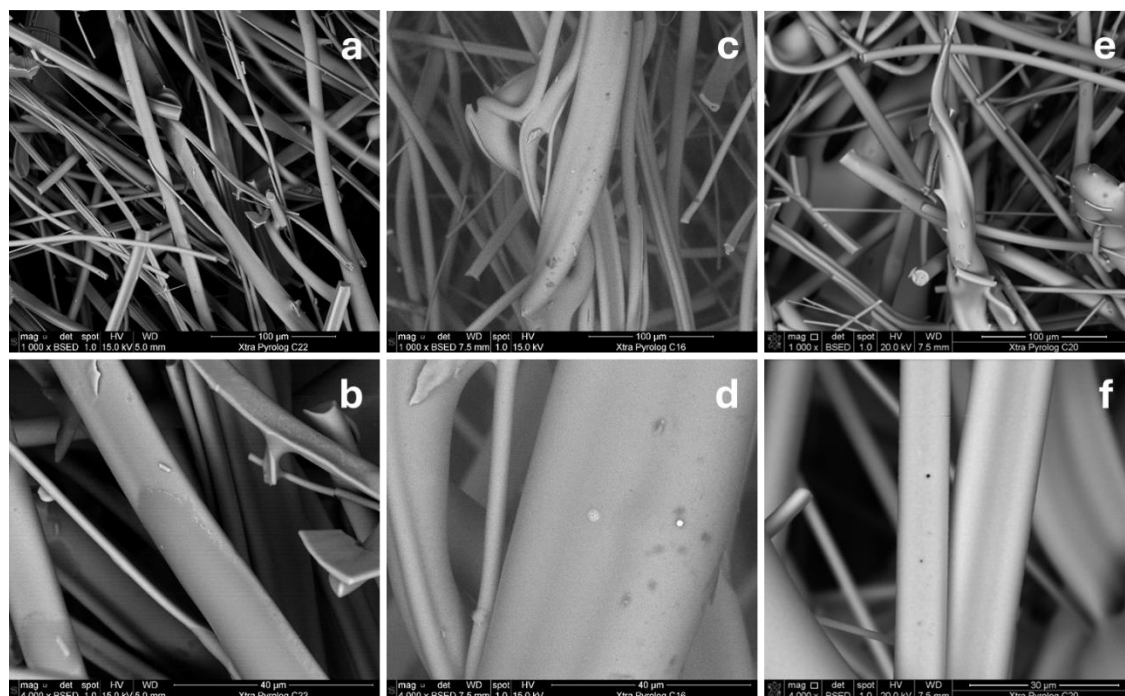
Figure 90. Micrographs of Superwool Xtra Pyrolog after the different heat treatments at 1200 °C; a-b. Air 24h; c-d. H2 8h; e-f. H2 24h

As in previous HTs, there are not noticeable differences in the oxides composition, determined by EDS, of the HT Blanket, Prime Blanket and Pyrolog materials after the HT in pure H_2. However, contrary to what has been seen after HTs in water vapour atmospheres, in the case of the Xtra Pyrolog a reduction in the K_2O has been detected by EDS (Table 29) which is in line with the higher mass loss measured on this material after being exposed to H_2 (Figure 83).

HYINHEAT

Table 29. Compositional analysis of Xtra Pyrolog determined by EDS for each heat treatment.

wt. % by EDS	MgO	Al_2O_3	SiO_2	K_2O	ZrO_2
Air 24 h	0.6	29.9	33.0	29.5	6.9
H_2 8 h	0.4	29.0	35.0	28.0	7.1
H_2 24 h	0.3	30.8	36.4	25.7	6.3

E.3.3 Heat treatments on refractory bricks

To evaluate the behaviour of refractory brick in the atmospheres that arise from the combustion of NG and H_2 with air and O_2, different HTs have been performed at 1250 °C for 48 hours following the same procedure than for the fibre-based materials.

E.3.3.1 Effect of water vapour atmospheres

The mass loss and dimensional changes of the bricks after the HTs in water vapour atmospheres are shown in Figure 91. In general, the three materials experiment a higher mass loss when they are exposed to higher water vapour content atmospheres (NG/O_2 and H_2/O_2), being this more noticeable in the brick JM23, which is the formulation with lower amount of Al_2O_3.

Regarding the dimensional variations, changes in heigh (Figure 91.b), length (Figure 91.c) and width (Figure 91.d) have been measured. As expected, the only materials than shows significant differences after HTs is the brick JM23 due to its lower classification temperature, 1260 °C comparing to 1540 and 1650 °C of JM28 and JM30, respectively. These last two materials are design to be able to stand higher temperatures and for that, they do not show any shrinkage after the HTs performed at 1200 °C. In any case, the material JM23 does not present significant dimensional changes as function of the HT atmosphere which suggest that the water vapour, at least during the holding time tested (48 h), does not affect the stability of this material.
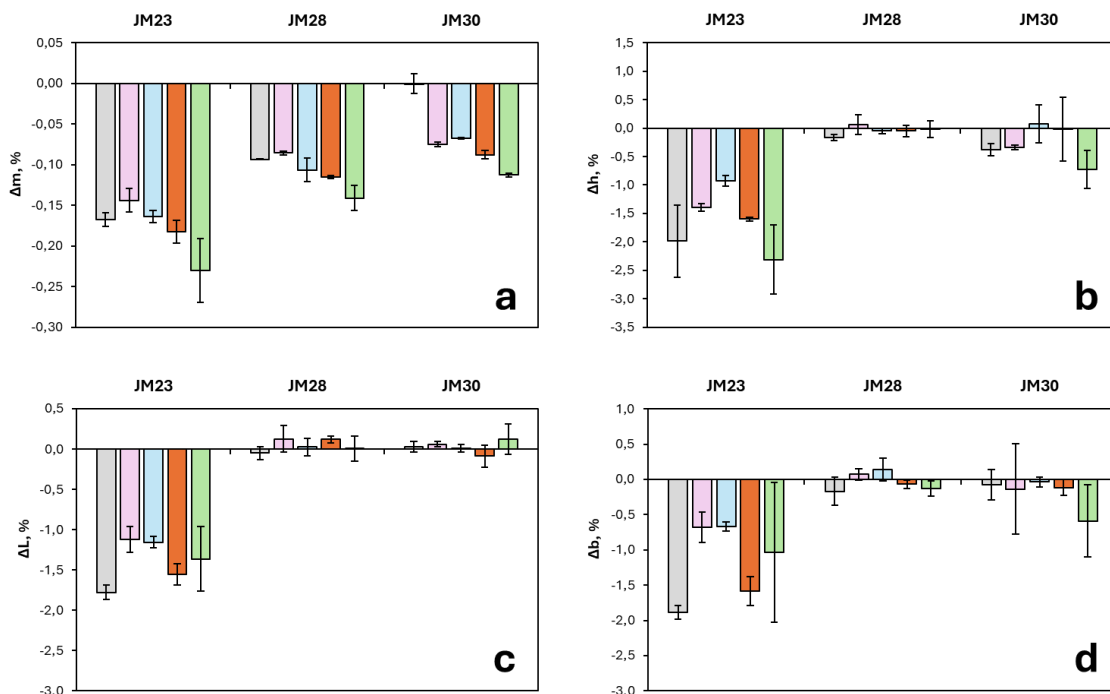
Figure 91. a. Mass loss; b. variations in height; c. variations in length; d. variations in width of the refractory bricks JM23, JM28 and JM3 after HTs in NG/Air (violet), H_2/Air (blue), NG/O_2 (orange), H_2/O_2 (green).

HYINHEAT

Bulk density (Figure 92.b), and apparent porosity (Figure 92.c) were determined for the refractory bricks and slight variations were observed after HT. In the case of JM23, a slight increase in its bulk density with respect to the initial value can be seen, as a result of a decrease in skeletal density and apparent porosity. Brick JM28 shows a decrease in its bulk and skeletal densities with respect to the untreated material. For brick JM30, its bulk density remains approximately constant, although a decrease in its skeletal density and apparent porosity has been observed. However, it seems that these changes occur independently of the atmosphere used.
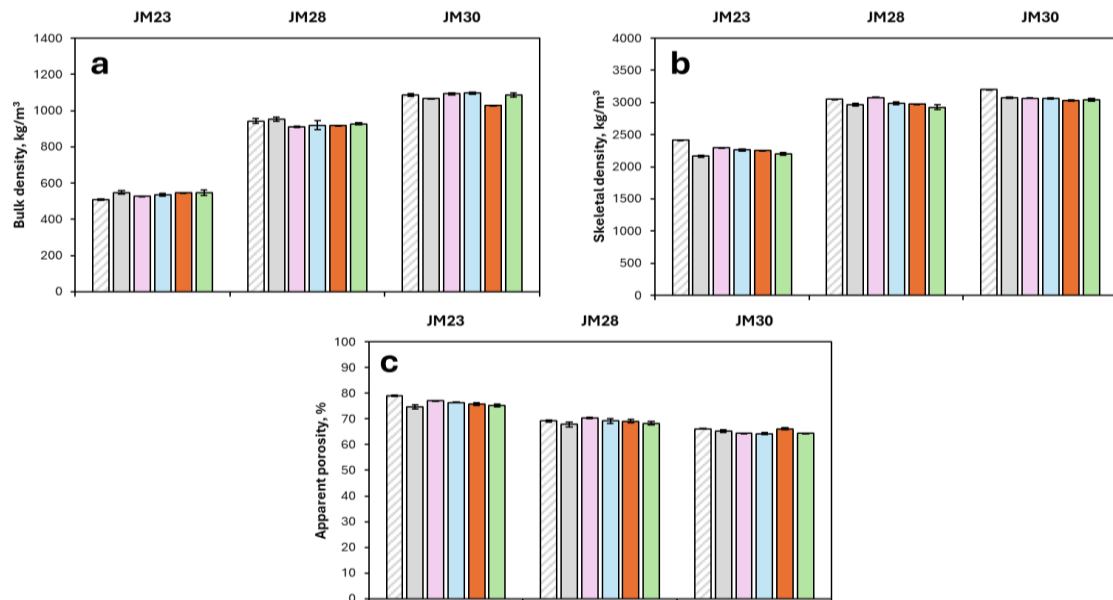
Figure 92. Density measurements of JM bricks after HT; a. Bulk density, b. skeletal density; c. open porosity of refractory bricks JM23, JM28 and JM30. Unfired in striped grey, air in grey, NG/Air in violet, H₂/Air in blue, NG/O₂ in orange, H₂/O₂ in green.

The mechanical strength (MOR), measured by means of three-point bending test, of the three bricks after HTs is represented in Figure 93, values of the unfired and air heat-treated materials are included for comparison. Values obtained are in line with those of the data sheet in the unfired samples, however there are not significant changes after HT and any tendency with the HT atmosphere cannot be drawn. The higher deviation in the measurements of the JM28 and JM30 has been attributed to the higher particle size of these bricks, that can be seen in the micrographs of the Figure 95 and Figure 96.
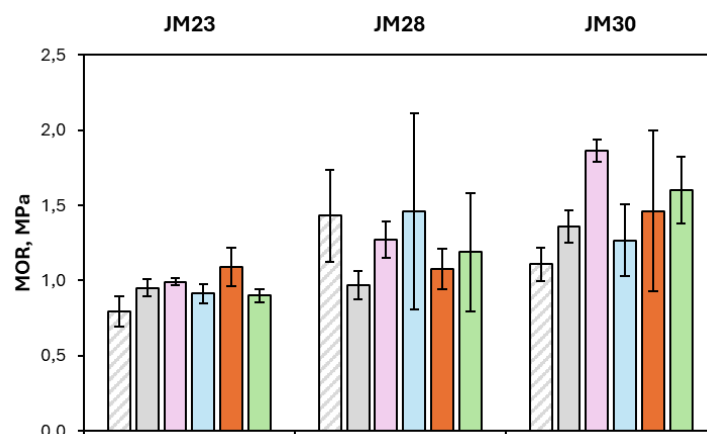
Figure 93. MOR of refractory bricks JM23, JM28 and JM30. Unfired in striped grey, air in grey, NG/Air in violet, H₂/Air in blue, NG/O₂ in orange, H₂/O₂ in green.

HYINHEAT

A series of micrographs of the selected materials subjected to different combustion atmospheres were taken at different magnifications. The microstructure of JM23, JM28 and JM30 are presented in Figure 94, Figure 95 and Figure 96, respectively.
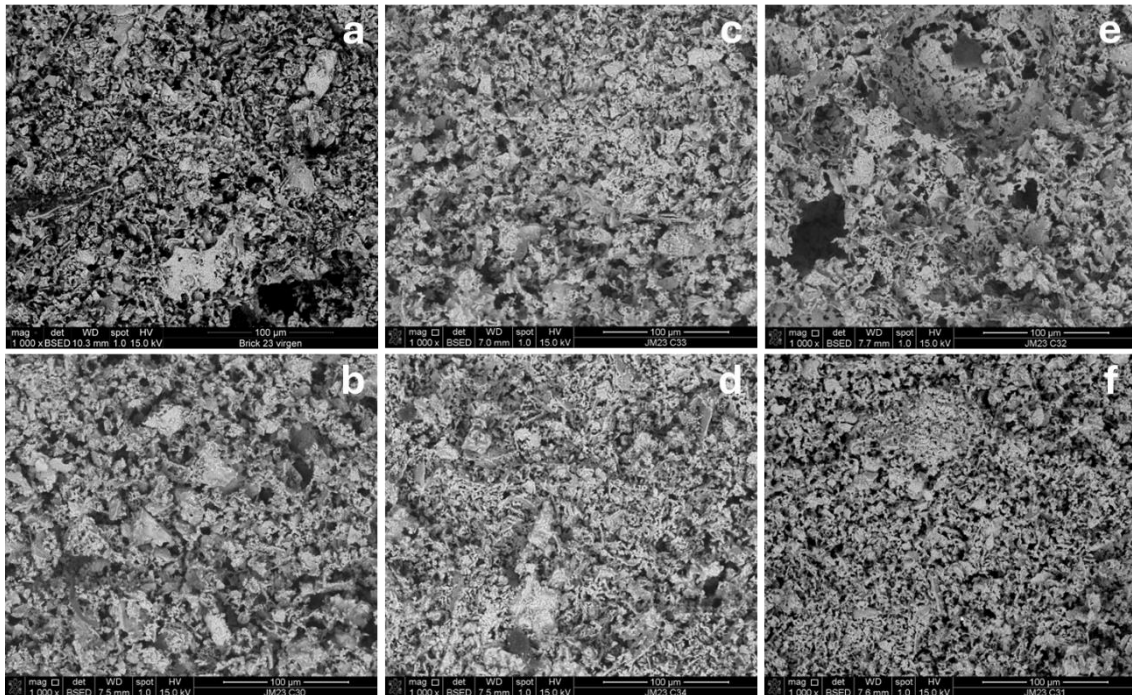
Figure 94. Micrographs of JM23 unfired and after the different heat treatments at 1250 °C - 48h; a. Unfired, b. Air, c. NG/Air, d. H_2/Air, e. NG/O_2, f.H_2/O_2.
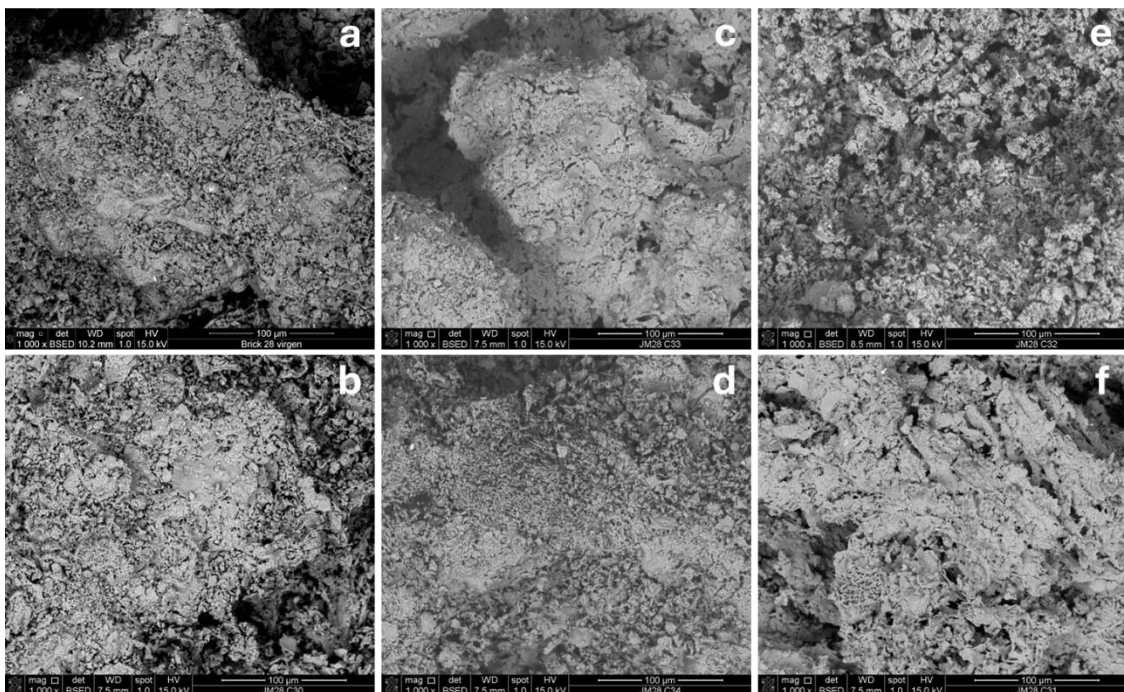
Figure 95. Micrographs of JM28 unfired and after the different heat treatments at 1250 °C - 48h; a. Unfired, b. Air, c. NG/Air, d. H_2/Air, e. NG/O_2, f.H_2/O_2.

HYINHEAT
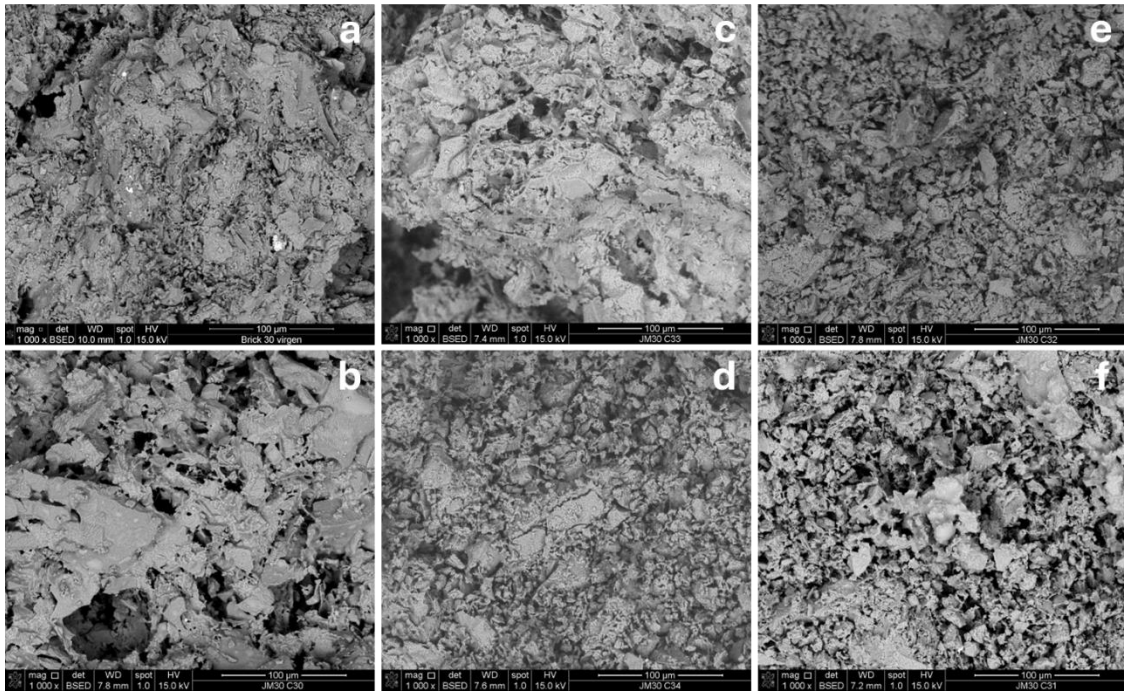
Figure 96. Micrographs of JM30 unfired and after the different heat treatments at 1250 °C - 48h; a. Unfired, b. Air, c. NG/Air, d. H₂/Air, e. NG/O₂, f.H₂/O₂.

No discernible alterations were observed in the microstructure of the materials after HTs. Upon semi-quantitative analysis of the composition by EDS, no compositional modifications were identified in comparison to those presented in Table 23. For that, these tables have not been included in this report.

Quantification based on the X-ray diffractograms of the phases of JM23 (Table 30), JM28 (
Table 31) and JM30 (
Table 32) after the different HTs des not show significative differences, except for JM30, in which a slight increase in the mullite content is taken place in all the HTs applied, but independently of the type of atmosphere.

Table 30. Compositional analysis of JM23 determined by XRD for each heat treatment.

wt. % by XRD	Unfired	Air	NG-Air	H₂-Air	NG-O₂	H₂-O₂
Anorthite	90.5	91.9	91.4	91.6	91.6	91.6
Mullite	9.5	8.1	8.6	8.4	8.4	8.4

Table 31. Compositional analysis of JM28 determined by XRD for each heat treatment.

wt. % by XRD	Unfired	Air	NG-Air	H₂-Air	NG-O₂	H₂-O₂
Mullite	67.1	68.5	69.7	65.2	70.0	71.2
Corundum	32.9	31.5	30.3	34.8	30.0	28.8

Table 32. Compositional analysis of JM30 determined by XRD for each heat treatment.

wt. % by XRD	Unfired	Air	NG-Air	H₂-Air	NG-O₂	H₂-O₂
Mullite	55.0	59.3	62.6	60.0	61.2	61.2
Corundum	44.9	40.6	37.4	40.0	38.8	38.5
Quartz	0.5	0.1	-	-	-	0.3

HYINHEAT

E.4 Conclusions

Several conclusions could be drawn from the laboratory HTs performed at the different atmospheres arisen from the air or oxy-combustion of NG or H$_2$, and algo in pure H$_2$, and the correspondent characterisations (physical, mechanical properties and microstructural changes) carried out, both in fibre-based and bricks insulation materials used as linings in reheating furnaces for steel production.

Combustion atmospheres:

In general terms, no dramatic changes in the properties of all the materials tested as function of the water vapour content in the HT atmosphere have been found at the temperature and time tested. The main conclusions extracted from these HTs are the following:

- Mass loss increases as water vapour content increases in the combustion atmosphere in all the materials, being the Prime formulation the one that shows lower mass loss.
- There is no influence of the different combustion atmospheres on the physical properties (volume shrinkage and density).
- As a consequence of the heat treatments, the fibre diameter increases in all the fibre-based grades tested, but it does not depend on the water vapour content.
- The resilience of the materials decreases in all the cases regardless the atmosphere used.
- Minor microstructural changes have been observed. An increase in fibre roughness was identified in the Superwool HT Blanket and Superwool Prime (both blanket and Pyrolog) when they are HT-ed in high vapour content atmospheres. Similar fibre crystallization behaviour has also been shown in all the atmospheres tested, except some changes in the relative content of wollastonite/pseudowollastonite in HT Blanket for high water vapour content atmospheres.
- Xtra Pyrolog is the most sensitive material to the combustion atmospheres. In spite of the minor differences found in the general properties, a brittleness behaviour has been observed after the resilience tests in the samples heat-treated under combustion atmospheres (regardless the % of water vapour content), which is not observed in the air heat-treated samples.
- For bricks, the three grades tested show a slightly increase in mass loss with the water vapour content in the HT atmospheres, but in all the cases these losses are negligible. Only JM23 suffers from shrinkage after HTs, regardless the atmosphere used, which in line with its classification temperature (1260 °C). To observe a significant change in the behaviour of refractory bricks JM23, JM28 and JM30 the application of HT at higher temperature or longer holding time would be necessary.

Pure H$_2$ Heat Treatments:

In general, the behaviour of the materials when they are heated in pure H$_2$ is different from that in the combustion atmospheres.

- All the fibre-based materials tested suffer from higher shrinkage when they are HT-ed in pure H$_2$,
- The mass loss of the HT and Prime formulations is negligible while the Superwool Xtra Pyrolog shows a higher mass loss than that correspond to HT in air and combustion atmospheres due to the evaporation of K$_2$O in H$_2$.
- Except for the Prime formulation, there is a change in the crystallization way of the fibres when they are HT-ed in H$_2$. The crystallization of the cristobalite is hindered in the case of HT Blanket and the reduction of the K$_2$O in the Xtra Pyrolog leads to an increase in the Leucite phase.
- A higher reduction in resilience of fibres takes place in the HT and Prime blanket, comparing with the combustion and air atmospheres. In general, a hardening effect was observed in all materials, but particularly in Superwool Xtra Pyrolog after 24 hours of exposure to H$_2$, although in this case, no embrittlement behaviour has been observed.

Comparing all the materials fibre-based material tested, the Prime formulation is the one that shows higher stability in the presence of high-water vapour atmospheres and also in the presence of pure H$_2$ while the most sensitive material seems to be the Xtra Pyrolog, that became very fragile when it is heated in presence of water vapour (combustion atmospheres) and suffer a high mass loss in H$_2$ rich environments due to the partial evaporation of one of its constituents (K$_2$O).

HYINHEAT

F. Impact of H₂ heating on steel quality: Analysis and Solution

F.1 Overview

In recent years, technological developments and innovations that have involved the steel and iron and steel industry in general have been mainly dictated by increasingly complex and challenging requests from steel producers or end users.

The use of semi-products or steel products, from common to special ones, is traditionally governed by extremely stringent and rigorous requirements in terms of metallurgical and mechanical characteristics, to guarantee the quality of the final product.

During the heating process that takes place in a rolling furnace for flat and long products, various physical-chemical phenomena take place: fundamental are those responsible for the alteration of the mechanical and metallurgical characteristics of the metal surface.

These are the oxidation and decarburization reactions, i.e. the chemical-physical alteration of the surface layer of the metal, governed by the environmental conditions typical of industrial furnaces (long residence times at high temperatures, in an oxidizing or reducing environment): the reactions are chemically controlled by the diffusion of oxygen and carbon at high temperatures and by the chemical equilibrium of the various species involved in the mechanisms.

DAN, a world leader in the construction of systems for heating and heat treatment of carbon, micro/high alloy and stainless steels, has over the years analyzed the mechanism of oxidation and decarburization kinetics.

Considering the actual global demands of furnaces ready for Hydrogen combustion, DAN has already deeply evaluated the impact of Hydrogen combustion on those chemical phenomena with a particular focus on the Scale Formation.
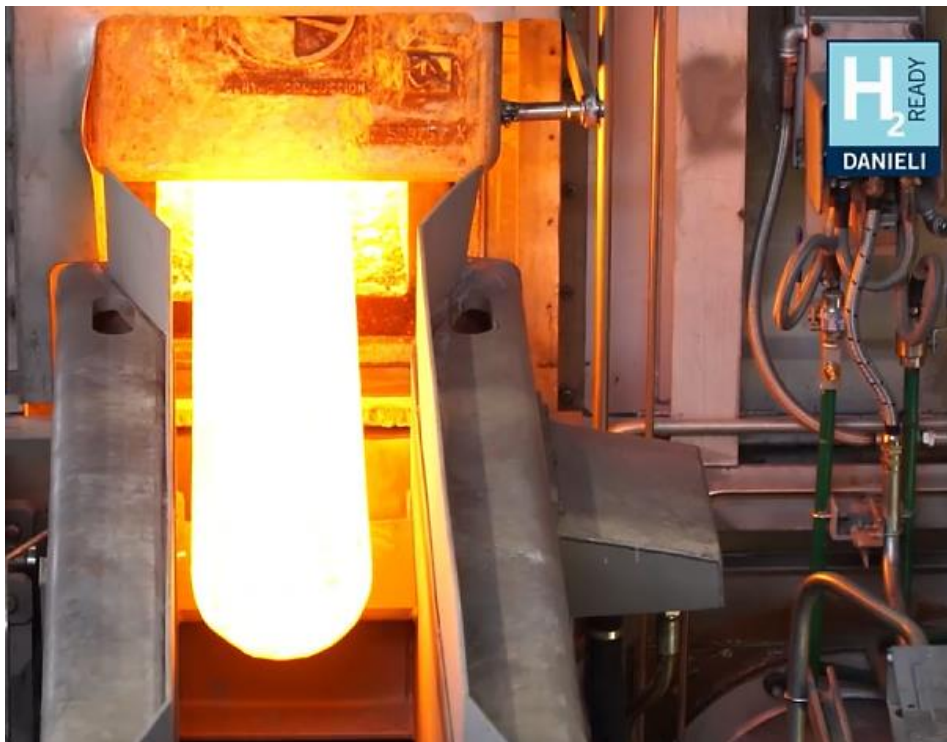
Figure 97 - Discharing of DAN's scale free furnace

HYINHEAT

Impact of H₂ heating on product quality, yield, and refractory

F.1.1 General scale formation concept

During the heating of a metal charge, the following occurs simultaneously:

- the superficial impoverishment of carbon to the metallic state (Fe_3C) by oxygen, which is called "decarburization"
- oxidation of iron, which is visually perceptible as the formation of a surface scale -so called "scale formation"

The oxidation of iron and carbon occurs following complicated chemical kinetics since in contact with the metal composed of different percentages of Fe, C and micro-alloys such as Ni, Mn, Mo, Si, Cu, Cr, the combustion products consisting of CO, CO_2, H_2, H_2O and O_2 are found.

The oxidation process as a whole will produce a very complex oxide according to the chemical composition of the steel, resulting from the combination of the various simple oxides, and which will influence the extent and porosity of the scale.

During a heating process of a steel for final rolling or annealing to modify the mechanical or structural characteristics of the steel itself, the following are defined:

- decarburization as impoverishment of the surface layers of the steel with a reduction in the weight of the material
- oxidation as oxygen enrichment of the surface layers of the steel with an increase in the weight of the material

The heating or heat treatment process of steel is characterized by the simultaneous development of three main phenomena:

- reactions between the furnace gases,
- interaction between the combustion products and the metal surface,
- diffusion within the metal.

The elementary reactions that at the surface-combustion products contact level govern the mechanisms of decarburization and oxidation of iron can be summarized as follows:

$$2\,Fe + O_2 \leftrightarrow 2\,FeO$$

$$4\,Fe + 3\,O_2 \leftrightarrow 2\,Fe_2O_3 \qquad \text{Oxidation} (\rightarrow)$$

$$3\,Fe + 2\,O_2 \leftrightarrow Fe_3O_4$$

$$2\,Fe_3C + O_2 \leftrightarrow 6\,Fe + 2\,CO$$

$$Fe_3C + 2\,H_2 \leftrightarrow 3\,Fe + CH_4 \quad \text{Decarburization} (\rightarrow)$$

$$Fe_3C + CO_2 \leftrightarrow 3\,Fe + 2\,CO$$
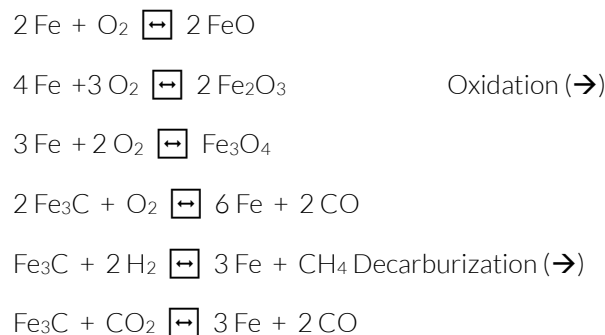
The result of these reactions is represented, especially above the austenitization temperature (≈ 910°C), by a considerable loss of carbon and iron from the body of the metal charge, elements which are partly found in the scale and partly migrate into the fumes.

HYINHEAT

F.2   Scale growth model development

F.2.1   Target

DAN is always focused on continuous improvement of the newest green technologies.

Hydrogen combustion is a green option to the traditional fossil based fuels for steel furnace. A fundamental aspect to be analyzed is that Hydrogen combustion shall guarantee proper heating quality and the product properties. For this reason, the needs of a dedicated research project grew up in order to study the scale phenomena in new, different furnace atmospheres created by Hydrogen Combustion.

In 2022 DAN Research Center started the development of a new proprietary scale prediction model based on experimental results. The aim of the work is the development of a kinetic model able to predict, quantitatively, the growth of scale thickness within several different atmospheres and conditions. The planned activities will also give a series of semi-quantitative indications regarding the influence of oxidation conditions on the scale morphology and its attitude to a good descaling behaviour.

From the industrial point of view, the control of scaling conditions during heating could be important for the optimization of steel loss and the improvement of the surface quality.

The above results can be exploited to improve the operating conditions of combustion furnaces and for the design of the heating atmosphere in the case of fully hydrogen combustion.

Following section will shortly summarize the research project and its results.
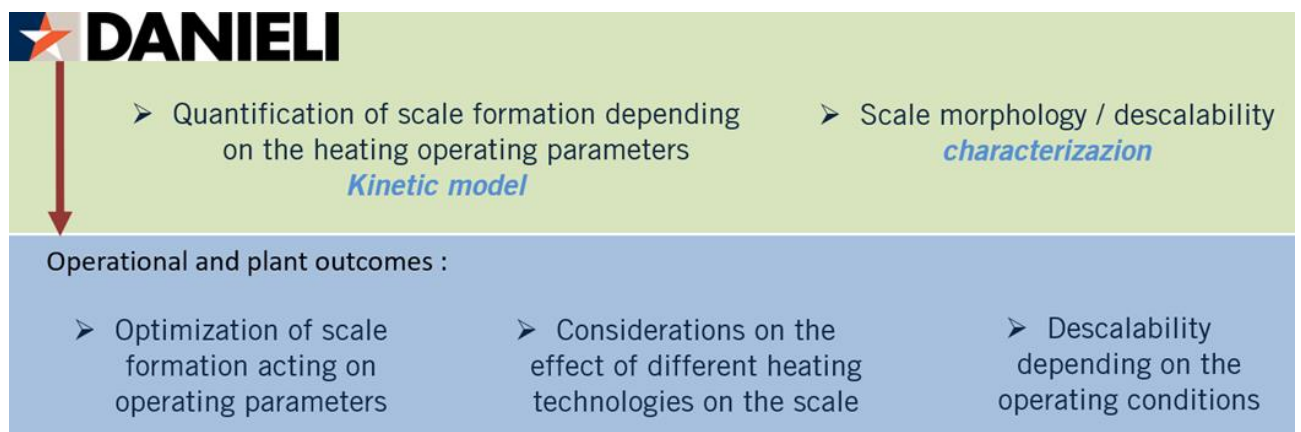
Figure 98 - Targets of the research

F.2.2 Work Description

Considering the difficulty in monitoring the growth of the scale in the plant, it was decided to recreate the heating process on a laboratory scale, working on small samples obtained from the slab " as cast " in a tubular furnace equipped to control and vary the process conditions.

The samples are subjected to different oxidation conditions and different combinations of temperature, time, concentration of oxidizing gases such as oxygen and vapor.

The oxidized samples are characterized via microscopy in order to measure the thickness of the scale and other qualitative characteristics (porosity, presence of melted phases, homogeneity) and by means of some mechanical tests, which will give indications regarding the adhesion of the generated scale.

The data collected are used into a kinetic model of scale growth, first attempt, which will need to be calibrated in the plant.

The kinetic model of the scale growth is based on the widely accepted Wagner theory and describes the scale growth in function of temperature, time, oxygen and water vapour concentration.

The main activities can be summarized as:

1. Collection, transport of materials from plant
2. Preparation of samples for the laboratory experimental activity
3. Oxidation test of samples in the tubular furnace
4. Surface characterization of the samples
5. Build of a database of experimental data from literature (steel scale growth)
6. Elaboration of a kinetic model with literature data
7. Refining of the kinetic model with the experimental parameters
8. Evaluation of the oxidation conditions on the qualitative aspects of scale and steel
9. Application of the model in predictive mode, for the estimation of the scale thickness for different heating profiles
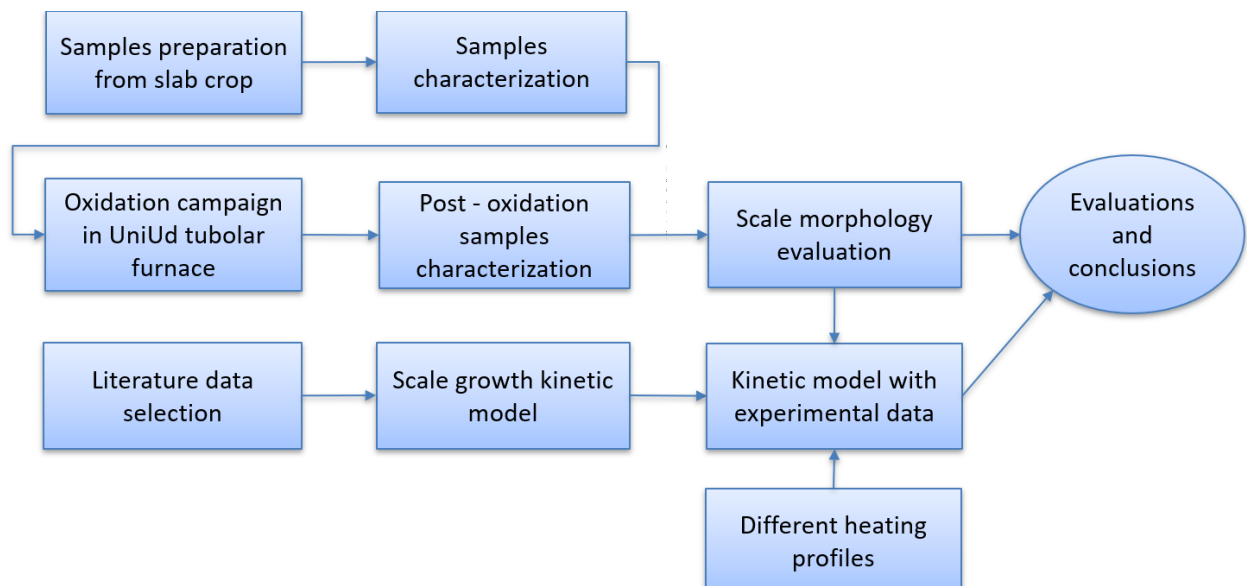
Figure 99 - Workflow diagram

HYINHEAT

F.2.3 Test equipment and procedure

N_2 or the oxidating mixture. The desired oxidating mixture is obtained adjusting the N_2 and O_2 flows from the gas bottles by a ball flowmeter, and the water addition is regulated by a HPLC pump.

Two steel samples at a time were placed into a refractory sample holder (alumina), the first one equipped with a thermocouple.
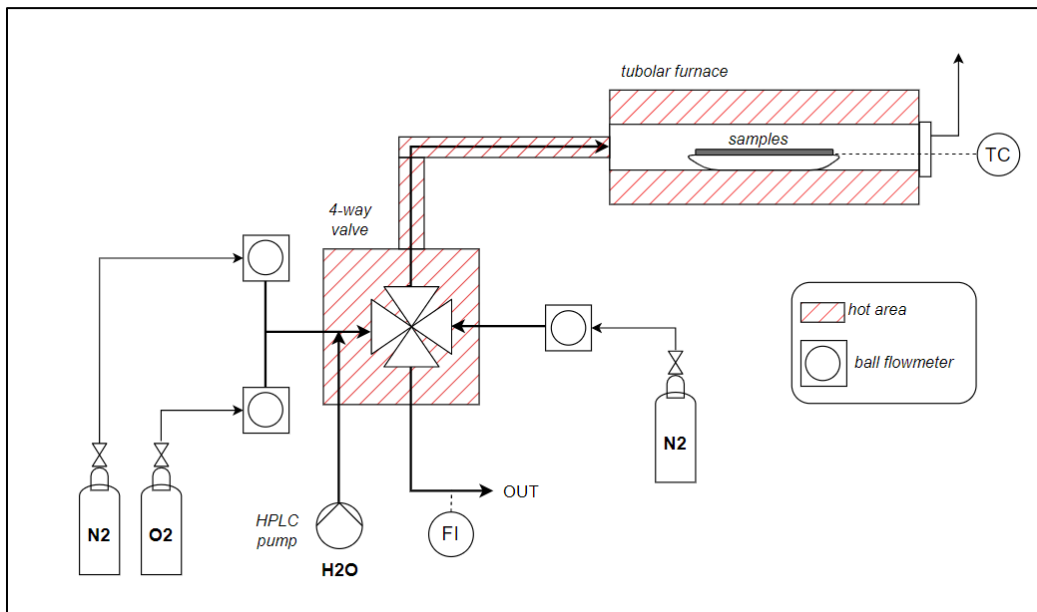
Figure 100 - Experimental equipment scheme

The main operations during the test are:

1. Samples placed into the refractory crucibles are introduced into the cool tubular furnace
2. Heating-up up to 500°C under mild N_2 flow
3. Heating-up up to test temperature with N_2 flow
4. When the test temperature is reached, increasing of the N_2 flow
5. In the meantime the oxidating gas mixture is prepared
6. The correct oxidating gas mixture is feed to the tubular furnace by switching the 4-w valve
7. The gas flow is then suddenly switch to N_2 flow in order to stop the oxidation phase
8. The samples are cooled under N_2 flow until 400°C
9. The samples are extracted from the furnace when cooled at Room Temperature

HYINHEAT

F.2.4 Test and model results

The characterization activity has also provided a series of semi-quantitative indications concerning the influence of oxidation on the quality of the surface and on the aptitude for descaling.

Compared to medium carbon, low carbon steel results in a thicker (+20%) and more dense and homogeneous scale. According to morphological observations, this scale, although thicker, can be more easily removed during the descaling phase, reducing the onset of imprinted scale.

The experimental data was used in a first attempt scaled growth kinetic model which is being calibrated at the plant. The kinetic model of scale growth is based on the widely accepted Wagner theory that describes scale growth as a function of a diffusivity parameter and a concentration gradient of oxidants. In the internally developed, six-parameter model, the terms are further described as a function of temperature, time, oxygen concentration and water vapour.

The model was tested both with a literature data set and with an experimental one, resulting satisfactory in terms of regression quality.
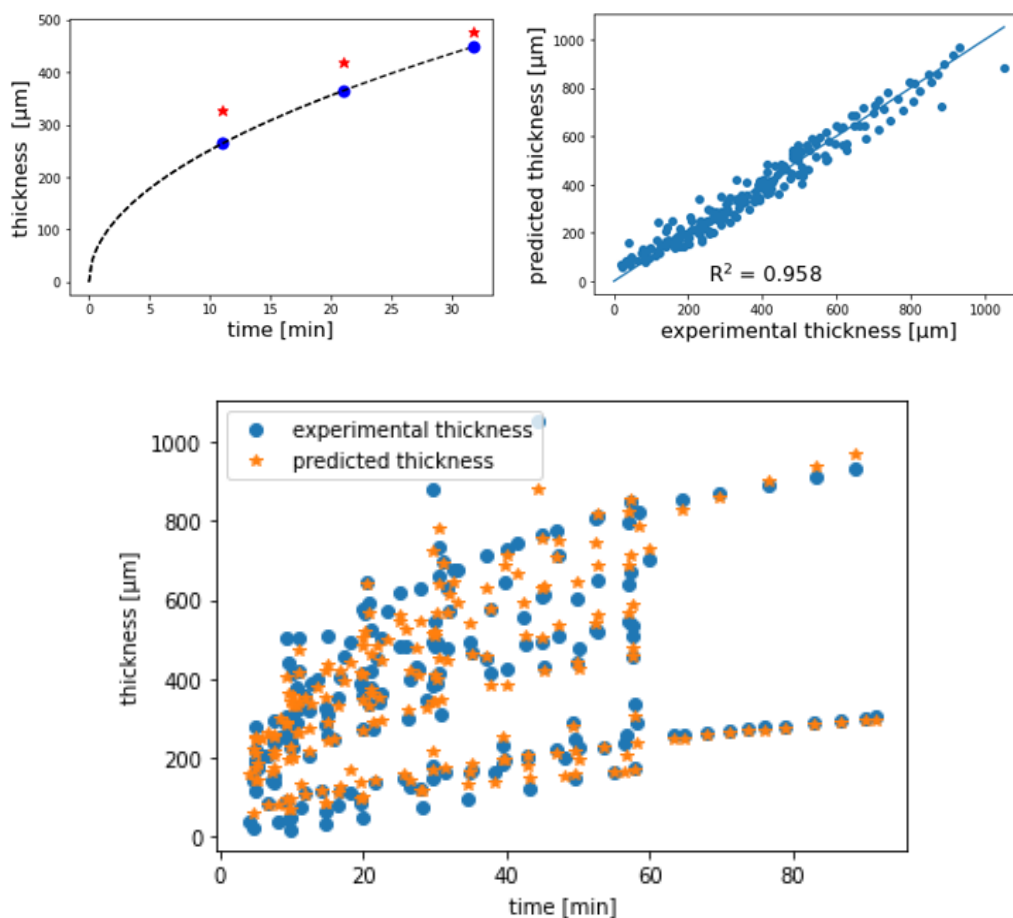
Figure 101 - Model test

Possibilities for future improvement and optimization of the kinetic model are:

- the possibility to adapt the model parameters to specific steel grades through further experimental campaigns and data regression.
- make the model more complex and increase the dependencies (carbon and other main elements of steel; carbon dioxide content in the atmosphere)

The next step will be to further validate the model when applied to a variety of industrial reheating furnaces, of DAN Centro Combustion.

HYINHEAT

F.3 Scale growth simulation comparison between natural gas and hydrogen

F.3.1 Scope of the simulation

The scope of the simulation is to calculate the growth of the scale on a billet surface in two different scenarios: a traditional combustion furnace working with natural gas and the case of burning hydrogen, considering the same heating profile but different fumes composition.

The kinetic model previously described is used.

DAN is showing this case study an example with the purpose of future comparison with other models and data obtained in the HyInHeat project.

F.3.2 Input data

The combustion heating conditions were provided by DAN Centro Combustion Proprietary software: EFESTO.

The following condition has been simulated in two scenarios: actual Natural Gas combustion and Pure Hydrogen combustion.

CASE STUDY

Furnace type	Walking Beam Furnace
Charge type	Billets
Billet	180 x 180 x 12,500 mm
Steel grade	Low carbon
Productivity	170 tph
Stock in temp	20°C
Stock out temp	1,250°C
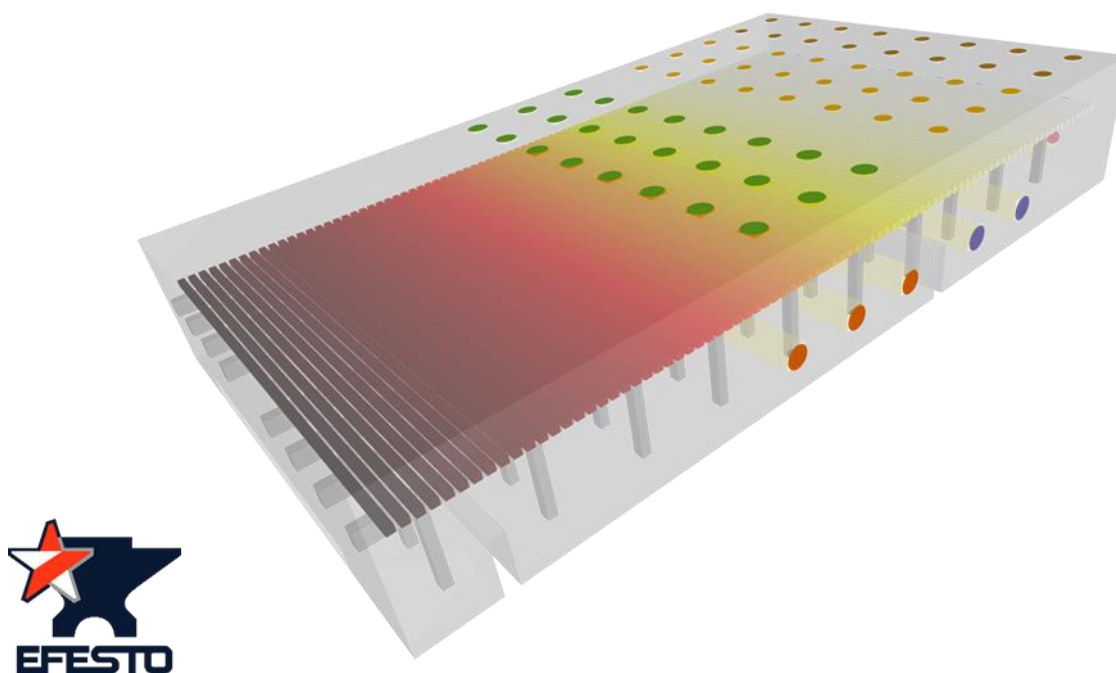
Figure 102 - EFESTO Furnace simulation

Impact of H$_2$ heating on product quality, yield, and refractory

The Concentration profiles are considered flats and steady during time, according to:

WASTE GAS COMPOSITION	CO$_2$%	H$_2$O%	N$_2$%	O$_2$%
NATURAL GAS	9⇓⇓	18 ⇑	72	0.9
HYDROGEN	0	34.7	64.4	0.9

Figure 103 - Natural Gas Combustion atmosphere	*Figure 104 - Hydrogen Combustion atmosphere*
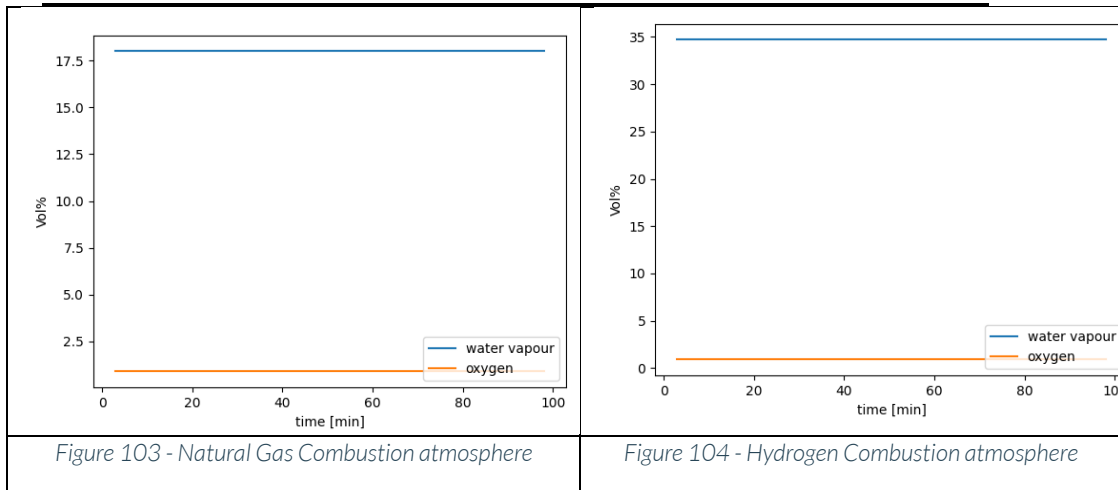
The Heating profile is obtained from EFESTO software simulation.

F.3.3   Simulation results
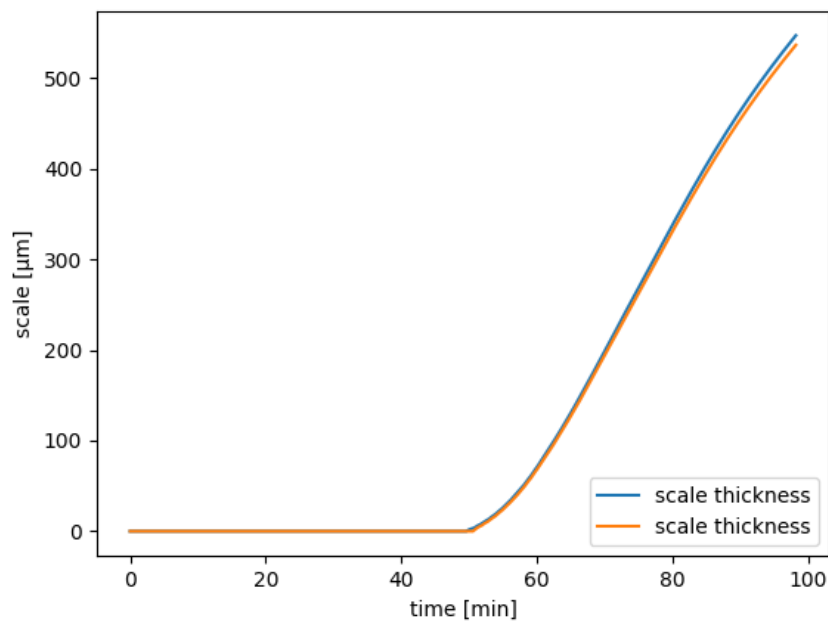
The calculated scale-growth profile is represented in the below graph, reacjing a final thickness of about 536 µm for the natural gas, 546 µm for the hydrogen case.

The scale thickness is very similar for both cases, despite the water vapour concentration is double in the case of hydrogen; the reason is that both values are anyway high values and the effect of water vapor in going towards saturation in that range.

HYINHEAT

F.4   Scale Free Furnace

DAN Centro Combustion, the division of DAN which deals in combustion technologies for industrial furnaces, is investing in innovative technologies and processes, such as so-called Scale-Free furnaces that not only help improve yield on finish products, but also help reduce emissions and improve the thermal efficiency of industrial furnaces.

This Furnace concept is here shortly described for being a innovative solution to the scale formation phenomena.

Figure 105 - Scale free furnace sidewall Burners

F.4.1   Furnace basic concept

The Scale Free Furnace is a type of walking beam furnace for billets, blooms, beam blanks, and light slabs with the goal to halve the scale formation and reduce both fuel and CO_2 emissions. In order to achieve these goals, the following measures are applied:

1. Physical separation of combustion zones (preheating, heating and soaking) consisting of walls and septa;
2. Dedicated Combustion ratio control, in heating and soaking zones, where the scale formation appears the most;
3. DAN Centro Combustion burners with flameless technology
4. Furnace material (refractories, riders etc.) chosen for working in excess of gas without maintenance problems;
5. Furnace designed to avoid entrance of false air in normal process conditions and exit of unburned gas during the transitory conditions, the furnace.
6. Additional instrumentation to control better the combustion and avoid exit of unburned gas from the chimney

HYINHEAT

F.4.2 Furnace results

While the target for Scale-Free furnaces is to reduce the scale loss of heated steel, they also help reduce fuel consumption and therefore CO_2. The following results show the amount of savings that can be achieved by Scale-Free furnaces.

SCALE FORMATION

50%

FUEL CONSUMPTION

5%

CO2

5%
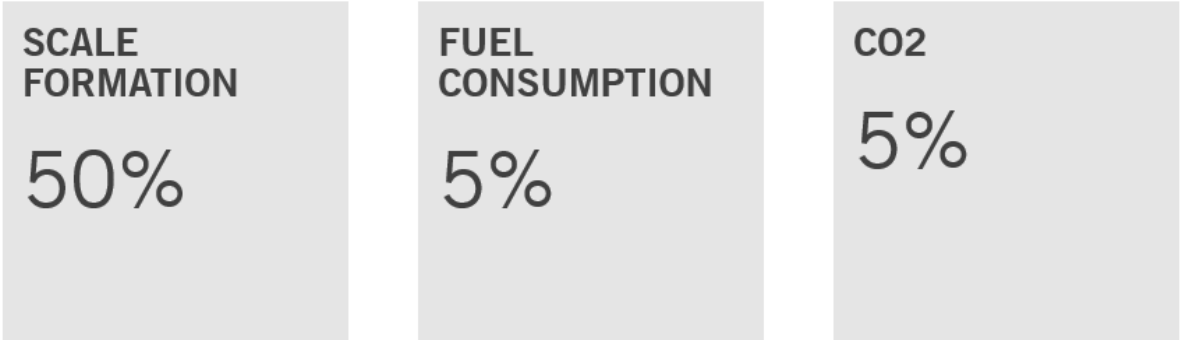
Figure 106 - Scale Free Furnace Savings

Overall, a Scale-Free furnace is essential for maximizing efficiency, reliability, and environmental sustainability in the steel industry. By reducing scale buildup and ensuring optimal furnace performance, steel manufacturers can achieve higher productivity, lower operating costs, and reduced environmental impact, ultimately driving long-term success and competitiveness.

DAN Centro Combustion has installed the first Scale-Free reheating furnace in the state-of-the-art ABS QWR 4.0 rolling mill plant, reaching performances exceeding the guaranteed ones.

Thanks to DAN Hydrogen Ready burners, the Scale Free Furnace is suitable and ready for Hydrogen combustion.

F.5 Conclusion

Since 2020 DAN has studied Hydrogen combustion in several aspect and product quality is a priority. The first crucial step on this topic is the research project presented in this report. Thanks to the precise work of DAN Research Center a solid model for product quality prediction in Hydrogen combustion atmosphere is now experimentally validated. Further validation with scale measurements on industrial application will be the next milestone.

At the same time DAN Centro Combustion developed a radical and game changing solution to the scale phenomena: the Scale Free furnace. This furnace type has already been supplied and built with an Hydrogen Ready combustion system. Hydrogen combustion results on the industrial application are yet to come.

HYINHEAT

G. Substitution of Refractory Ceramics Fibres for Alkaline Earth Silicate Fibres and Their Thermal Performance

G.1 Introduction

It is necessary to take into account that the technology of Man Made Vitious Fibres (MMVF) has progressed since most existing re-heat furnaces were specified and constructed. Traditional Refractory Ceramic Fibres (RCF) have increasingly been replaced with Low Bio Persistent, Alkaline Earth Silicate (AES) fibres such as the Superwool range. Of prime consideration to designers is the heat flow characteristics of these insulating materials as defined by their thermal conductivity.

In 1997 the European Commission added man-made vitreous (silicate) fibres to the list of dangerous (hazardous) substances under the European Union Directive 67/548/EEC. This Directive classifies substances according to their specific hazard and sets out requirements for hazard communications to users through packaging, labelling and material safety data sheets. The classification framework for MMVFs is complicated, but may be summarised for the purposes of this document as:

• Some MMVFs are classified as category 2 carcinogens (substances which should be regarded as if they are carcinogenic to man).

• Most commercial MMVFs are classified, by default, as category 3 carcinogens (substances which cause concern for man owing to possible carcinogenic effects). However, these MMVFs may be exonerated from category 3 carcinogen classification if they meet certain criteria in the Directive.

For high temperature insulation wools, this framework classifies RCFs as category 2 carcinogens and exonerates the AES (Superwool) range of products from any carcinogen classification through Note Q.

In 2008 a new regulation - classification, labelling and packaging of substances and mixtures (regulation 1272/2008/EEC) came into force with the main aim of bringing EU Clasification and Labelling into line with Globally Harmonised System.

Under this new regulation:

Cat 1 = 1a Cat 2 = 1b Cat 3 = 2

Notes Q and R still apply therefore:

RCF (refractory ceramic fibre) = 1b

AES such as Superwool® fibre = Exonerated

G.2 The consequences of carcinogen hazard classification in the European Union

Classification of RCFs in the European Union as category 2(1b) carcinogens triggered a number of downstream regulations both across the European Union and in individual Member States. These require measures to be taken by Member States to restrict the use of and control exposures to RCFs in order to minimise possible adverse impacts to human health and the environment. The classification numbering has changed, but the regulation still remains the same.

The measures include:

• Prohibiting manufacturers and suppliers from placing RCFs on the market for use by the general public (Directive 76/769/EEC).

• Requiring employers using RCFs to seek a substitute which would present a lower risk to the health of workers, or to contain the RCFs and implement measures to reduce occupational exposure to the lowest technically achievable (Directive 2004/37/EC).

HYINHEAT

• Handling and disposing of waste RCFs from manufacture and use as hazardous substances, by a licensed waste contractor and in an appropriately licensed landfill (Directives 91/689/EEC and1999/31/EC).

In January 2010, the EU declared RCF to be an SVHC (Substance of Very High Concern) and added it to Annex XV of the European REACH regulation.

These downstream consequences have applied to the marketing and use of RCFs since their classification as category 2(1b) carcinogens, and have resulted in increased costs of compliance for manufacturers, suppliers and users of RCF.

They do not apply to the AES Fibres such as the Superwool range of products.

Additionally, European Union Member States have the right to implement their own worker protection measures, such as the setting of Occupational Exposure Limits. Many Member States have introduced lower Occupational Exposure Limits for MMVFs since the 1997 classification. Some of the low Occupational Exposure Limits set, or proposed, in Europe for RCFs are very low and difficult to achieve.

For the reasons outlined above, new reheat furnaces or those which are being re-insulated during an upgrade to hydrogen are likely to be substituting AES for RCF Fibres. It is therefore important for Industry to understand the similarities and differences between the grades, especially in regards to heat transfer properties (Thermal Conductivity)

G.3 Thermal Conductivity of AES and RCF Fibre Products

TCUK collected from various production sites samples of Man Made Vitious Fibre products representative of those which are used in the AMS and AMO reheating furnaces, and those which would be recommended to use in future relining or greenfield sites. These were tested for Thermal Conductivity before partial samples were sent to CEIT for testing in Hydrogen combustion atmospheres.

The Thermal Conductivity was measured using equipment conforming to ASTM C201. The coefficient of thermal conductivity is a value corresponding to the intensity of a thermal flow which runs through a sample as a consequence of a thermal gradient normally directed to its surface. It is expressed in Wm−1K−1. The heat flow is determined using a water circulating calorimeter of size 76mm by 76mm, which is guarded on either side by water cooled plates maintained at the same temperature, these are of a size such that the overall area being tested is 450mm by 335mm. The sample thickness is typically 75mm and at the highest test temperature a 1200°C thermal difference can be established between the hot and cold faces. Table 33 and Figure 107 shows the Thermal Conductivities of the various fibre materials relevant to re heat furnaces.

HYINHEAT

Impact of H$_2$ heating on product quality, yield, and refractory

Table 33 Thermal Conductivity of Various Fibres suitable for Re Heat Furnaces

| AES /RCF	AES	AES	AES	AES	AES	AES	RCF	RCF
Product name	Superwool XTRA	Superwool Prime	Superwool HT	Superwool Prime	Superwool Plus	Superwool Plus	Cerachem	Cerachem
Format	Module	Module	Blanket	Blanket	Blanket	Board	Blanket	Module
Classification Temperature	1450	1300	1300	1300	1200	1200	1430	1430
Temperature	Thermal Conductivity Wm-1K-1							
200	0.08	0.06	0.05	0.05	0.04	0.08	0.04	0.07
300	0.10	0.07	0.06	0.06	0.05	0.08	0.06	0.08
400	0.12	0.08	0.08	0.08	0.07	0.09	0.08	0.09
500	0.15	0.10	0.10	0.10	0.09	0.10	0.10	0.11
600	0.18	0.12	0.13	0.13	0.12	0.12	0.13	0.14
700	0.22	0.14	0.17	0.16	0.15	0.13	0.16	0.16
800	0.27	0.17	0.22	0.19	0.18	0.16	0.20	0.20
900	0.32	0.20	0.28	0.23	0.21	0.18	0.24	0.23
1000	0.38	0.24	0.34	0.27	0.25	0.20	0.28	0.27
1100	0.45	0.27	0.41	0.32	0.30	0.23	0.33	0.32
1200	0.52	0.31	0.49	0.37		0.26	0.39	0.37
1300	0.60							
Measured Density Kgm-1	211	198	115	125	127	380	128	175
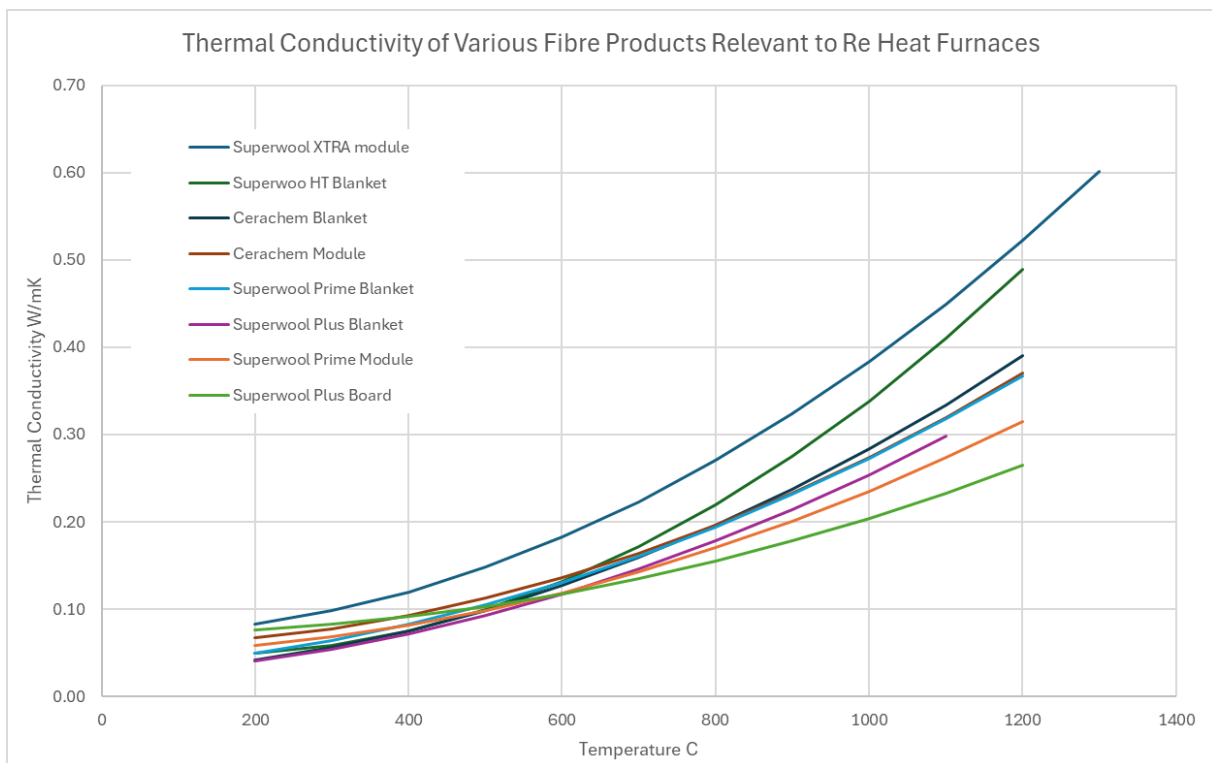
Figure 107 Thermal Conductivity of Various Fibre Products Relevant to Re Heat Furnaces

G.4 Conclusion

It can be concluded that comparative to Cherachem pyro modules, a slightly thicker lining of Superwool XTRA modules would be required, but in the case of Superwool Prime modules (which is the new version of the now obsolete Superwool HT grade), then a direct substitution is possible with additional energy savings. In all cases it is recommended to do heat flow calculations at the specification stage.

HYINHEAT

H. Bibliography

AlSCAN. (2024, May 22). *https://new.abb.com/products/measurement-products/analytical/metallurgical-analyzers/alscan*.

Chen, R. Y., & Yuen, W. Y. (2013). Effects of the presence of water vapour on the oxidation behaviour of low carbon–low silicon steel in 1% O2–N2 at 1073 K. *Oxidation of metals 79.5*, 655-678.

Cochran, C. N.; Belitskus, D. L.; Kinosz, D. L. (1977). Oxidation of Aluminum-Magnesium Melts in Air, Oxygen, Flue Gas, and Carbon Dioxide. *Metallurgical Transactions B*, 324 - 332.

Fukagawa, T., Okada, H., & Maehara., Y. (1994). Mechanism of red scale defect formation in Si-added hot-rolled steel sheets. *ISIJ international*, 906-911.

Gadadhar SAHOO, M. D. (2016). Hot Ductility and Hot-Shortness of Steel and Measurement Techniques: A Review. *Journal of Metals, Materials and Minerals*, Vol. 26, N°2, pp. 1-11.

Haapakangas, J. (2024). Oxide Scale Formation on Low-Carbon Steels in Future Reheating Conditions. *Metals*, 189.

Luzzo, I. (2021). Feasibility study for the utilization of natural gas and hydrogen blends on industrial furnaces. *Matériaux & Techniques*, 306.

N. Birks, G. H. (2006). *Introduction to the High Temperature Oxidation of Metals.* Cambridge University Press.

Palladino, C. (2023, May 28). *Lex in depth: the staggering cost of a green hydrogen economy.* (Financial Times) Retrieved July 20, 2023, from https://www.ft.com/content/6e22930b-a007-4729-951f-78d6685a7514

Richard Osei, S. L. (2022). Effect of Cu Additions on Scale Structure and Descaling Efficiency of Low C Steel Reheated in a Combustion Gas Atmosphere. *Oxidation of Metals*, 98:363-383.

Stones, J. (2023, April). *EU Hydrogen Bank could bring renewable hydrogen costs below €1/kg.* (ICIS) Retrieved July 20, 2023, from https://www.icis.com/explore/resources/news/2023/04/05/10873154/eu-hydrogen-bank-could-bring-renewable-hydrogen-costs-below-1-kg/

Syvertsen, M.; Johannsson, A.; Lodin, J.; Bergin, A.; Ommedal, M.; Langsrud, Y.; Peterson, R. D. (2023). Oxidation Study of Al–Mg Alloys in Furnace Atmospheres Using Hydrogen and Methan as Fuel. *Light Metals 2023* (pp. 936 - 941). San Diego: TMS.

Thank, E. P. (2023, April 05). *EU rules for renewable hydrogen: Delegated regulations on a methodology for renewable fuels of non-biological origin.* Retrieved July 15, 2023, from https://www.europarl.europa.eu/thinktank/en/document/EPRS_BRI(2023)747085

Tiryakioğlu, M. (2020). The Effect of Hydrogen on Pore Formation in Aluminium Alloy Castings: Myth Versus Reality. *Metals*, 368-384.

Tiryakioğlu, M. (2021). On Estimating the Hydrogen Solubility in Solid Aluminium Alloys and the Hydrogen Solubility Difference between the Liquidus and Solidus Temperatures. *Intl. Journal of Cast Metals Research*, 83-87.

HYINHEAT

Get in touch

Website

http://hyinheat.eu/

Email address

info@hyinheat.eu